MICRO AND NANOTECHNOLOGY FOR CANCER TREATMENT

By

ADEETI ULLAL

B.S. Bioengineering, University of California, Berkeley, 2008

SUBMITTED TO THE HARVARD-MIT DIVISION OF HEALTH SCIENCES AND TECHNOLOGY
IN PARTIAL FULLFILLMENT OF THE REQUIREMENTS FOR THE DEGREE OF

DOCTOR OF PHILOSOPHY IN BIOMEDICAL ENGINEERING

AT THE

MASSACHUSETTS INSTITUTE OF TECHNOLOGY

JUNE 2013

Signature of Author:

Harvard-MIT Division of Health Sciences and Technology
May 20, 2013

Certified by:

Ralph Weissleder, M.D., Ph.D.
Directer, Center for Systems Biology, Massachusetts General Hospital
Professor, Department of Systems Biology, Harvard Medical School
Thesis Supervisor

Accepted by:

Emery N. Brown, M.D., Ph.D.
Co-Director and Professor of Health Sciences and Technology, MIT
Associate Director, Institute of Medical Engineering, MIT

MICRO AND NANOTECHNOLOGY FOR CANCER TREATMENT

By

ADEETI ULLAL

Submitted to the Harvard-MIT Division of Health Sciences and Technology on May 20, 2012 in Partial Fulfillment of the Requirements for the Degree of Doctor of Philosophy in Biomedical Engineering

Abstract

Cancer is responsible for over 7.6 million deaths worldwide; the majority of patients fail to respond to drugs or become resistant over time. In order to gain a better understanding of drug efficacy in patients, we developed three diagnostic technologies to address limitations in sample acquisition and improve the scale and sensitivity of current cancer diagnostic tools.

In the first section, we describe a hybrid magnetic and size sorting microfluidic device that isolates rare circulating tumor cells from peripheral blood. The self-assembled magnetic sorter creates strong magnetic fields and effectively removes leukocytes tagged with magnetic nanoparticles. The size sorting region retains the remaining cells in single cell capture sites, while allowing small red blood cells to pass through 5μm gaps. The device achieves over 10^3 enrichment, up to 96% recovery of cancer cells and allows for on-chip molecular profiling.

In the second section we use a magnetic nanoparticle decorated with small molecule drugs to assay target expression and drug binding in mock clinical samples of cancer cells spiked into whole blood. Specifically, we modify a PARP inhibitor (Olabarib) and conjugate it to a dextran coated iron oxide nanoparticle. We measure the presence of the drug nanosensor based on the change in T_2 relaxation time using a miniaturized, handheld NMR sensor for point-of-care diagnosis.

In the final section, we detail a photocleavable DNA barcoding method for understanding treatment response via multiplexed profiling of cancer cells. We validate our method with a 94 marker panel on different cell lines with varying treatments, showing high correlations to gold standard methods such as immunofluorescence and flow cytometry. Furthermore, we demonstrate single cell sensitivity, and identify a number of expected biomarkers in response to cell treatments. Finally, we demonstrate the potential of our method to help in clinical monitoring of patients by examining intra- and inter-patient heterogeneity, and by correlating pre and post-treatment tumor profiles to patient response. Together, we show how these technologies can help overcome clinical limitations and expedite advancements in cancer treatment.

Thesis Supervisor: Ralph Weissleder, M.D., Ph.D.
Title: Director, Center for Systems Biology, Massachusetts General Hospital; Professor, Systems Biology, Harvard Medical School

| Acknowledgements |

It has been a blessing to be in a graduate community full of role models: visionary professors, supportive friends, and encouraging colleagues.

First and foremost, I must acknowledge Ralph. When I joined the lab just three years ago, I was an eager, but naive graduate student. Thought I felt uncertain about my research skills many times, Ralph always displayed the utmost confidence in my abilities. He held me to high standards, encouraged creativity, and pushed me to achieve my best. He has taught by example, and I remain inspired by Ralph's work ethic (both in the lab and hospital), scientific curiosity, and genuine kindness to patients. Thank you.

To my thesis committee members, Bob Langer and Alice Shaw, thank you for your keen insights, time and guidance. Beyond research, I am thankful that Professor Langer for taking the time to advise me about life after grad school. Thank you to Professor Shaw, an unbelievable oncologist, who allowed me to shadow her in clinic and has even answered my own questions when my aunt was diagnosed with lung cancer.

Thanks to the many members CSB/the Weissleder lab, who have helped me tremendously. In particular, thank you to Katy and Hyun, the best benchmates, and my confidantes through all grad school strife. You both have unbelievable scientific ability only matched by your humility. To my UROP, Tuang, sometimes I am not sure who is the mentor and who is the mentee. Your curiosity, optimism, and lease on life brought joy to the lab. To my fellow grad students, Vanessa, Anna, and Huilin: in a sea full of high-achieving postdocs, thanks for commiserating about common grad student fails. Special thanks Vanessa, who played "Lucy" to my "Ethel" during numerous, delirious late night experiments. To my other collaborators: the chemists, Eunha, Sarit, Ghyslain, you guys made life in lab fun and productive, and the engineers, Dave and Jaehoon, for thoughtful discussions about life and research. To the many other senior postdocs and professors (Jered, Greg, Thomas, Cesar, Claudio, Ralph M, and Hakho) who helped a young grad student become proficient. Finally, special thanks to the Pittet lab who shared my passions outside of lab: tennis, singing, running and lung cancer fundraising. Andita, your daily dose of sass mixed with support and Camilla, your harmonies/ dance moves/thoughtful insights, brightened up many a bleak week.

There are numerous friends who have become my "Boston family". Anitha, or "Niths" -- you have been my soul-sister through this process. Your understood everything and your empathy kept me going. Sofia ("Sof"), thank goodness for that teary-eyed run-in, our first year. Despite everything you take on, you have been there, without question, in my hardest moments. To HST-brown-original: Kaka and Raju, if everyone had friends like you, the world would be a better place. My 'party-circuit' girls: Alison, Jean, and Elena, you guys remind me that it is possible for high achievers with workaholic tendencies to have social lives! Thank you to the friends I could always count on: Calvin, Sheena, Anand, and Tiffany. To my many other friends from childhood, HST/Harvard/MIT, old roommates, etc., rest assured I will thank each of you personally.

Last, but not least, I owe everything to my family: Amma, Annu, Thatha, Patti, and Tarini. My success is based on the foundation you laid for me.

I dedicate this thesis in honor of my aunt, Subashree Vedantham, or Susie Chithi who passed away from lung cancer. More than her fight with the disease, it was her lifelong commitment to make the world a better place, that inspired me in my research and motivates me in life.

I Biographical Summary I

RESEARCH

- Projects covered diagnostics, devices and research tools.
- Expertise in cancer, pharmacodynamics, clinical translation, assay development, molecular imaging, micro and nanotechnologies, neuroimaging, synthetic biology and protein informatics.

EDUCATION

MASSACHUSETTS INSTITUTE OF TECHNOLOGY-HARVARD UNIVERSITY
Harvard-MIT Division of Health Sciences and Technology
PhD, Bioengineering, 2008-expected May 2013 | GPA 5.0/5.0
Concentration: Electrical Engineering
Thesis Advisor: Ralph Weissleder, Professor, Harvard Medical School
Thesis Chair: Robert Langer, David Koch Institute Professor, MIT
Thesis Reader: Alice Shaw, Assistant Professor, Massachusetts General Hospital

UNIVERSITY OF CALIFORNIA, BERKELEY
BS, Bioengineering, High Honors 2004-2008 | GPA 3.81/4.0
Certificate of Management and Innovation, College of Engineering

EXPERIENCE

PH.D. CANDIDATE
Center for Systems Biology, Massachusetts General Hospital *2010-present*
Developed micro and nanotechnologies for cancer treatment including 1) magnetic nanoparticle assays for drug binding 2) microfluidic devices for capture and analysis of circulating tumor cells 3) platform technology for multiplexed protein measurement of single cells

CO-DIRECTOR OF SCIENCE AND RESEARCH, JILL'S LEGACY
Bonnie J. Addario Lung Cancer Foundation *2010-present*
Reviewed and awarded $50k-100k grants to researchers from top institutions as part of young adult advisory board to lung cancer non profit.

TEAM MEMBER, MIT 100K BUSINESS PLAN COMPETITION
Oncolyse *9/2011-6/2012*
MIT 100k Biotech Wild card Awardee; Spun out of Harvard Medical School research on cancer immunotherapy targeting CD59, which won Harvard University Research Entrepreneurshp Symposium 2011 Winner

INTERN, CLINICAL MEDICINE
Mount Auburn Hospital, Harvard Medical School *1/2012; 6/2012*
12-week immersion into hospital setting after completing coursework in anatomy, pathology, and pathophysiologies. Performed complete physical exam and patient histories, wrote reports, and rounded with interns and residents

EXPERIENCE

Nanoparticle Drug Delivery (6/09-6/10, Sengupta Lab, Brigham and Women's Hospital)

Metabolic Engineering/Synthetic Biology ('06-'08, Codon Devices, Keasling Lab)

EEG/MEG studies for epilepsy (UCSF, Nagarajan Lab, 6/'07-8/'07)

HONORS

National Science Foundation Graduate Research Fellow, 2010-13

NCI-NIH Centers of Cancer Nanotechnology Excellence Fellowship, 2012-13

MIT Henry C. & Frances Keany Rickard Fellowship, 2010-2011

Hertz Fellowship Finalist, 2009 *(awarded to top 50 doctoral candidates)*

Member, American Association of Cancer Research

UCSF LEADS Scholarship, 2009-2010 *(awarded to 8 students in entire UC system)*

PUBLICATIONS

Ullal, AV*, Peterson, V*, Agasti, S, Tuang, S, Juric, D, Castro, C, Weissleder, R. "Photocleavable Immuno-DNA barcoding Platform Reveals Treatment Sensitivity in Cancer Patients." *in preparation.*

Peterson, V.*, Castro, C.*, Chung, J, Miller, N, **Ullal, A.**, Castano, M., Penson, R., Lee, H., Birrer, M., Weissleder, R. "Ascites Tumor Cell (ATC) Profiling Reveals Reliable Targets for Point of Care Analyses." *submitted.*

Chung, J*, Issadore, D*, **Ullal, AV***, Weissleder, R, Lee, H. "Rare Cell Isolation and Profiling on a Hybrid Magnetic / Size-Sorting (HMSS) Chip." *submitted.*

Ullal, AV, Reiner, T, Yang, KS, Gorbatov, R, Min, C, Issadore, D, Lee, H, and Weissleder, R. "Nanoparticle mediated measurement of target-drug binding in cancer cells." *ACS Nano*, 2011, published online 10.1021/nn203450p. **[Featured in ACS Nano Podcast]**

Reiner, T*, Lacy, J*, Keliher EJ*, Yang, KS, **Ullal, AV,** Kohler, R, Vinegoni, C, and Weissleder, R. "Imaging Therapeutic PARP Inhibition in Vivo through Bioorthogonally Developed Companion Imaging agents." *Neoplasia*, 2012 14(3): 169-177. **[Cover Article].**

Dueber, J., Wu, G., Malmirchegini R., Moon, T., Petzold, C., **Ullal, AV,** Prather, K. and Keasling, J. "Synthetic Protein Scaffolds Provide Modular Control over Metabolic Flux." *Nat Biotechnology*, 2009, 27(8): 753-759.

POSTERS

Ullal, AV*, Peterson, V*, Agasti, S, Tuang, S, Juric, D, Castro, C, Weissleder, R. "Photocleavable Immuno-DNA barcoding Platform Reveals Treatment Sensitivity in Cancer Patients." *HST Forum, Harvard Medical School (4/12/13)*

Ullal, AV, Reiner, T, Yang, KS, Gorbatov, R, Min, C, Issadore, D, Lee, H, and Weissleder, R. "Point-of-care measurement of target-drug binding in cancer cells." *AACR 2012,* (4/02/12), Chicago, Illinois.

Ullal, AV and Weissleder R. "DMR to Assess Treatment Response in Human Cancer." *Harvard-Weizmann Systems Biology Collaborative Symposium,* (3/14/11), Rehovot, Israel.

Ullal, AV, Dueber, J. & Keasling,J. "Metabolic Engineering in a Prokaryotic System: Using Domain- Ligand Binding to Increase Production" *UC Berkeley Undergraduate Poster Session, 4/2007*

Ullal, AV and Mach, A. "A Critical Study of Horizontal Gene Transfer in Yeast, Bacteria and Ciliates: The Rumen Environment." *Bioengineering 240 Class Proceedings, Spring 2007*

Ullal, AV, Kirsch, H. and Nagarajan, S. "Facial Emotional Processing in Epilepsy Patients." *UC San Francisco Summer Research Symposium Summer 2007 Poster Session.*

TALKS

Ullal, AV. "Magnetic Nanoparticle Assays for Treatment Response in Cancer," Centers of Cancer Nanotechnology Excellence (CCNE), Massachusetts Institute of Technology, Cambridge, MA, January 9, 2012.

OTHER

Mentor, Big Sisters Boston, 2011-present; Co-Director, MIT Women's Initiative, 2009-2011; Choreographer and Dancer, Lasya Dance Company, 1992-present; Boston Run to Remember Half Marathon, May 2012

| Table of Contents |

I Table of Figures I

I Chapter 1 I Introduction

1.1 Motivation

Cancer is the leading cause of death worldwide, accounting for 7.6 million deaths in 2008 alone. Some of the deadliest cancers in the US, such as pancreatic and lung cancer have five year survival rates as low as six percent.[1] These rates have not significantly improved in the last 30 years.[1] For these cancers, the majority of patients are diagnosed in advanced stages with highly invasive or metastatic disease, where surgical intervention is not an option.[2] Instead, patients are administered systemic therapies on a "trial and error" basis. The large degree of patient-to-patient variation makes it difficult to predict how a patient will respond to treatment, and tumors can develop resistance to drugs in less than 6 months.[3-7] Consequently, clinical trials for cancer therapeutics are increasingly accompanied by genetic diagnostics to rationally elucidate drug-sensitive and resistant cohorts amongst a heterogeneous group of patients. This companion data is collected at two extremes: a) exome analysis revealing driver oncogenes and specific mutations[45] and b) a limited number of hand-picked protein biomarkers. However, the majority of this data never achieves clinical utility. Mounting evidence shows that this is because single time-point, bulk genetic measurements vastly underestimate the epigenetic and genetic complexity of the tumor.[8,9,10,11] Even genetically similar cells display functional differences; for example, cells with identical genotypes still have different susceptibilities to the same drug.[12] Changes to drug combinations, doses and dosing schedules are required combat drug resistant clones.[13,14,15] Better tools are required to supplement clinical trials with additional pharmacodynamics data. This thesis aimed to create new platforms and assays to isolate cells and measure drug binding, drug dosing and cellular response.

1.2 Cancer Treatment: Attacking the Hallmarks of Cancer

Cancer is a highly complex disease; each tumor arises through multiple mutagenic steps in different pathways ranging from epigenetic histone changes to DNA repair and growth/survival signaling.[13,16,17,18] Within a single tumor there is great genetic and proteomic heterogeneity and a clonal population within the tumor can continue to proliferate even when the majority of the cells die.[19] There is a also great deal of patient-to-patient variation due to both genetic and environmental factors. As such, there is an increasing need to develop individualized treatment regimens.[20] Currently there are two major types of treatments: cytotoxic agents which inhibit cell proliferation, and molecular targeted agents, which act on specific signaling pathways and proteins.

1.2.1 Cytotoxic Drug Treatments

In early stages of cancer, the tumor is highly localized, and surgical resection is often curative. However, patients with advanced disease must undergo systemic therapies such as chemotherapy and radiation. These traditional therapeutics exploit the increased replicative potential and heightened sensitivity of cancer cells to DNA damage or genotypic stress. Chemotherapeutic or cytotoxic drugs, work by attacking dividing cells through several mechanisms. Alkylating agents are one class (e.g. cyclophosphamide, dacarbazine, temozolomide) that work by directly damaging DNA to prevent cancer cells from dividing. Platinum agents such as cisplatin, carboplatin and oxaliplatin which covalently bind to DNA to induce damage are also sometimes considered alkylating agents.[21,22] Antimetabolites (e.g. are 5-fluorouracil, methotrexate, gemcitabine and premetrexed) make up a second group of cytotoxic drugs, and interfere with DNA and RNA by intercalating with nucleotides to disrupt the S phase of the cell cycle. Anthracyclines, or anti-tumor antibiotics such as doxorubicin and mitomycin that interfere with DNA replication enzymes. Topoisomerase inhibitors that act on either topoisomerase I (e.g. topotecan, irinotecan) or topoisomerase II (e.g. etoposide) prevent the separation of DNA strands for replication during the S

phase. The final major class of cytotoxic drugs are mitotic inhibitors that work during the M phase to prevent mitosis. One common group of drugs are taxanes, such as paclitaxel (Taxol) and docetaxel (Taxotere), which inhibit microtubules, in turn preventing spindle formation and cell division.[23] More cytotoxic agents that operate through different mechanisms are still in development such as proteasome inhibitors.[22]

1.2.2. Molecular Targeted Therapy and Personalized Medicine

In an effort to rationally target pathways specific to each cancer, pharmaceutical companies have developed an increasing number of drugs to inhibit pathways upregulated in cancer. Some of the most effective drugs inhibit "oncogenes" that drive tumor growth.[24] By identifying sensitizing genetic mutations, patients can be divided into a select group of drug responders. Success stories such as Gleevec/imatinib (against the BCR-ABL fusion protein in leukemia), Tarceva/erlotinib and Iressa/gefitinib (against EGFR in lung cancer), Herceptin/trastuzumab (against HER2 in breast and ovarian cancers) and Crizotinib (against in lung cancer).[25-29] Another approach is based on "nononcogene addiction," where drugs target genes that may not be oncogenic, but are still necessary to maintain cancer cells. These include proteins involved in a cell's stress response, such as Heat Shock Protein (HSP) and PARP inhibitors.[13,30,31] Despite these advancements, patients inevitably develop resistance to targeted therapies within 2 years.[5,32,33] Increasing evidence has shown that treating heterogeneous cancer cell populations requires innovative treatment strategies such as immunotherapies, unique combination therapies, or interspersed dosing regimens to successfully make caner a manageable disease[15,34] Better tools are required to acquire pharmacodynamic information from cancer cells and the surrounding stroma on a single cell level. An improved understanding of cancer heterogeneity can intelligently guide therapeutic regimens.

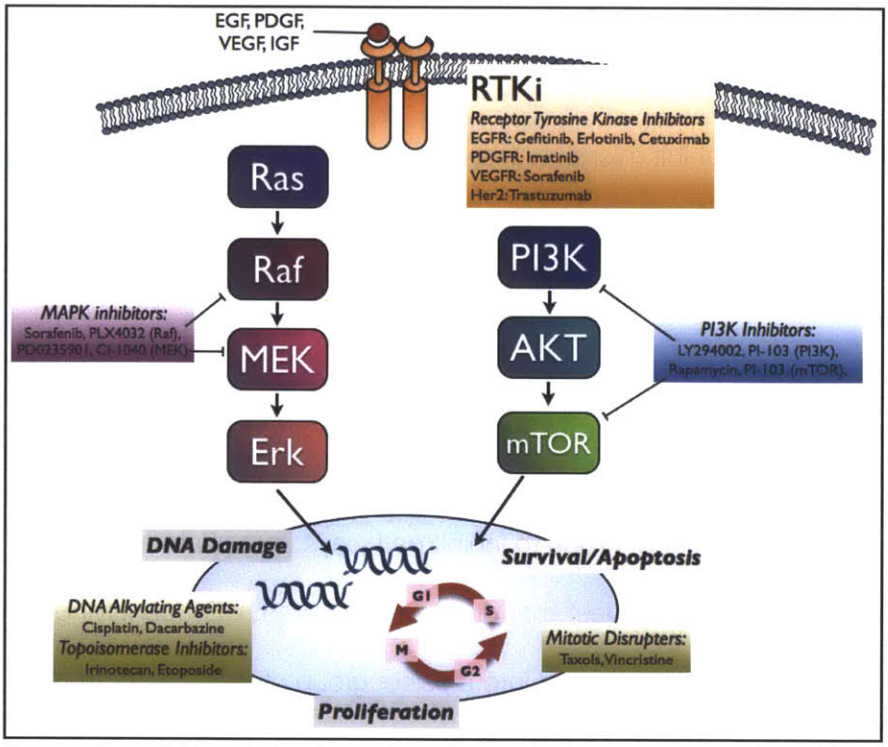

Figure 1.1 Multi-Pathway inhibition as a strategy for cancer treatment using molecular targeted drugs and chemotherapy.

1.3 Pharmacodynamic Measurements in the Clinic: Challenges and Limitations

1.3.1 Sample Acquisition and Processing

Though cancer has been studied extensively in vitro and in vivo, translation to patient samples has been difficult. Serial, repeat biopsies or fine needle aspirate (FNA) to collect cancer samples raise ethical and medical safety questions, and impose greater costs to hospitals and patients. Thus, approval for repeated biopsies is limited to few patients in early clinical trials. Following sample collection, clinical technicians and biomedical researchers face challenges to process, store and isolate cancer cells. Common preservatives such as formaldahyde and paraffin can reduce sample quality making them incompatible with downstream assays.[35] Tissues from biopsies requires additional processing through enzymatic breakdown of extracellular matrix (collagenase) as well as well-defined markers to sort and isolate cells of interest.[36] Fine needle aspirate samples require less processing than biopsies, but also result in far fewer cells (as few as 1,000 per pass), limiting the

number of measurements that can be performed.[37,38] Finally, the half-life of cells and protein markers can be extremely short; in fact, rare cancer cells in the bloodstream (circulating tumor cells, CTCs) have been shown to have half lives as short as 1 hour.[39-41] Thus, pharmacodynamic assays for clinical trials ideally need to be compatible and effective for samples with limited numbers of cells and differing preservations.

1.3.2 Current Diagnostics in Cancer Treatment and Alternative Proteomic Tools

Current clinical practice in cancer diagnosis employs either genomic measurements for known cancer mutations (e.g. Snapshot genotyping and Oncotype Dx)[42,43] or immunohistochemistry (IHC) with a limited number of markers to diagnose cancer type.[44] Genomic data has yielded a number of advances in cancer therapy to identify activating mutations that can be specifically targeted via treatment. However, the number of new mutations discovered has plateaued, and many known aberrations are 'un-druggable,' or impossible to target via small molecules or antibodies.[45] Recent therapeutics have taken alternative approaches including drugging the host immune system, or targeting compensatory proteomic pathways. While proteomic information is valuable, clinical practice is limited by the amount of sample required for current techniques such as IHC. Pathologists typically perform basic H&E staining to identify cellular structure, alongside 3-10 selected markers depending on available sample. These analyses are limited since IHC requires tedious, manual slide preparation with no guarantee of identifying cancerous cells amongst the stroma.[44] Markers are primarily used to distinguish the cancer's originating site (e.g. TTF-1 for lung cancer),[46] and not indicative of therapeutic sensitivities. Often these markers are not standardized and have limited diagnostic power. Finally, many therapeutically relevant markers are expressed in non-cancerous tissues; as such, concurrent staining procedures are necessary to ensure that cells examined are malignant.

Newer proteomic tools have been designed to perform multiplexed marker detection on small amounts of proteomic materials with high fidelity and sensitivity. These include mass spectrometry,[47] mass cytometry,[48-51] or flow cytometry[52]; however, none of these have been introduced clinically due to high costs, poor sample recovery, or limited multiplexing capabilities.

1.4 Advancing Cancer Treatment with Micro and Nanotechnologies

Advances in microfluidics and nanotechnology have created a wave of new devices and platforms to improve companion diagnostics in cancer treatment. Microfluidic advances have allowed for improved cell-surface interactions through surface modifications such as self-assembling monolayers, accurate flow control for controlled mixing and isolation of cells, and combined on-chip sample processing and analysis via integration of optical or magnetic sensors.[53] Nanotechnology utilizes materials, devices and drugs on the scale of 100nm or less and have been applied in molecular sensing, imaging and treatment (drug delivery).[54-56] These include nanodevices, liposomal, polymeric and magnetic nanoparticles, and modified biologics such as antibody fragments and unique DNA barcodes. Nanoparticles confer advantages such as modularity and multiplexing capabilities through surface modifications, multivalency (akin to receptors on cells) to achieve signal amplification, and unique pharamacokinetic properties[57,58]. Here, we cover specific applications of micro and nanotechnology to clinical applications including i) microfluidic devices for rare cell isolation ii) magnetic nanoparticle sensing for cancer diagnostics iii) DNA barcoding on antibodies for multiplexed protein detection.

1.4.1 Microfluidic Devices for Rare Cell Isolation

The isolation and molecular profiling of rare cells from clinical specimens holds significant potential for the early diagnosis and treatment monitoring of disease,[59-61,82] drug discovery,[62] and stem cell research.[63] Particularly, the detection and profiling of circulating tumor cells (CTCs) in whole blood has emerged as a promising methodology to detect, monitor, and better understand cancer.[60,61,64,65]

CTC detection poses a tremendous technical challenge that requires high throughput screening of large volumes of fluid (~10 mL) and enrichment of heterogeneous targets against a complex, vast biological background.[64] Much work has been done to design microfluidic devices that address these challenges. For example, microfluidic chips have employed micro-magnets to efficiently sort magnetically labeled cells with high flow rates, molecular biomarker specific isolation, and easy integration with down-stream microfluidic components.[66-69] Likewise, microfluidic structures have been reported that capture and hold individual cells for on-chip staining, culture, and molecular analyses.[70-72] With an increasing need for frequent patient monitoring during cancer progression and treatment, tools that enable measurements from peripheral blood draws are far more ethical and feasible than invasive cancer biopsies. Thus, microfluidic devices to identify circulating tumor cells are positioned to to make a large impact on treatment monitoring in cancer patients.

1.4.2 Diagnostic Capabilities using Magnetic Nanoparticles

Ultra-sensitive detection of cancer antigens could improve cancer diagnosis and monitoring. Magnetic nanoparticles has been applied to achieve high sensitivity in ex-vivo clinical assays. One sensing technology that utilizes magnetic nanoparticles is DMR (Diagnostic Magnetic Resonance). DMR can quickly and quantitatively determine a molecular profile from scant cells including fine needle aspirates (FNAs), circulating tumor cells (CTCs) and even tumor exosomes of cancer patients [37,73]. The device consists of a miniaturized NMR probe that can measure the transverse relaxation time ($T_2 = 1/R_2$) of the water molecules in the sample. Magnetic nanoparticles conjugated to an antibody can then be applied to the sample to detect the expression of a particular protein. The presence of magnetic, iron core nanoparticles increases the relaxation rate of the surrounding water molecules, resulting in a decrease in the spin-spin relaxation time (T_2). By tagging cells with magnetic nanoparticles targeted to a marker-of-interest, we can detect a change in the relaxation time between tagged cells and non-tagged cells. This is proportional to the amount of magnetic nanoparticle present, and in turn protein expression. Specifically we use

cross-linked iron oxide (CLIO) nanoparticles that are approximately 30 nm in size and can easily penetrate permeabilized cells.[74] Using these nanoparticles, the DMR system can detect as few as 2 cells in 1-uL volumes in less than 15 minutes.[73] The latest DMR (DMR-4) also has superior temperature control for consistent measurement.

Current technologies for molecular profiling are time consuming, expensive and require large sample sizes. Though clinical MRI scanners and benchtop relaxometers with low field (<1 Tesla) magnets have been used in the past, these devices were unable to make parallel measurements and required large sample volumes. DMR technology has been designed considering clinical limitations such as sample size. The chief advantages of the chip-based DMR system are high sensitivity and the ability to use microliter sample volumes with minimal processing. While parallel processing can be used to achieve multiplexing, an additional sensor channel with greater variable tags (size, color, etc.) would be required to perform large-scale multiplexed measurements on the same amount of sample.

1.4.3 Nanoscale Biologics: Multiplexed Immuno-detection via DNA barcoding

Genomic detection through qPCR and sequencing rapidly progressed in the last decade to achieve femtomolar sensitivity. DNA sequences can be designed to create hybridizable fluorescent probes and three-dimensional structures that serve as unique barcodes.[75,76] By attaching these barcodes to antibodies, researchers have leveraged the inherent multiplexing and detection capabilities of DNA technologies to boost the sensitivity of immunoassays such as ELISA by 10 to 10,000 fold.[77] Most of these methods have utilized immuno-qPCR (iPCR) with antibodies conjugated with small, designed DNA sequences of various lengths. After the cells are stained with the chimeras, DNA can be released following cell lysis and proteolytic cleavage.[78] Over the years, a number of technical advances have enabled both sensitive and specific detection for clinical

application. These include improved blocking conditions, rolling circle amplification, controlled chimera conjugations via specifically introduced binding sites on the Fab fragment, and the introduction of microfluidics for single cell detection.[76,79 80] Clinical applications have ranged from cytokine measurements in serum to protein biomarker detection in cancer sources. However, costs, limited clinical access and processing times have thus far prevented large-scale multiplexed detection beyond tens of makers.

1.5 Thesis Overview

The overall goal of this thesis is to enable biomedical researchers and clinicians with translational technologies that can improve cancer treatment. Current state-of-the-art methodologies and assays are limited by previously outlined clinical constraints such as cost and sample material. To address these challenges, innovations are required on a number of fronts, including sample acquisition and assay development to efficiently capture large amounts of information. The tools developed in this thesis span a range of clinical hurdles and incorporate innovations on a range of scales from microtechnologies to nanometer sized biologics. First, we tackled the challenge of sample acquisition. Current methods for treatment monitoring require serial clinical samples with repeated invasive procedures. Ideally, future measurements would be less invasive and come circulating tumor cells in peripheral blood. We address challenges in CTC enrichment, capture and release challenges, and detail a combined size and magnetic sorting microfluidic device (Chapter 2). Next, we created tools to improve data acquisition during clinical trials. Drug binding and dosing is the primary focus of early (Phase I) clinical trials. We sought to improve companion tools in this early phase of experimental cancer care with a magnetic nanoparticle assay that could quantify the amount of drug present in circulating tumor cells (Chapter 3). Finally, we describe a large-scale, multiplexed protein detection platform that can profile cancer cells. We go on to demonstrate the

clinical potential of this platform to both predict and monitor treatment response in cancer patients (Chapter 4). We conclude with perspectives and future directions for these projects.

I Chapter 2 I Microtechnology to Characterize CTCs

2.1 Introduction

Circulating tumor cells (CTCs) have emerged as an important biomarker in clinical practice as well as in fundamental research.[61,65] CTCs, shed from primary tumors, have been shown to be an early harbinger of tumor expansion and metastasis,[81] and have been used to predict disease progression, response to treatment, relapse and overall survival.[82-84] Recent work has shown that CTCs display distinct proteomic and genetic profiles; for example, CTCs in pancreatic cancer, have increased RNA expression of Wnt, implicating this pathway in metastasis.[85] Proteomic characterization of proliferative markers such as Ki-67, and hormonal markers such as androgen receptor in prostate cancer, also have been shown to be predictive of treatment outcome.[86,87]

Despite such clinical potential of CTCs, their routine detection and characterization still remains a significant technical challenge.[88] The task requires the screening of a large number of cells (e.g. $>10^7$ cells in 10 mL blood) and enrichment of heterogeneous targets against a complex biological background. Two main methods of CTC isolation are typically used: positive and negative selection. In positive selection, CTCs are directly isolated from blood via size-based filtration[89-93] or antibody-based capture.[61,86,94] The negative methods deplete abundant blood cells, often by immunomagnetic separation, for downstream CTC enrichment.[95] Both approaches have been used for high throughput CTC isolation from whole blood (SI Table 1). Each method, however, has its own inherent limitations. Positive enrichment could be biased by its selection criteria (e.g., cell size, cell surface markers). Negative selection, albeit unbiased, often requires increased sample processing (e.g. multiple washing steps for CTC isolation) that could result in cell loss.

We hypothesized that both positive and negative selection could be combined in a single platform so as to enable 1) highly efficient and unbiased CTC purification, and 2) in-situ molecular analyses on collected cells. As proof-of-concept, we herein describe a hybrid magnetic / size-sorting (HMSS) system, that integrates magnetic- and size-based isolation into a compact microfluidic chip. The HMSS first uses a magnetic filter to deplete leukocytes through immunomagnetic capture. Samples then pass through a size-sorter region that traps individual cells at predefined locations. Since abundant leukocytes are removed by the magnetic filter, the size-sorter could have a low size cut-off (~5 μm), which allows for the unbiased capture of even small cancer cells. Furthermore, molecular probes can be introduced to perform on-chip, multiplexed analyses at single-cell resolution. We evaluated the utility of the developed system by capturing and profiling tumor cells in whole blood.

2.2 Results and Discussion

2.2.1 Hybrid magnetic and size-sorting chip

The structure of the HMSS chip (Fig. 2.1) is based on two distinct miniaturized components that have been developed in our laboratory: a self-assembled magnet filter[69] and a cell-size sorter.[72] The magnet filter consists of a layer of magnetic grains (125 μm, NdFeB), which spontaneously self-assemble into an array of anti-aligned magnetic dipoles (Fig. 2.1b).[69] Such configuration creates a magnetic field pattern that is confined tightly above the surface of the array. The field strength (B) falls off exponentially with distance from the magnet surface, producing steep field gradients (∇B). A large trapping force ($\sim B \bullet \nabla B$) can thus be imparted on magnetically-labeled cells near the magnet surface.[69] In tandem with the magnetic filter, a size-based cell sorter is implemented (Fig. 2.1c).[72] The structure has a weir-style physical barrier with an underpass-gap that allows flow-through of small cells (e.g., red blood cells; RBCs) and effluent fluids. Bigger cells (e.g., CTCs), however, are trapped at the capture sites, which enables in-situ analyses of single cells (Fig. 2.1d).[72,96]

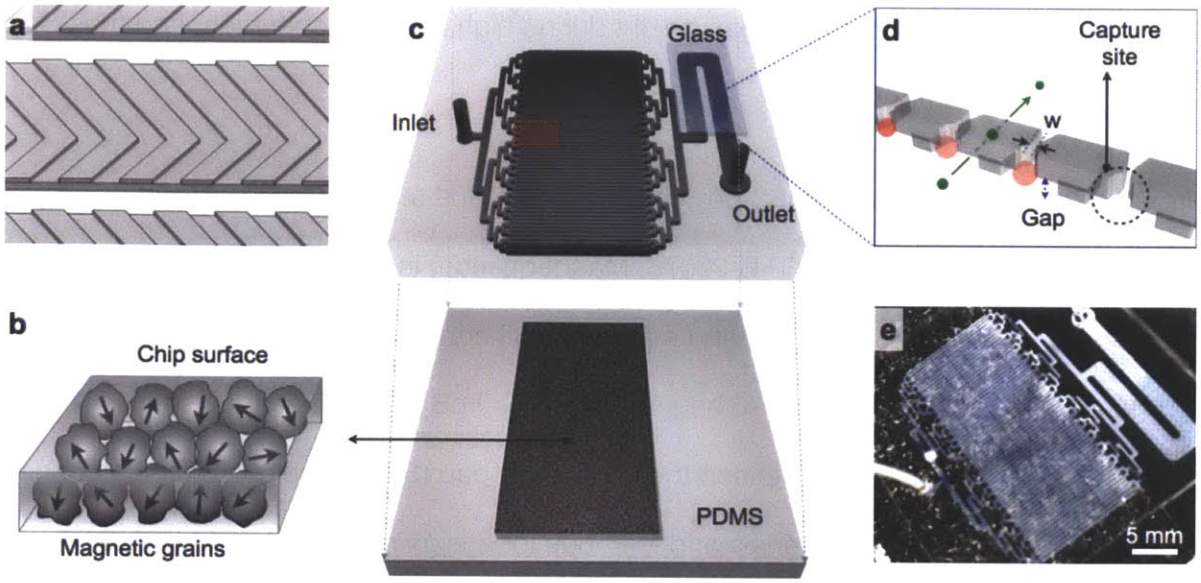

Figure 2.1. Design of microfluidic hybrid magnetic / size-based (HMSS) sorting chip. (a) A herringbone pattern is integrated on main parallel channels to force cells near top surface of channels onto the bottom surface. (b) Magnetic grains are self-assembled on the bottom surface of the channels to generate a large magnetic field and field gradients. (c) Schematics of HMSS sorter: two separate PDMS blocks are permanently bonded. Top PDMS includes parallel channels with herringbone structures, size-based capture sites, embedded glass sled, and connecting ports. The other consists of self-assembled magnetic layer. (d) Schematics of size-based capture structure: cells (red) larger than a underpass gap are captured at capture sites while smaller cells (green) pass through. (e) Fabricated HMSS-sorter.

Compared to our previous magnetic filter and size-based sorter, the HMSS chip incorporates new design features that significantly improve the throughput of the device. First, parallel chaotic-mixing channels are implemented in the magnetic separation region. Unlike a simple laminar flow, the chaotic advection brings cells more frequently in contact with the channel bottom, enhancing the capture efficiency by the magnetic filter.[97,98] The channel height, therefore, is no longer limited by the reach of the magnetic field into the flow channel, and tall channels could be implemented to increase the throughput while reducing fluidic resistance. Second, the structural strength of the size-sorter is reinforced by embedding a thin glass slip in the channel top (Fig. 2.1c). By providing rigid support to the physical barrier, this design helps

the size-sorter maintain a consistent gap height during high flow-rate operation, and thus minimizes potential escape of CTCs.

Figure 2.1e shows a prototype HMSS device. To fabricate the magnetic layer, we first suspended NdFeB particles (MQFP-B-20076, Magnequench) in uncured PDMS (polydimethylsiloxane, Dow Corning), and magnetized them using a high-field magnet (~1.5 T). The mixture was then slowly cured (~3 hours) to allow NdFeB grains to self-assemble. The fluidic mold had three layers that defined the underpass-gap (5 μm in height), fluidic channels, and herringbone mixers (see Materials and Methods for design details). Prior to PDMS curing, a thin glass slab (150 μm thick) was placed above the cell capture unit. The HMSS was then assembled by permanently bonding the magnet layer with the fluidic structure. The channel inside of the fabricated devices was treated with F127 Pluronic copolymer (Sigma Aldrich) to minimize non-specific cell adhesion.[99] Liquid injection (e.g., cell suspension, antibody-mixture) was driven by an external peristaltic pump.

2.2.2. System Operation

The sequence of HMSS operation is demonstrated in Fig. 2.2. Samples were prepared by spiking ~5000 cancer cells (HT29, colorectal adenocarcinoma) into RBC-lysed whole blood samples (1 mL). Prior to the mixing, cancer cells (HT29, colorectal adenocarcinoma) and human leukocytes were stained in red (Cell Tracker Red CMPTX, Life Technologies) and blue (Hoescht 33258, Invitrogen) respectively. Samples were then incubated with CD45-specific magnetic particles (EasySep® CD45 Depletion Cocktail) to label leukocytes (see Materials and Methods for details). In the initial cell mixture (Fig. 2.2a), cancer cells (red) were difficult to detect due to the presence of abundant leukocytes (blue). Following the negative depletion of leukocytes with the magnetic filter, cancer cells were efficiently enriched (Fig. 2.2b). The size-sorter then collected cancer cells along the capture sites, which allowed for easy single cell

identification and counting (Fig. 2.2c). Note that the entire assay was performed without off-chip washing steps; after incubating samples with leukocyte-specific magnetic particles, the mixture was flown through the HMSS chip to complete the assay. Such on-chip processing minimized potential cell-loss and simplified the system operation.

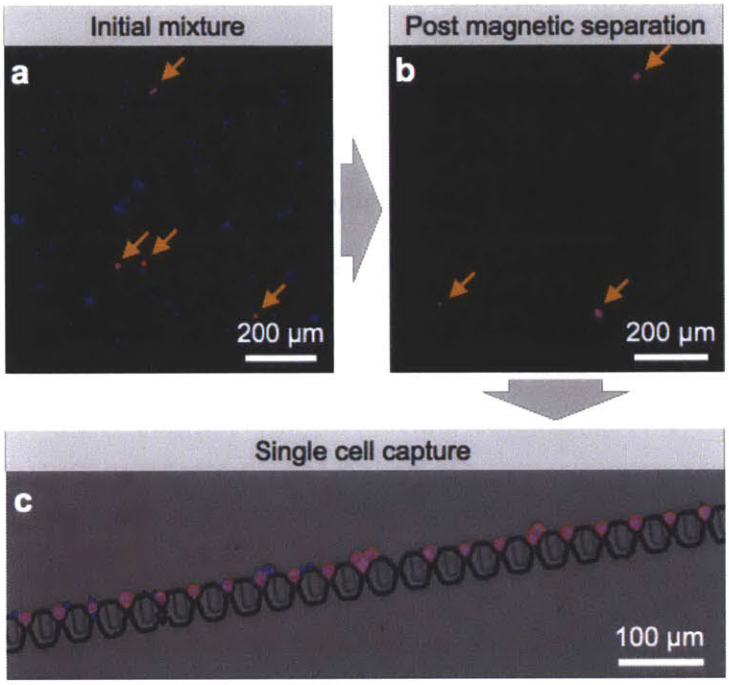

Figure 2.2. Operation of the HMSS chip. Following the magnetic labeling of leukocytes, samples are introduced into the HMSS chip for one-step CTC isolation. (a) Before the magnetic depletion, the initial sample was highly heterogenous, and cancel cells (arrows) were difficult to find. (b) After the depletion of leukocytes by the magnetic filter, cancer cells were significantly enriched. (c) The size-sorter (gap height, 5 μm) further trapped cells at predefined capture sites for easy cell counting. Captured cells could be further stained on-chip. Cancer cells and leukocytes were pre-stained in red and blue, respectively, for visualization.

2.2.3 Device Characterization

The performance of the HMSS chip was evaluated by determining two parameters, enrichment ratio and recovery rate. The enrichment ratio was defined by measuring how many times the population of non-magnetic cells (e.g., cancer cells) is enhanced relative to that of

magnetically-labeled host cells (e.g., leukocytes). The recovery rate, which measures how many target cells are inadvertently trapped by the system, was obtained from the relative changes of target cell population before and after HMSS operation.

We first assessed the effect of chaotic mixing on target cell enrichment. Computational simulation revealed that magnetic objects in the mixing channel can be more effectively captured by the magnetic filter than those in the laminar flow device (Fig. 2.3a). This trend was more pronounced at higher flow rate. In the laminar flow system, high speed objects could easily escape the magnetic filter region before significantly pulled down towards the channel bottom. Inside the herringbone channel, however, particles were forced to make frequent contact with the channel bottom. Consequently, the chaotic mixer system could maintain a consistent capturing efficiency even at higher flow rate (Fig 2.3b).

To test the computational prediction, we fabricated two types of magnetic filter chips that were with and without herringbone structure. Samples were prepared by adding ~10^3 cancer cells (HT29) in RBC-lysed blood (1 mL) and subsequently labeling leukocytes with magnetic particles (Materials and Methods). Samples (1 mL) were then introduced to the devices at the flow rate of 3 mL/hr. The number of leukocytes before and after magnetic depletion was measured by flow cytometry. As expected, the herringbone pattern-assisted magnetic filter achieved significantly higher (> 30-fold) enrichment ratio (~1800) than the simple-laminar flow device (enrichment ratio: ~50; Fig. 3b); this could be attributed the increased frequencies of cell-magnet interactions by the chaotic advection. Furthermore, the capture efficiency was stable over wide range of flow rates. For instance, even though the flow rate of whole blood samples were varied from 1 to 12 mL/hr, the overall enrichment ratio remained nearly constant with values >10^3 (Fig. 2.3c).

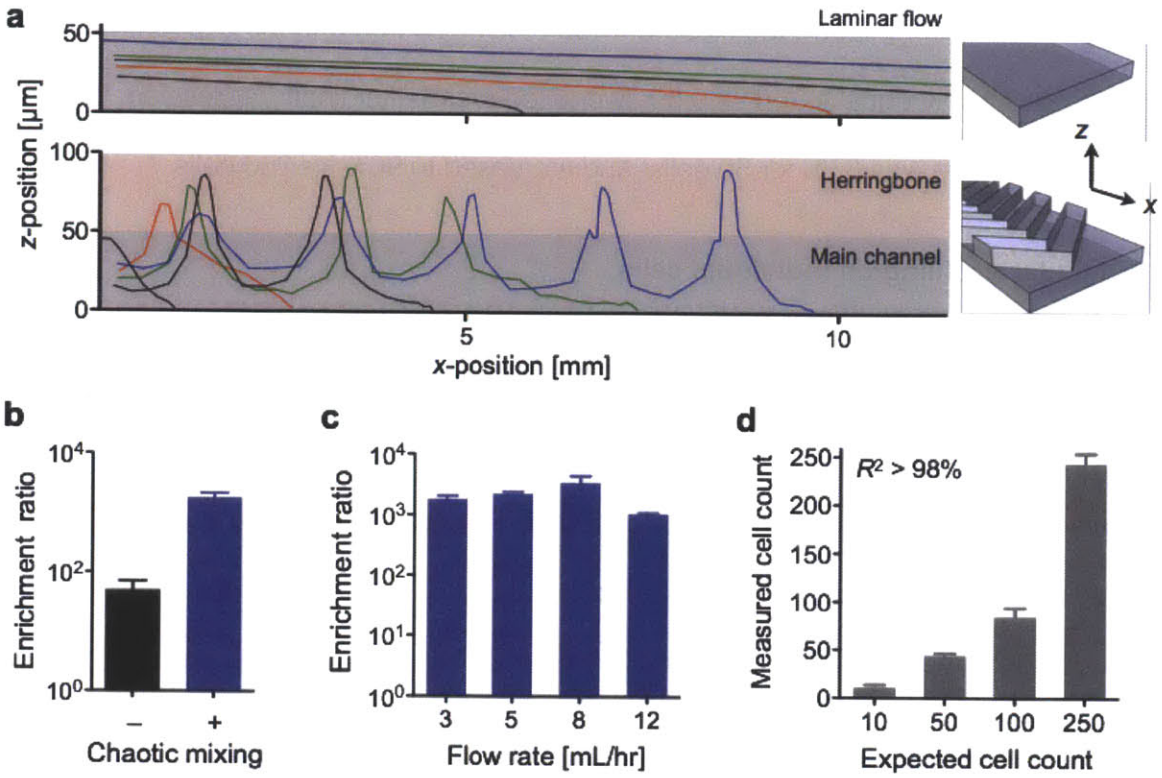

Figure 2.3. Characterization of the HMSS-sorter. (a) Computational simulation of magnetic capture in the laminar (top) and the chaotic (bottom) fluidic systems. Magnetic objects inside the chaotic mixer more frequently contact the magnet surface, leading to higher capture yield. (b) Comparison of enrichment ratios with and without chaotic mixing. The enhancement due to the chaotic mixing is > 30 fold. (c) Enrichment ratios at varying flow rates. Consistent cell-enrichment (>10^3 enrichment ratio) could be achieved at various flow rates. (d) Titration experiments. Known amounts of cancer cells were spiked in blood and were captured by the HMSS. The measured counts shows good with the expected numbers. Data is displayed as mean ± SD from triplicate (b, c) and quintuplicate (d) measurements.

We next characterized the recovery performance of HMSS chip. Blood samples (10 mL) containing varying concentrations of cancer cells (HT29; 10, 50, 100 and 250 cells/mL) were prepared. Leukocytes were then magnetically labelled, and samples (1 mL) were introduced to the HMSS chip at the flow rate of 5 mL/hr. Cancer cells, that were trapped at pre-defined capture sites, were enumerated. The measured cell counts showed excellent agreement with

expected cell counts (Fig. 2.3d); the slope between the measured and the expected cell counts was statistically equal to 1 ($P > 0.59$, two-tailed t-test) after linear regression. The average recovery rate was 87% for 50 cells, and increased to 96% for 250 cells.

2.2.4 Molecular profiling on individual cells

The HMSS chip can be an effective platform not only for CTC isolation and counting, but also for its characterization. By flowing a mixture of molecular probes, captured cells can be molecularly screened at a single cell resolution. As an representative example, we profiled the expression of EpCAM (epithelial cell adhesion molecule) and vimentin in tumor cells. These markers were chosen for their clinical implications: EpCAM is a widely-used epithelial marker for CTC isolation; vimentin is a mesenchymal marker whose level is up-regulated during the epithelial-to-mesenchymal transition of CTCs.[94,100] Samples were prepared by spiking different types of cancer cells (SW872, liposarcoma; SKOV3, ovarian serous adenocarcinoma; MCF-7, breast adenocarcinoma) into whole human blood (see Materials and Methods for details). Following the cell enrichment and trapping, a cocktail of fluorescent probes were introduced to stain captured cells for nucleus, EpCAM and vimentin. The assay revealed distinct marker profiles among different cell lines (Fig. 4a). For the epithelial cancer cells (SKOV3, MCF-7), EpCAM expression was strongly positive; vimentin was positive in SKOV3, but was negative in luminal-like MCF-7, which is consistent with previous reports.[101,102] The mesenchymal cancer cells (SW872), on the other hand, were stained positive for vimentin and negative for EpCAM.

The HMSS also facilitated molecular analyses at the single cell level. For instance, Fig. 2.4b shows the expression profiling of Ki-67, a cell-proliferation marker, in A431 cells (epidermoid carcinoma) spiked into whole human blood. With the cancer cells stably trapped in the HMSS, we could resolve nuclear localization, and heterogeneity amongst cells. Some cells showed strong Ki-67 staining, suggesting their high proliferative potential. Proliferative markers such as

Ki-67 have been shown to correlate to disease progression and survival; dual staining of CTCs with PSA and Ki-67 in prostate cancer patients showed a broad range of proliferative index in CTCs, even under castrate conditions.[86] Note that other diagnostic markers could be readily incorporated into the HMSS platform, including DNA damage markers (e.g., histone γH2AX) and signaling proteins (e.g., phosphorylated EGFR).[103,104] Such multiplexed assays on CTC molecular status would be of significant clinical importance in monitoring and rationalizing patient treatment.

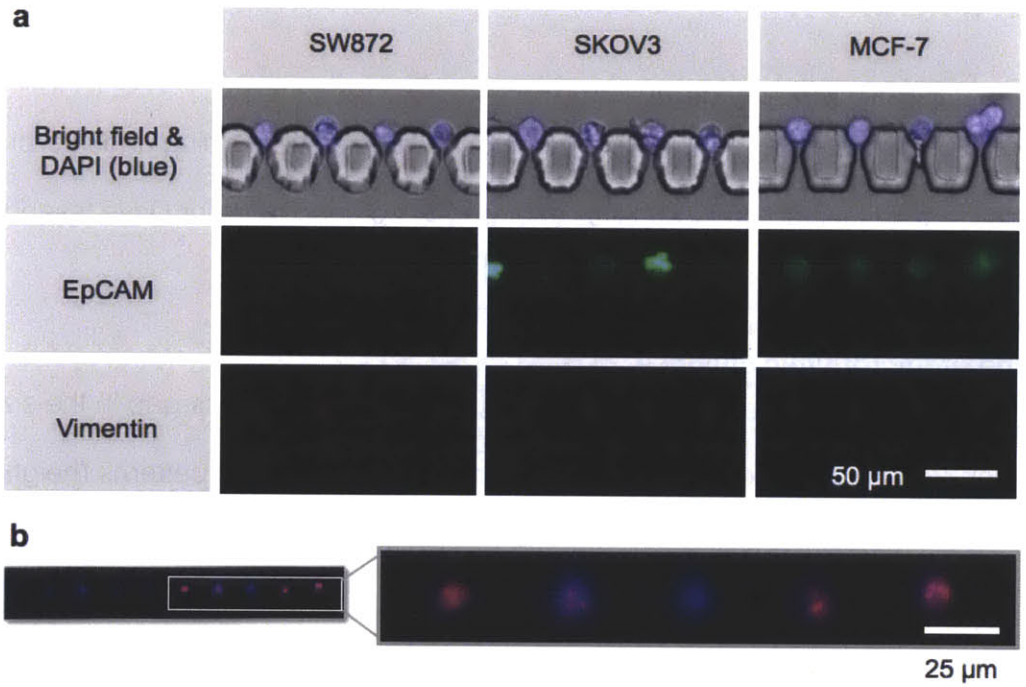

FIgure 2.4. On-chip analyses on captured cancer cells. (a) Molecular analyses on on three different types of cells (SW872, SKOV3, and MCF-7) showed differential staining of EpCAM and vimentin. The staining was performed on-chip after capturing cancer cells in whole blood. DAPI, 4',6-diamidino-2-phenylindole. (b) With cancer cells stably trapped, the HMSS facilitated the identification and higher resolution imaging of individual cells. Ki-67 staining of A431 cells revealed subcellular nuclear localization and heterogeneity amongst cells.

2.2.5 Conclusion

In summary, the HMSS is a promising tool for CTC detection and analysis. The integration of two distinct cell separation technologies, namely a self-assembled magnetic filter and a size-

based sorter, allows the efficient isolation of CTCs in an unbiased manner. Subsequent on-chip profiling enables cellular studies at single cell resolution. Furthermore, by optimizing the fluidic design, we have significantly improved the throughput and the cell-capture accuracy. With such advanced features, the HMSS chip could play an important role in translational cancer research. We plan on using the HMSS system with clinical samples to look at a variety of markers that are relevant to pathway inhibition in molecularly targeted treatments. Ultimately, we envision that the technological advancements in HMSS device would aid in understanding the underlying biology of CTCs as well as in establishing their clinical utility.

2.2.6 Personal Contribution to Work

The author of this thesis led a group of researchers in planning, performing and interpreting experiments in equal collaboration with Dr. Jaehoon Chung and Professor Dave Issadore.

2.3 Materials and Methods

2.3.1 Design of microfluidic channel

The fluidic system had a triple-layer structure that defined the underpass-gap in the size sorter (5 μm in height), fluidic channel (height, H_C = 50 μm), and herringbone patterns (height, H_H = 50 μm). The main microfluidic channel in the magnetic filter region consisted of 64 parallel mixing channels (width, W_C = 380 μm). The dimension of herringbone mixer was chosen according to the previous report[98] to maximize the events of suspended cells contacting the channel bottom (see Fig. 2.5a for details). Cell capturing structure was implemented in the size sorter region (Fig. 2.5b). The capture sites were designed to trap even small cancer cells (> 5 μm in diameter).

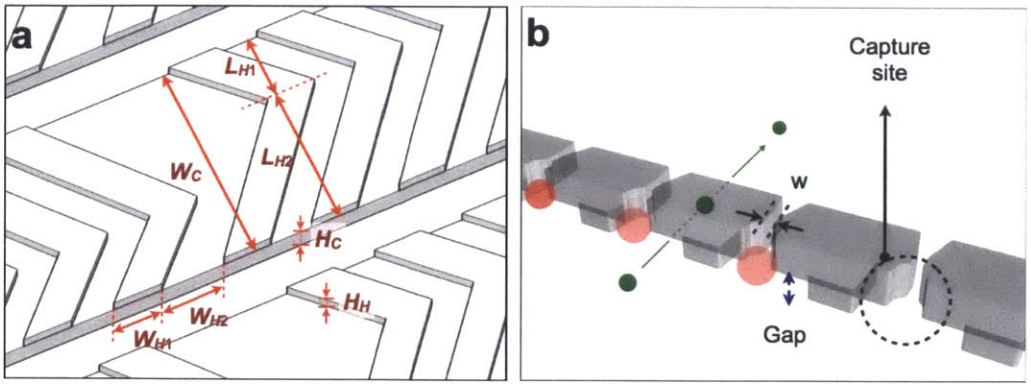

Figure 2.5. Fluidic structures in HMSS. (a) Design parameters for the herringbone mixer: W_C = 380 μm; H_C = 50 μm; L_{H1} = 250 μm; L_{H2} = 130 μm; W_{H1} = 150 μm; W_{H2} = 150 μm; H_H = 50 μm). (b) Dimension of capture sites in size-sorter: gap height, 5 μm; w = 7 μm.

2.3.2 Sample preparation

Samples were prepared by following the workflow shown in Fig. 2.6. For the device characterization, we used RBC-lysed human blood, which facilitated the staining of leukocytes (Fig. 2.6a). For the molecular staining experiments, we used human whole blood (Fig. 2.6b).

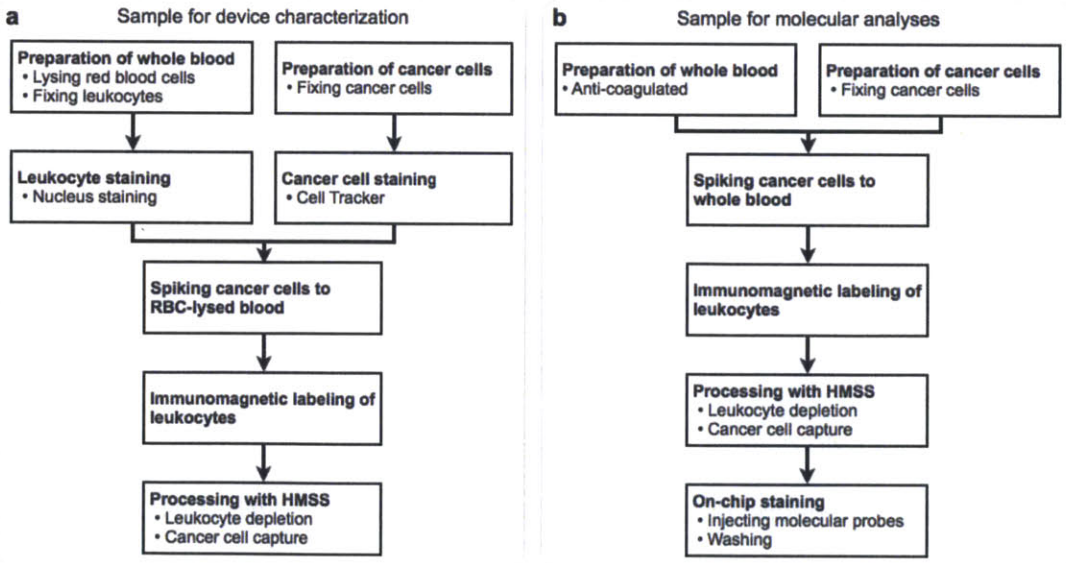

Figure 2.6. Sample Processing Workflow. Sample preparation steps for device characterization (a) and on-chip molecular analyses (b).

Preparation of RBC-lyses blood: Human whole blood were lysed and fixed with pre-warmed 1x Lyse/Fix (BD Biosciences) for 10 minutes , shaking at 37 °C. Samples were then washed twice with PBS+2% BSA. Leukocytes were labeled blue by adding Hoescht 33258 (Invitrogen) (1:2000 dilution).

Preparation of cancer cells: Cancer cells (HT29) were pre-fixed in the same manner as described above. The fixed cells were then labeled with Cell Tracker Red CMPTX (Life Technologies) at 25 μM.

Magnetic labeling of leukocytes: Leukocytes were labeled using EasySep™ Human CD45 Depletion Kit (Stemcell Technology). First, EasySep® CD45 Depletion Cocktail at 100 μL/mL cells (e.g., for 1 mL of cell suspension, add 100 μL of cocktail) was added in prepared whold blood. The mixture were incubate at room temperature for 15 minutes. EasySep® Magnetic Nanoparticles were then added and mixed at 220 μL/mL cells for 10 minutes.

Demonstration of system operation (Fig. 2.2): Pre-stained red-fluorescent HT29 cells (~5000) were spiked into RBC-lysed blood (1 mL), and leukocytes were magnetically labeled. Without washing, the mixture (1 mL) was introduced to the HMSS device at the flow rate of 3 mL/hr. The operation was monitored with an inverted fluorescent microscope (Nikon Eclipse Ti).

Enrichment testing (Figs. 2.3b,c): Samples were prepared by adding ~1000 cancer cells into RBC-lysed blood (1 mL). The numbers of cancer cells ($N_{c,i}$) and leukocytes ($N_{L,i}$) were measured using a flow cytometer (LSRII, BD Biosciences), before (i = 1) and after (i = 2) the magnetic depletion. The enrichment ratio was then obtained as $(N_{C,2}/N_{L,2})\cdot(N_{C,1}/N_{L,1})^{-1}$.

Titration experiments (Fig. 2.3d): Confluent cancer cells in culture were suspended ($>10^7$ cells/mL), and the cell concentration was determined through standard hemacytometer cell counting. We then serially diluted (10×) the stock solution. Final samples were then prepared by separately adding a precise volume of dilution series into 10 mL of RBC-lysed blood. The

final concentrations of cancer cells were 10, 50, 100 and 250 cells/mL. Note that this approach minimized the logistic errors coming from pipetting. For each experiment, we used 1 mL of prepared samples. The cancer cells captured by the HMSS were counted via microscopy.

2.3.3. Samples for on-chip molecular analyses

On-chip staining of EpCAM and vimentin (Fig. 2.4a): Three cell lines (SW872, liposarcoma; SKOV3, ovarian carcinoma; MCF-7, breast adenocarcinoma) were chosen for their varying expression levels of EpCAM and vimentin. Cells in culture (~70% confluence) were detached and subsequently fixed as described above.Whole blood was obtained from healthy volunteers and placed in tubes containing ethylenediaminetetraacetic acid (Becton Dickinson, Franklin Lakes, NJ). Approximately 3500 of cancer cells were added in 3.5 mL of whole blood. After the magnetic labeling of leukocytes (see above), samples were flown to the HMSS device at the flow rate of 3 mL/hr. Captured cancer cells were then stained on-chip by injecting a cocktail of molecular probes (0.1 mL/hr, 6 hours). Following probes were mixed: Hoescht 33258 (Invitrogen), a vimentin (D21H3)-Alexa Fluor® 555 antibody (Cell Signaling) and an EpCAM (VU1D9)-Alexa Fluor® 488 antibody (Cell Signaling). These probes were suspended in 1× Perm/Wash buffer (BD Biosciences) supplemented with 2% BSA (PW+). The final concentration of each antibody was 2 μg/mL. After staining, cells were washed on-chip by flowing PW+ buffer (0.1 mL/hr, 30 min), and imaged under an inverted microscope (Nikon Eclipse Ti).

On-chip staining of Ki-67 (Fig. 4b): Cancer cells (A431, epidermoid carcinoma) were cultured to 70% confluence, detached and fixed, following the same protocol described above. Cells were then pre-stained with 1:2000 Hoescht 33258 (Invitrogen). Approximately 1000 cancer cells were mixed into whole blood (3.5 mL), and the prepared samples were processed by the HMSS. We first treated the capture cancer cells with PW+ buffer (0.5 mL/hr, 30-40 min) to permeabilize their membrane. Next, Ki-67 antibody (BD Biosciences) in PW+ buffer (1 μg/mL)

was introduced (0.1 mL/hr, 8 hours). FITC- labeled secondary antibody (4 µg/mL) against Mouse IgG1 (BD Biosciences) was then injected (0.1 mL/hr, 1 hour), followed by a final wash with PW+ (1 hour).

I Chapter 3 I Nano-assay to Study Target-Drug Binding

Parts of this chapter are from Ullal, et. al. "Nanoparticle-mediated measurement of target-drug binding in cancer cells." *ACS Nano.* 5(11), 2011.

3.1 Introduction

Nanomaterials have become an indispensable tool in the development of clinical diagnostics[37,105,106], single cell analysis[107,108] and systems wide analysis of clinical specimen.[109] They can be easily modified with multivalent targeting ligands to amplify signals,[110] improve avidity, [107,108] enhance binding,[111] and translate molecular interactions into measurable electrical, optical or magnetic signals. In particular, magnetofluorescent nanoparticles allow for dual read-outs by optical (e.g. flow cytometry, immunofluorescence) and magnetic sensing (e.g. nuclear magnetic resonance or magnetoresistive detection). Dextran-coated, cross-linked iron oxide (CLIO) nanoparticles have been shown to be ideal for use with clinical samples as they are highly stable in physiological buffers and can be easily detected by NMR measurements with low biological background. Recently, our group leveraged these properties to profile scant cells from fine needle aspirate[37] and to enhance detection of rare circulating cancer cells. Most nanoparticle-based diagnostic applications have primarily used antibodies as affinity ligands to detect whole cells,[37] pathogens,[73,112] soluble protein biomarkers[113] or metabolites.[114]

One major unexplored application, has been the use of nanomaterials to quantitatively assay drug-target binding in clinical samples. Though clinical samples are readily procured during routine medical procedures, samples often have scant cells with short half-lives once harvested,[86] thus necessitating a point-of-care assay with minimal sample processing. Tools to quantify target-binding in a given patient at a given dose could help in screening drug candidates during pharmaceutical development[115] and also impact treatment decisions made in the clinic. Ultimately such assays would significantly aid in determining whether systemically administered drugs have

reached and occupied their intended cellular targets and how target binding varies across patients who may have acquired drug resistance.

In order to enable fast, point-of-care assessment of drug-target interactions, we designed nanosensors that could be adapted to study many drug-target systems which are quickly assayed by a portable diagnostic NMR system (DMR)[73,116]. Specifically, we hypothesized that by constructing a single small molecule drug-nanoparticle conjugate that could compete with corresponding free small molecules for their targets, one could gain insights into the molecular binding action of the drugs. Given the vast repositories of small molecules drugs, nanosensors could thus be developed for a variety of targets. Furthermore, we reasoned that the drugs themselves could serve as "affinity ligands", and aimed at establishing a new biomarker detection paradigm distinct from antibodies.[107] Unlike antibodies which show binding specificity for single antigenic sites within a given protein, small molecule drugs bind to specific conformations (e.g. catalytic sites) and often show broader specificity. Using the drug itself as a probe allows for a combined read out of multiple relevant targets all of which may affect drug efficacy.

As a model system, we selected poly(ADP-ribose) polymerase (PARP) inhibition, and conjugated the PARP inhibitor Olaparib (AZD-2281) to magnetic nanoparticles. Several PARP inhibitors have made significant headway in pre-clinical and clinical trials for ovarian and breast cancer.[117-120] Moreover, the binding kinetics of PARP inhibitors are particularly interesting as they have been designed to mimic nicotinamide and competitively block binding at specifically the PARP1 and PARP2 catalytic sites.[121] Using the PARP nanosensor, we performed validation experiments, comparative drug inhibition studies and testing in whole blood samples without the need for prior purification. We show that the method is fast, sensitive and well suited for point-of care operation. The ability to measure target binding of an increasing number of molecularly targeted drugs should

have a range of applications in biomedicine, drug development, clinical trials and for routine patient care.

3.2 Results and Discussion

3.2.1 Synthesis and characterization of the PARP nanosensor

Based on earlier findings that the 4-NH-piperazine functionality of AZD2281 tolerates bulky substituents without significant decrease in binding affinity,[122-124] we chose this site to immobilize the small molecule. For this reason, carboxyl-functionalized precursor **1** was reacted with N-hydroxy succinimide in the presence of a carbodiimide resin, yielding the amine reactive NHS ester activated AZD2281 derivative AZD2281-NHS **2** (Fig. 3.1a). HPLC, ESI-MS and HRMS spectra confirmed both identity and purity of the isolated product. AZD2281-NHS was converted to PARPi-NP **3** by addition of amine-terminated CLIO nanoparticles (Fig. 3.1a). Each nanoparticle had approximately 70 drug molecules covalently attached, which corresponds to near complete conversion of free amine groups on each particle. The AZD-2281 conjugated nanoparticles (PARPi-NPs) were highly stable in solution (>6 months) without detectable aggregation, as determined by dynamic light scattering (mean diameter: 40.1 nm). Control NPs used for all studies were succinylated, but otherwise identical. Carboxylic acid modified AZD-2281 had an IC_{50} of 6.7 nM, similar to that of the reported free AZD-2281 drug (5 nM).[122,125] Following conjugation to the nanoparticle, the construct retained inhibitory activity against PARP1 with a measured IC_{50} of 3 nM (Fig. 3.1c). Importantly, none of the control nanoparticles (either the succinylated or amine precursor CLIO) showed any inhibition of PARP activity.

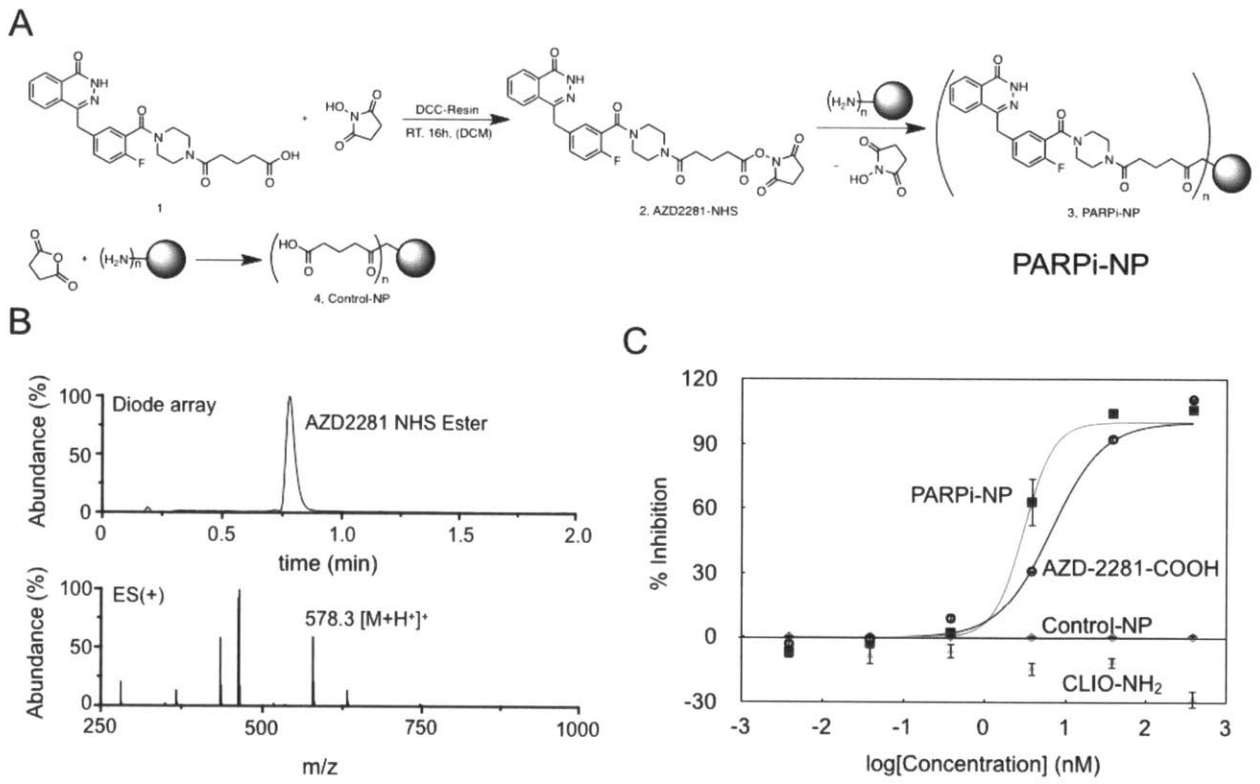

Fig. 3.1. Synthesis and Characterization of Small Molecule Nanoparticle. a) AZD-2281 was modified to have an NHS-ester and reacted with magnetic nanoparticle (CLIO-NH_2) for 4 hours in PBS. Control nanoparticle was created by reacting succinic anhydride with CLIO-NH_2 overnight. b) HPLC and ESI-LC/MS traces of the AZD2281 NHS Ester. c) AZD-2281 remained active even after conjugation to CLIO as verified by a PARP activity assay. $IC50_{AZD\text{-}COOH}$ = 6.685 nM (5.087 to 8.786 nM IC50 95% confidence interval; R^2 = .9816); $IC50_{PARPi\text{-}NP}$ = 3.071 nM (1.643 to 5.740 nM IC50 95% confidence interval; R^2 = .9723). Control and unconjugated nanoparticles did not have any inhibitory effect.

3.2.2 Validation of the drug nanosensor in cell lines

To test whether our drug nanosensor could measure PARP expression, we selected five cell lines (HT29, HeLa, MDA-MB-231, MDA-MB-436 and HEK293 cells) that have varying PARP1 expression levels as confirmed by Western Blotting (Figs. 3.2a, b). Cells were fixed, permeabilized, and then incubated with either PARPi-NP or control-NP. The PARPi-NPs had an average diameter of about 40 nm, which is slightly larger than an unconstricted, open nuclear pore size of 30 nm.[126] However, once permeabilized, nanoparticles are able to freely enter the cell by diffusion for both nuclear and cytoplasmic targets.[127] Incubation times and nanoparticle concentrations were

selected to achieve maximal target binding from the PARPi-NP with minimal background from the control-NP. PARPi-NPs showed tight binding to the target with little decrease in signal over time. Following the removal of excess NPs, samples were processed by the DMR system to determine their transverse relaxation time (T_2). The measured T_2 values were converted to R_2 (=1/T_2) and normalized to PBS and control-NP samples to obtain the PARP1 cellular expression level (Fig. 3.2c). Fig. 3.2d shows excellent correlation between DMR magnetic measurements and PARP1 expression levels as determined by Western Blots (r^2= 0.92) and flow cytometry (r^2= 0.97). DMR measurements were performed with 10,000 cells for validation studies; however, in subsequent experiments signals were detected in as few as 1,500 cells. In addition to PARP-1 measurements, we also determined PARP2 expression levels by immunoblotting (Fig. 3.2b). However, correlation of PARPi-NP to expression was dominated by PARP1, likely due to the much higher abundance of PARP1 as compared to PARP2 in the selected cell lines.

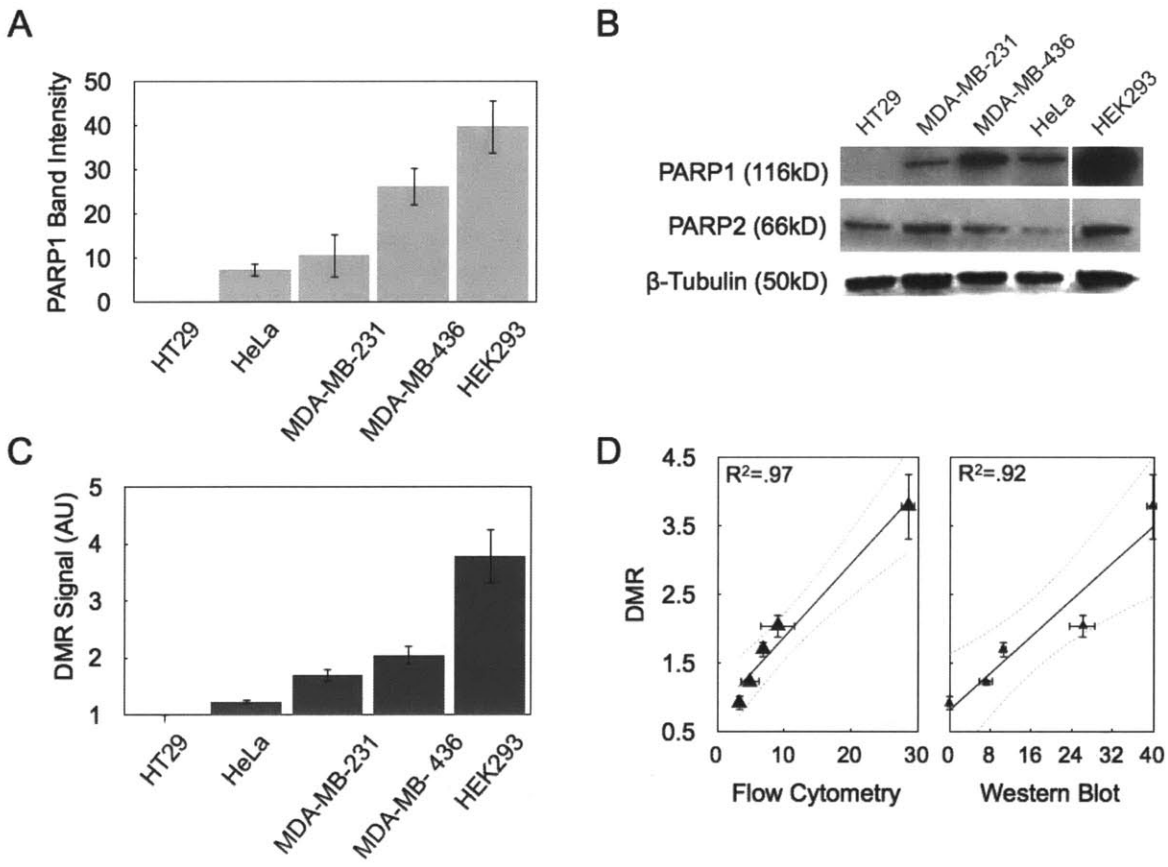

Fig. 3.2. AZD2281-NP Measurement of PARP expression. a) Cell lines were screened for PARP1 expression by immunoblotting and five were selected with varying levels of PARP expression. Expression was quantified from three separate blots and plotted normalized to HT29 expression. b) A representative Western Blot showing PARP1 and PARP2 expression. c) PARPi-NP was applied to the same cell lines to quantify binding to total PARP. Changes in T_2 relaxation time were measured by DMR to measure the amount of magnetic nanoparticle present. Signal of the nanoparticle (S_{NP})was calculated as $R_{2,\,NP}$ - $R_{2,\,PBS}$)/($R_{2,\,PBS}$) -1). The amount of magnetic particle present was then determined by dividing by the amount of background as assessed by the control-NP ($S_{PARPi\text{-}NP}$ /$S_{Control\text{-}NP}$). Data shown is in biological duplicate. from three separate DMR measurements and is normalized to HT29 signal. d) PARPi-NP was also optically assayed using flow cytometry and shows high correlation to DMR measurements (R^2=0.97). DMR measurements also had high correlation (R^2=0.92) to PARP1 expression from immunoblotting. Dotted lines represent 95% confidence intervals.

We next used microscopy to further assess quantitative measurements by examining the intracellular localization of nanosensor and drug targets. In HEK293 cells with high PARP expression (Fig. 3.3a), there was excellent co-localization between intracellular PARP1 antibody and PARPi-NP (co-localization correlation = 0.8). The nanosensor showed strong nucleolar and and nuclear localization, which is consistent with PARP1 subcellular organization as previously found using PARP1 expressing cell lines[128,129] or AZD-2281 as a fluorescent probe.[124] Similar trends were observed in HeLa cells, which have moderate PARP1 expression. In HT29 cells which have little PARP expression, both the PARP1 antibody and PARPi-NP showed negligible signal. The control-NP showed little to no background (Fig 3.3b).

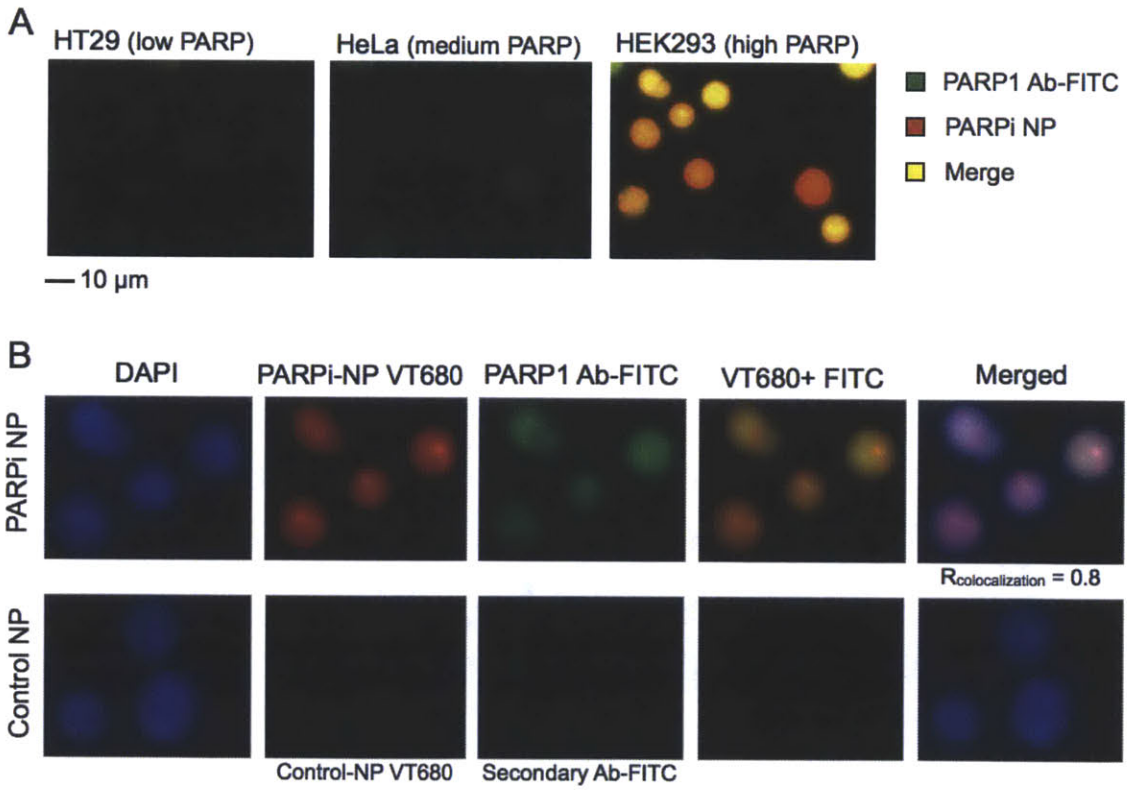

Fig. 3.3. Immunofluorescence of PARPi-NP. a) Differences in PARP expression could be seen using PARPi-NP and immunofluorescence. Experiments were performed in biological duplicate. PARP1-Ab is

shown in green; PARPi-NP is shown in red, and the merge is displayed in yellow. Here, representative images show that the low PARP expression cell line, HT29 had hardly any PARPi-NP, and low PARP1-Ab binding (mostly background). HeLa cells had slightly more PARP, and respectively PARPi-NP. Finally, high PARP expressing HEK283 cells showed high amounts of PARPi-NP and PARP1-Ab. b) Strong colocalization of PARPi-NP and PARP1-Ab were seen (Colocolization Correlation = 0.8). The control-NP had low background with negligible signal.

3.2.3 Nanosensor testing of different small molecule PARP inhibitors

Most small molecule PARP inhibitors work by competitively inhibiting nicotinamide (NAD+) at the PARP catalytic site.[130] We chose 5 different, commercially available PARP inhibitors (Fig. 3.4) to test whether the nanosensor-DMR measurements could be used to determine IC_{50} of each of the different drugs. Briefly, cells were incubated with varying doses of a PARP inhibitor. Subsequently, PARPi-NPs were added to detect the number of unoccupied PARP targets. The entire assay was performed in less than 90 minutes and required only 10,000 cells. The key PARP inhibitor, AZD2281 showed an IC_{50} of 1.14 nM and was able to effectively compete the PARPi-NP in a homologous binding competition assay (Fig 3.4). AG-014699 which has high structural similarity to AZD-2281 also displayed very tight binding with an IC_{50} of 0.67 nM. The heterologous competitive binding curve with ABT-888 (Velaparib), another competitive PARP inhibitor, showed an IC_{50} of 9.5 nM. This data suggests that ABT-888 may have a faster off rate than that of PARPi-NP, in turn allowing the PARPi-NP to occupy more PARP sites for a given concentration of free ABT-888. Furthermore, unlike AZD-2281, ABT-888 has been reported to have a slightly stronger binding affinity for PARP-2 as opposed to PARP-1 due to a stronger interaction with alpha-helix-5 in the PARP-2/ABT-888 co-crystalstructure.[131] This difference in binding affinity for the two PARP targets could also explain why it has less of a competitive effect on the PARPi-NP compared to AZD-2281 or AG-014699. The weak PARP inhibitor, 3-aminobenzamide, which is similar in structure to NAD+ only showed a competitive effect at extremely high doses (IC_{50}=29.5 μM). As a negative control, we also demonstrated that the non-competitive inhibitor BSI-201 (4-iodo-3-nitro-benzamide), which

has a distinct pharmacophore and acts by ejecting the first zinc-finger of the PARP1 protein,[132] does not block PARPi-NP binding even at high doses. These results indicate that the nanosensor can indeed be used to quantitate target inhibition in competitive experiments.

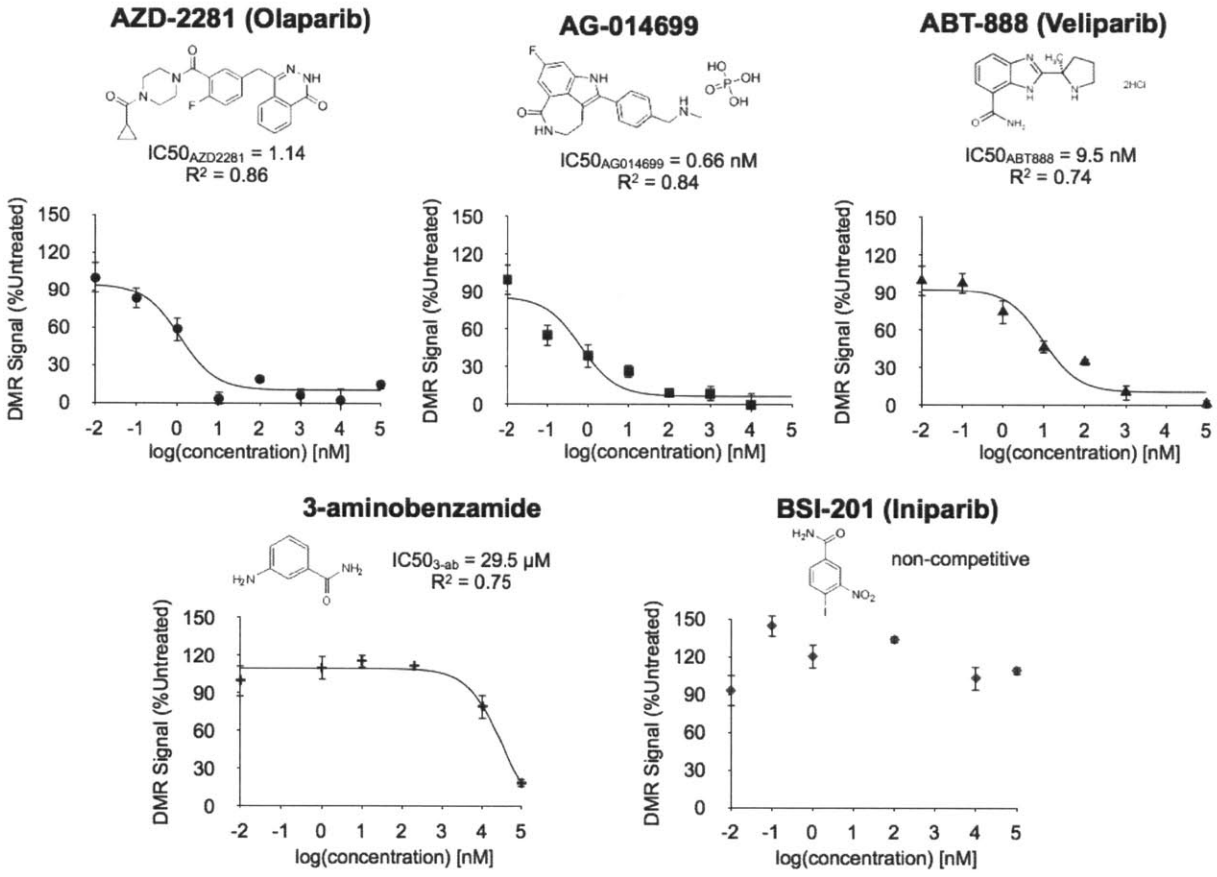

Fig. 3.4. Competitive Binding Curves of PARPi-NP with various PARP inhibitors. Competitive binding assays were performed by incubating selecting PARP inhibitors that have been designed to compete with Nicotinamide at the PARP1 and PARP2 catalytic pockets (AZD2281, AG04699 and ABT888). Another weak competitor, 3-aminobenzamide was selected, as well as the non-competitive inhibitor BSI-201 as a negative control. Free PARPi was added at various doses for 30 minutes before addition of the PARPi-NP or Control-NP (15 µg Fe/ml). After 20 minutes of incubation and washing, signal was read magnetically using DMR. Competitive binding curves were fitted using Prism (GraphPad); AZD-2281 had an IC50 of 3.4 nM (R^2=.86), AG014699 had an IC50 of 7.0nM (R^2=.84), and ABT-888 had an IC50 of 257nM(R^2=.88). 3-aminobenzamide was only weakly competitive and BSI-201 had no competitive effect. Experiments were

performed on three separate occasions and represent at least biological duplicate. Fluorescence measurements of the assay

3.2.4 Drug Inhibition in Live Cells and Blood Samples

A number of strategies are currently used to measure target binding, including fluorogenic assays, ELISA, radioimmunoassays, mass spectrometry, SILAC, surface plasmon resonance and isothermal calorimetric measurements. These methods typically require purified target protein which necessitates a large number of cells and makes it difficult to perform assays under biologically relevant conditions. Consequently, few of these methods are ever performed in a clinical setting where there are time constraints, complexities in obtaining clinical samples, and limited numbers of cells.

The simplicity and the robustness of the nanosensor confer potential for the assay to be an effective platform to directly assess drug binding efficacy in patient samples. To evaluate its clinical utility, we measured target inhibition of AZD-2281 in mock clinical samples. Specifically, the ovarian cancer cell lines A2780, OVCAR429 and UCI-101 or the breast cancer cell line MDA-MB-231 were spiked into human whole blood. The samples were immediately treated with AZD-2281 drug at three different doses: 0 (probing dose), 150 nM (testing dose), and 1.5 μM (saturating dose). We used this "three-dose assay" rather than a full dose response curve (see Fig. 3.4) to speed up analysis and preserve valuable scant clinical samples. After removing excess AZD-2281, the PARPi-NPs were used to probe PARP sites unoccupied by the free drug (Figure 3.5a). Finally, cancer cells were isolated using CD45 negative selection to remove host cells. While all prior *in-vitro* validation DMR assays were performed with 10,000 cells, signals from whole blood samples were detected with as few as 1,500 cells. This detection level is promising for clinical samples such as fine needle aspirate where one obtains about 1,500 per pass.[133] Though host cells (CD45+)

showed little to no uptake of the PARPi-NP, CD45 negative selection was necessary to reliably detect changes in signal from the PARPi-NP after drug inhibition.

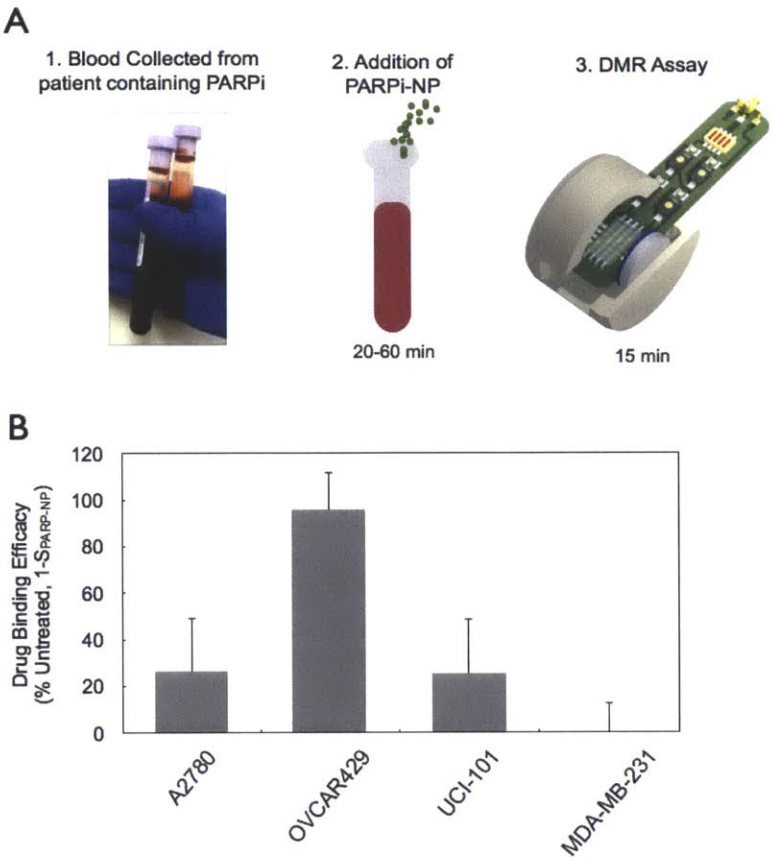

Fig. 3.5. Drug Binding Efficacy in Whole Blood Samples . a) A schematic of a clinical drug binding assay from whole blood samples. Mock clinical samples were prepared by spiking cancer cells into human whole blood. This sample was directly incubated with AZD-2281 before the PARPi-NP was added. Quick read-out could then be performed with DMR and/or flow cytometry. b) Drug binding levels were determined by looking at the inverse percent change in PARPi-NP from treated versus untreated samples. Data shown is an example of "Binding Efficacy" by taking the ratio of drug bound at the test dose to the saturating dose. OVCAR429 showed the highest drug binding at the test dose, and thus had a binding efficacy measure of 0.94. In contrast, no drug was bound to MDA-MB-231 at the test dose resulting in a binding efficacy of 0.00.With further experiments and validation, such a measure could be used as a simple diagnostic to dictate treatment choices in the clinic such as choice or dose of drug.

The result at the probing dose ([AZD-2281] = 0 nM) revealed differences in PARP expression across the cell lines, which could serve as a predictive biomarker for initiating treatment. Indeed, prior work has correlated PARP levels to treatment sensitivity and patient outcome.[134,135] The drug binding levels at the testing and saturating doses were then estimated by comparing R_2 values between drug-treated and untreated samples. At the saturating dose, the binding levels reached a near maximum of 70% in almost all cell lines, except A2780 which showed only moderate drug binding (~40%). At the test dose, however, drug binding levels varied significantly across tumor lines, presumably reflecting differences in drug uptake as a result of varying expression in drug transporters, or variability in binding affinity due to mutations at the catalytic site. We then converted these values into a potential measure of drug binding efficacy by taking the ratio of drug binding levels between the test and the saturating doses (Fig. 3.5b). These results suggest the potential for a future "treatment index," where patients with high drug binding efficacy would receive lower therapeutic doses, while patients with low drug binding efficacy would require higher doses, or be candidates to receive alternative drugs. In the future we plan to combine this assay with a previously developed assay[136] using two-step antibody-nanoparticle labeling to detect target expression. In this way, we will be able to discriminate low signals as a result of diminished drug binding as opposed to decreased expression of the target protein.

The described approach lays the groundwork for further advances. The sensitivity of the assay could be further enhanced by adopting two step bioorthogonal systems. In the first step, the drug could compete with a drug-*trans*-cyclooctene (TCO) conjugate of similar size with reduced steric constraints. In a second step, a Tetrazine (Tz)-NP could "click" with the drug-TCO to reveal target binding. Such two step systems have been shown to have a dramatic improvement in sensitivity over direct conjugates;[110] moreover, PARPi-TCO molecules have already been described.[124] A second consideration is the fact that current read-out happens as an average in several hundred to

thousand of cells. In the future, we hope to combine the assay with newer generations of ultra-high sensitivity DMR and other magnetic technologies that would allow for single cell sensing of drug binding.[116] This sensitivity could potentially allow for early identification of rare drug resistant clones where the target protein contains mutations in the drug binding pocket or the resistant cells display an increase in drug efflux pumps. For example, we show that we can discriminate differences in drug binding in HT1080 cell lines that overexpress MDR (a drug effluxor protein) as compared to normal HT1080 (Figure 3.6).

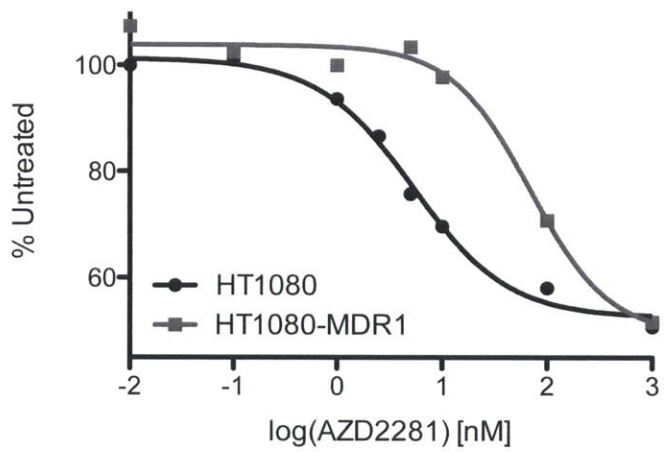

Figure 3.6. PARPi Nanosensor Curves Show Drug Efflux. Competitive nanoparticle drug binding showed differences in binding affinities between a drug-sensitive HT1080 cell line [IC_{50} = 5.3 nM; r^2 = 0.9923], and its drug-resistant counterpart transfected with MDR1 [IC_{50} = 68.6 nM; r^2 = 0.9983]. Olaparib, or AZD-2281 is a known substrate of MDR1, a drug extruding protein. Moreover, MDR1 upregulation is a known resistance mechanism in response to Olaparib as well as standard-of-care taxol chemotherapeutics.

Finally, in the current work we have focused solely on drug target binding, but not on therapeutic efficacy. It would thus be of interest to combine the current assay with molecular profiling of several protein biomarkers to measure drug response. For example, one could assay cellular phenotypes to drug response such as apoptosis induction *via* measurements of cleaved caspases and cleaved

PARP or PI3K/MAP kinase inhibition using measurements of key signaling pathway proteins such as phospho-s6rp.[127]

3.2.5 Conclusion

The described method could serve as a broader platform generalizeable to other drugs and their targets. The main challenges in adapting the assay to other drug or cellular systems are 1) the ability to modify the drug while retaining target specificity, tight binding, and stability in aqueous buffers and 2) optimization of assay conditions to ensure optimal nanoparticle binding for each target system. For some proteins, steric hinderance from the nanoparticles may be an issue for targets proteins with small binding pockets. This could be overcome by implementing two-step labeling with click chemistries. Recently, we have shown this to be possible for a variety of targets, e.g. Taxol,[137] PARP1[123,138,139] or PLK1 inhibitors.[140] Each target-inhibitor system would also require optimization of drug and nanoparticle concentrations, incubation times and cell permeabilization levels to ensure that nanoparticle binding is not assay-limited. Notably, an inherent benefit of the assay is that just one drug conjugate is required to survey several inhibitors of a particular target (Fig. 3.4). Thus, there is flexibility during assay development to select a drug that is both optimal for the target system, yet easy to work with. In the future, we believe the assay can be extended beyond cancer cells, and used in other organisms such as bacteria to assay antibiotic resistance.

The ability to provide such data in biologically relevant samples could be of considerable clinical interest to make rational treatment decisions, optimize doses in a given patient and understand population heterogeneities of drug responses. The method could also serve to quantitate the effective drug target resident time in readily accessible samples such as peripheral blood. In sum, we designed and developed a paradigm using small molecule nanoparticle conjugates that have the potential to address several clinical limitations and to impact patient treatment.

3.2.6 Personal Contribution to Work

The author of this thesis led a group of researchers in planning, performing and interpreting experiments.

3.3 Materials and Methods

3.3.1 Materials

The cell lines HT29, MDA-MB-231, MDA-MB-436, HeLa, HEK293, UCI-101, A2780, and OVCAR429 were all obtained from ATCC and cultured in RPMI (MDA-MBA-231, MDA-MB-436, OVCAR429, A2780, UCI-101) or DMEM (HT29, HeLa, HEK293) with 10% fetal bovine serum, 1% L-glutamine and 1% penicillin. The small molecule drug AZD-2281 modified with the NHS-ester was synthesized in-house. Free AZD2281 (Selleck), BSI-201 (ChemieTek), AG04699 (ChemieTek) and 3-aminobenzamide (Sigma) were all commercially purchased for use in competition assays. Until otherwise noted, all reagents were purchased from Sigma-Aldrich (St. Louis, MO) and used without further purification. Cyclohexylcarbodiimide polystyrene resin was purchased from EMD biosciences (Gibbstown, NJ). 4-[[4-Fluoro-3-(4-(5-oxopentanamide)piperazine-1-carbonyl)phenyl]methyl]-2H-phthalazin-1-one was synthesized according to published literature procedures.[124] Proton nuclear magnetic resonance (^{1}H NMR) spectra were recorded on a Varian AS-400 (400 MHz) spectrometer. Chemical shifts for protons are reported in parts per million (ppm) and are referenced against the dimethylsulfoxide lock signal (^{1}H, 2.50 ppm). Data are reported as follows: chemical shift, multiplicity (s = singlet, d = doublet, t = triplet, m = multiplet), integration and coupling constants. LC-ESI-MS analysis and HPLC-purifications were performed on a Waters (Milford, MA) LC-MS system. For LC-ESI-MS analyses, a Waters XTerra® C18 5 μm column was used. For preparative runs, an Atlantis® Prep T3 OBD™ 5 μM or a XTerra® Prep MS C18 OBD™ 5 μM column was used. High-resolution electrospray ionization (ESI) mass spectra were obtained on

a Bruker Daltonics APEXIV 4.7 Tesla Fourier Transform mass spectrometer (FT-ICR-MS) in the Department of Chemistry Instrumentation Facility at the Massachusetts Institute of Technology.

3.3.2 Synthesis of AZD-NHS

Cyclohexylcarbodiimide polystyrene resin (74 mg, 2.3 mmol/g) was added to a solution of 4-[[4-Fluoro-3-(4-(5-oxopentanamide)piperazine-1-carbonyl)phenyl]methyl]-2H-phthalazin-1-one (**3**) (20 mg, 0.042 mmol) and N-hydroxysuccinimide (20 mg, 0.174 mmol) in dichloromethane (1.5 mL) and the resulting mixture stirred gently at room temperature over night. Subsequently, the reaction mixture was filtered and volatiles removed in vacuo. The crude material was purified via silica chromatography (acetonitrile/ethyl acetate = 5%-100%, yielding the title compound as a clear solid (15.5 mg, 0.027 mmol, 64%). ^{1}H NMR (400 MHz, DMSO-d_6) δ = 12.59 (s, 1H), 8.26 (d, $^{3}J_{HH}$ = 7.7, 1H), 7.96 (d, $^{3}J_{HH}$ = 7.9, 1H), 7.89 (t, $^{3}J_{HH}$ = 7.2, 1H), 7.83 (t, $^{3}J_{HH}$ = 7.4, 1H), 7.47-7.41 (m, 1H), 7.39-7.34 (m, 1H), 7.24 (t, $^{3}J_{HH}$ = 9.0, 1H), 4.33 (s, 2H), 3.67-3.12 (m, 8H), 2.81 (m, 4H), 2.72 (t, $^{3}J_{HH}$ = 6.4, 2H), 2.50-2.40 (m, 2H), 1.89-1.81 (m, 2H); ^{19}F NMR (376 MHz, DMSO-d_6) δ = -119.68; LC-ESI-MS(-) *m/z* = 576.2 $[M-H]^-$; LC-ESI-MS(+) *m/z* = 578.3 $[M+H]^+$; HRMS-ESI $[M-H]^+$ m/z calcd. for $[C_{29}H_{27}FN_5O_7]^-$ 576.1900, found 576.1888.

3.3.3 Nanoparticle Conjugations and Characterization

Cross-linked iron oxide (CLIO) nanoparticles were synthesized and tagged with with an amine reactive cyanine dye (VivoTag 580xL, VT680xL, Perkin Elmer) as previously described [110]. Magnetofluorescent nanoparticles were reacted with 370 equivalents of AZD2281-NHS in PBS with 5% dimethylformamide (DMF) for 4h at room temperature. Excess AZD2281-NHS was removed using 100kD ultracentrifugation filtration units (Amicon) washed three times with PBS at 2000 rcf for 10 minutes and subsequently passed through a Sephadex G50 column.

Nanoparticle concentration was determined by measuring iron content through absorbance at a characteristic wavelength of 400nm as previously established.[141,142] Drug loading was determined by measuring the change in absorbance between the conjugated and unconjugated nanoparticle at 275nm. This change in absorbance was normalized by the amount of CLIO per sample, as calculated previously using iron concentration (UV absorbance at 400nm).[141] Molecules of AZD-2281 per nanoparticle were determined using a standard curve for the unreacted AZD-2281-NHS-ester. Drug inhibitory activity was confirmed by testing the ability of AZD2281-NP to inhibit PARP activity using an standard, *in-vitro* plate assay (Trevigen). Nanoparticle size was measured using dynamic light scattering (Malvern).

3.3.4 Cell Labeling

Cells were grown in culture for 3 days up to 90% confluency before collection with 0.05% Trypsin/ 0.53 mM EDTA, and washed once with Stain Buffer, SB+ (PBS + 2% FBS + 1% BSA). Cells were then fixed with a 1:1 mixture of PBS with a formaldehyde based fix buffer (FBI, BD Biosciences) for 20 minutes at room temperature and permeabilized by washing twice with a saponin containing buffer with 1% BSA (PW+) (Perm/Wash Buffer, BD Biosciences). Each sample (250,000 cells/ sample) was then labeled with 15 μg Fe/ml of nanoparticle (PARPi-NP, or Control-NP) in PW+, and incubated at room temperature protected from light on a rocker for 20 minutes. Excess nanoparticle was removed with two washes of PW+ before a final wash and resuspension in PBS (or Stain Buffer).

For the competition assay, HEK293 cells were treated with varying concentrations from 0 to 100μM of various PARP inhibitors. Solutions were made up in PW+. After a 20 minute incubation at room temperature with the free inhibitor, the targeted PARPi-NP or Control NP were added to the same mix for a total concentration of 15 μg Fe/ml and incubated for an additional 20 minutes

before washing and continuing with labeling as described above. Data shown represents at least biological duplicates and experiments were repeated at least three times. All data was fitted using Prism 5.0 (GraphPad, La Jolla, CA).

3.3.5. Immunoblotting

Lysates were collected from cells at 90% confluency by washing with cold PBS on ice and scraping with Ripa buffer containing a protease inhibitor cocktail. Samples were syringed 3 to 5 times and sonicated for 30 seconds before being spun down at 10,000 rpm for 15 minutes to collect the supernatant. Samples were made up with 4x Laemlli buffer with DTT and boiled for 10 minutes. Ten µg of total protein was loaded on NuPAGE 4-12% gradient Bis-Tris gels (Invitrogen) with MOPS running buffer and transferred to PVDF membrane using an iBlot Gel Transfer Device (Invitrogen). Blots were blocked with 5% dried milk in TBST (TBS with 0.1% Tween-20) and probed with primary monoclonal antibodies at the appropriate dilutions (PARP1, Santa Cruz Biotechnology sc7150, 1:250; PARP2, Abcam ab93416, 1:250, Beta-tubulin, Abcam ab7287, 1:100). Relative expression for each blot quantified using ImageJ (NIH).To ensure consistency in PARP expression, cell lysates were collected within four passages of the PARPi-NP detection. Data shown is representative of biological triplicate and is displayed as mean ± standard error.

3.3.6 Flow Cytometry

To determine target binding, the amount of nanoparticle present was quantified from VT680 fluorescence with an LSRII flow cytometer (Becton Dickinson) and the geometric mean of fluorescence intensity was determined using FlowJo software. All measurements were performed in biological triplicate and signals were normalized by the Control NP sample ($S_{PARPi\text{-}NP}/S_{Control\text{-}NP}$). Data are shown as mean ± standard error.

3.3.7 Microscopy

Cells were labeled with nanoparticle as described above, and then incubated for 1 hour at room temperature with a PARP1 antibody (Santa Cruz Biotechnology sc8007) at a dilution of 1:50 in PW +. Cells were washed once with PW+ and then incubated with secondary antibody at 2ug/ml for half an hour on ice. Cells were washed two more times with PW+ before resuspension in PBS. A minimal volume (100μL) of sample containing approximately 10,000 cells was transferred to a 96 well plate and imaged . Images were acquired at 40x with DeltaVision screening system (Applied Precision Instruments) and analyzed using FIJI software (version 1.45).

3.3.8 DMR

Magnetic detection measurements were conducted as described previously[133] with 10,000 cells using the miniaturized nuclear magnetic resonance device, DMR,[73] for target expression and competitive binding experiments. Detection in whole blood studies were performed with detection of as few as 1,500 cells. Signals were calculated by converting T_2 measurements to R_2 and compared the change in R_2 from the baseline PBS sample to the labeled PARPi-NP ($S_{PARPi\text{-}NP}$) or Control-NP ($S_{Control\text{-}NP}$). Signals from the PARPi-NP were normalized by dividing by the signal from the Control-NP ($S_{PARPi\text{-}NP}/S_{Control\text{-}NP}$). Data shown is in biological duplicate and is represented as means $\pm$ standard error.

3.3.9 Whole Blood Processing

Selected cell lines (A2780, UCI-101, OVCAR429 and MDA-MB-231) were spiked into human whole blood samples (200,000 cells in 1.5mL). Samples were then either left untreated, or incubated with AZD-2281 at 155 nM and 1.5μM for 30 minutes at room temperature. Following drug incubation, red blood cells were partially lysed with an RBC lysis agent (Qiagen), the sample was washed with SB+. The sample was then divided into two samples and probed either with PARPi-NP or Control-NP at 5 μg Fe/mL in 0.2x PW+ for 60 minutes. Samples were washed twice with 0.2x PW+ before resuspension in SB+ (or PBS). CD45 Negative selection was performed by

using CD45 magnetic beads and LS columns (Miltenyi Biotec). Signals from CD45+ cell samples were then measured by flow cytometry or DMR.

I Chapter 4 I Proteomic Profiling to Monitor and Predict Treatment Response in Patients

4.1 Introduction

Variability of protein levels across cancer-driving networks can provide a snapshot of the cell's phenotype. Proteins function as the cell's machinery to directly regulate cell fate, survival and genomic integrity. Understanding protein expression and fluctuation could directly affect knowledge about drug pharmacodynamics and the extent to which drugs engage their targets, trigger alternative molecular pathways, and induce tumor cell death or resistance.[154] Though we annotate proteins into discrete, canonical pathways, in reality they interact and overlap in a complex network. Consequently, protein functions can differ on a case by case basis, making it difficult to a priori select good biomarkers in clinical trials for varying treatments.

Integrating large-scale proteomic measurements across relevant cancer pathways into clinical trials would allow us to algorithmically determine predictive biomarkers. However, there are limited tools for proteomic analysis in the clinical setting; mass spectrometry remains technically challenging and extremely expensive, while scant sample material precludes broader analysis by immunohistochemistry. [44,143] We sought to develop a method that circumvents the limited throughput, capacity and loss of material associated with the above methods. We initially entertained emerging approaches such as mass cytometry[49] and multicolor spectral deconvolution,[144] but they did not have the required multiplexing capability or sample yield for clinical samples harvested by fine needle aspirates (FNA). DNA barcoding on antibodies had the potential to allow large-scale multiplexed read out on the order of hundreds of markers with high sensitivity. The majority of DNA barcoding technologies have previously been used in conjunction with qPCR to quantify readouts. However, large-scale multiplexing with qPCR requires individual primer design and hands-on processing for each marker. Thus, multiplexing with over 50 markers on single cells has not been achieved with any of the current DNA barcoding techniques.

We used a photocleavable linker to conjugate DNA to antibodies and selected the Nanostring platform to attain multiplexing of nearly 100 markers on single cells. This platform offered unique advantages over qPCR and other methods including i) multiplexed quantification on limited sample ii) femtomolar sensitivity iii) quantitative and reproducible results without amplification and iii) direct readout from cell lysate.[75] This would allow us to achieve i) simultaneous detection of hundreds of markers ii) theoretical sensitivity of detecting a single cell iii) quantification without amplification bias and iv) increased sample preservation by removing DNA isolation and wash steps. Here, we show that our approach has high correlation to gold standard methods such as flow cytometry and immunofluorescence. We then demonstrate that this profiling method can be used to discriminate pathway changes across different type of treatments. Finally we establish translational potential for patient monitoring by examining cancer patients on trial for a PI3K inhibitor where we find profiles can be predictive of treatment response.

4.2 Results and Discussion

4.2.1 Method Development and Validation

In order to perform proteomic profiling, we adapted standard flow cytometry antibody staining methods and combined them with the commerical Nanostring platform for genetic readouts. A cocktail of chimeric DNA-barcoded antibodies were mixed with permeabilized cells to allow for both extracellular and intracellular protein detection. After staining, DNA was released through photocleavage and lysis. Finally, DNA barcodes were read out and quantified using the Nanostring platform (Fig 4.1). Negative IgG/housekeeping antibody controls, internal DNA controls, and measurement of relative DNA per antibody were then used to extract expression profiles. Any markers that were not above IgG control signals were excluded. Thus, depending on antibody binding or expression level, some markers are not displayed in subsequent figures.

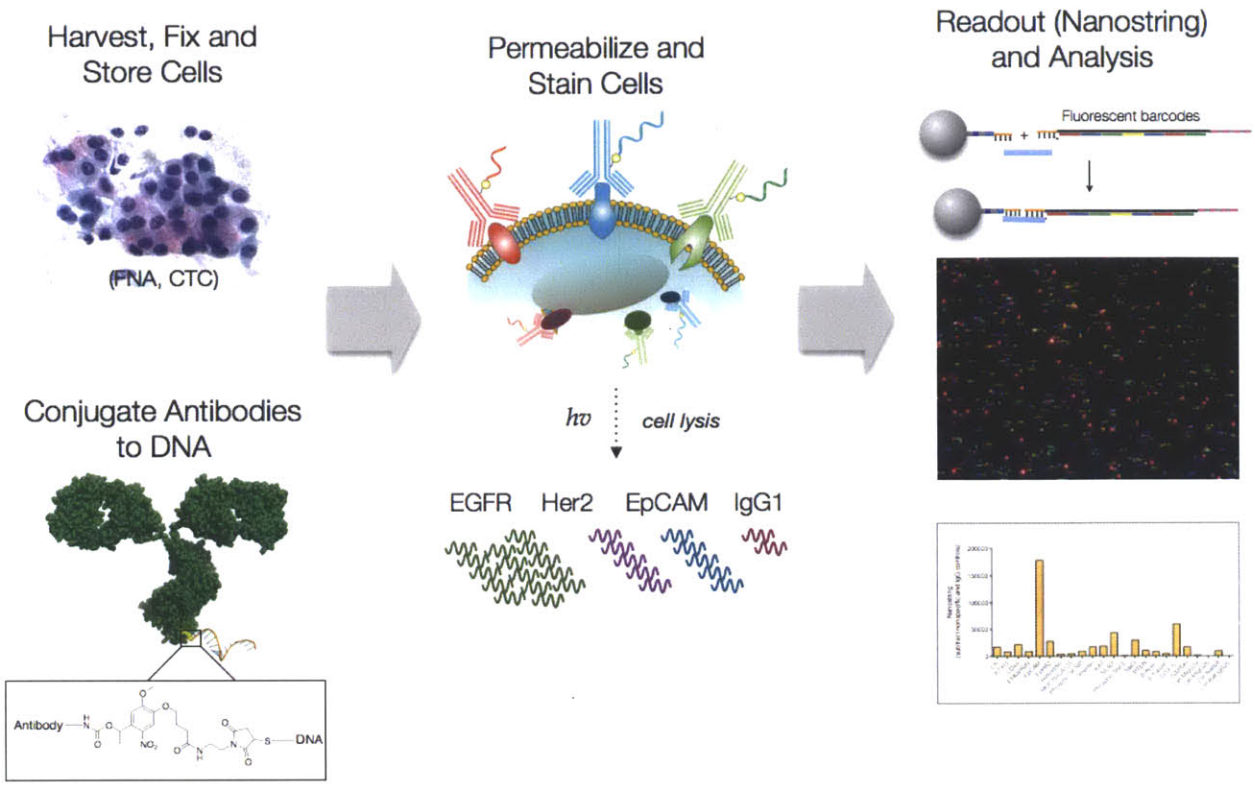

Figure 4.1 Schematic of DNA barcoded proteomic profiling. Cells are harvested from cancer patients by fine needle aspirate. Antibody conjugates contain a photocleavable linker to allow DNA release after exposure to specific wavelengths of light. Cells of interest are then "stained" with a cocktail of DNA barcode-conjugated antibodies. DNA barcodes are released from lysed cells and quantified with the Nanostring fluorescent DNA barcoding platform where probes are hybridized and imaged via a CCD camera. Protein expression levels are derived by subtracting non-specific binding from control IgGs and normalizing according to DNA per antibody and housekeeping genes.

We validated our approach by utilizing gold standard methods such as flow cytometry and show that protein expression measured from unconjugated antibodies correlate highly to chimeric conjugates in two different cell lines (Fig. 4.2). We then compare profiles of two ovarian cancer cell lines and a control benign ovarian epithelial cell line derived from our method compared to standard flow cytometry measurements and find high correlations between the two methods (Fig 4.3).

	SKOV3	ES2
Pearson R	0.93	0.85
Linear (r^2)	0.92	0.72
p value	<.0001	<.0001

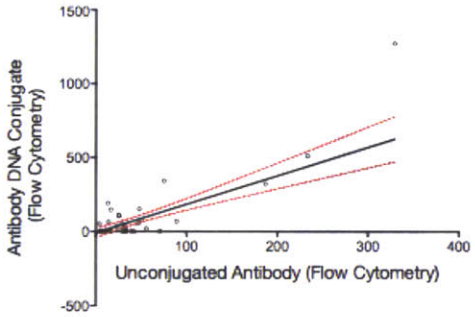

Figure 4.2. Validation of Conjugated Antibodies. DNA-conjugated antibodies were compared to native antibodies by performing immunocytochemistry in parallel. Results on flow cytometry showed similar results with linear relationships and high Pearson R values in two cell lines (p<.0001).

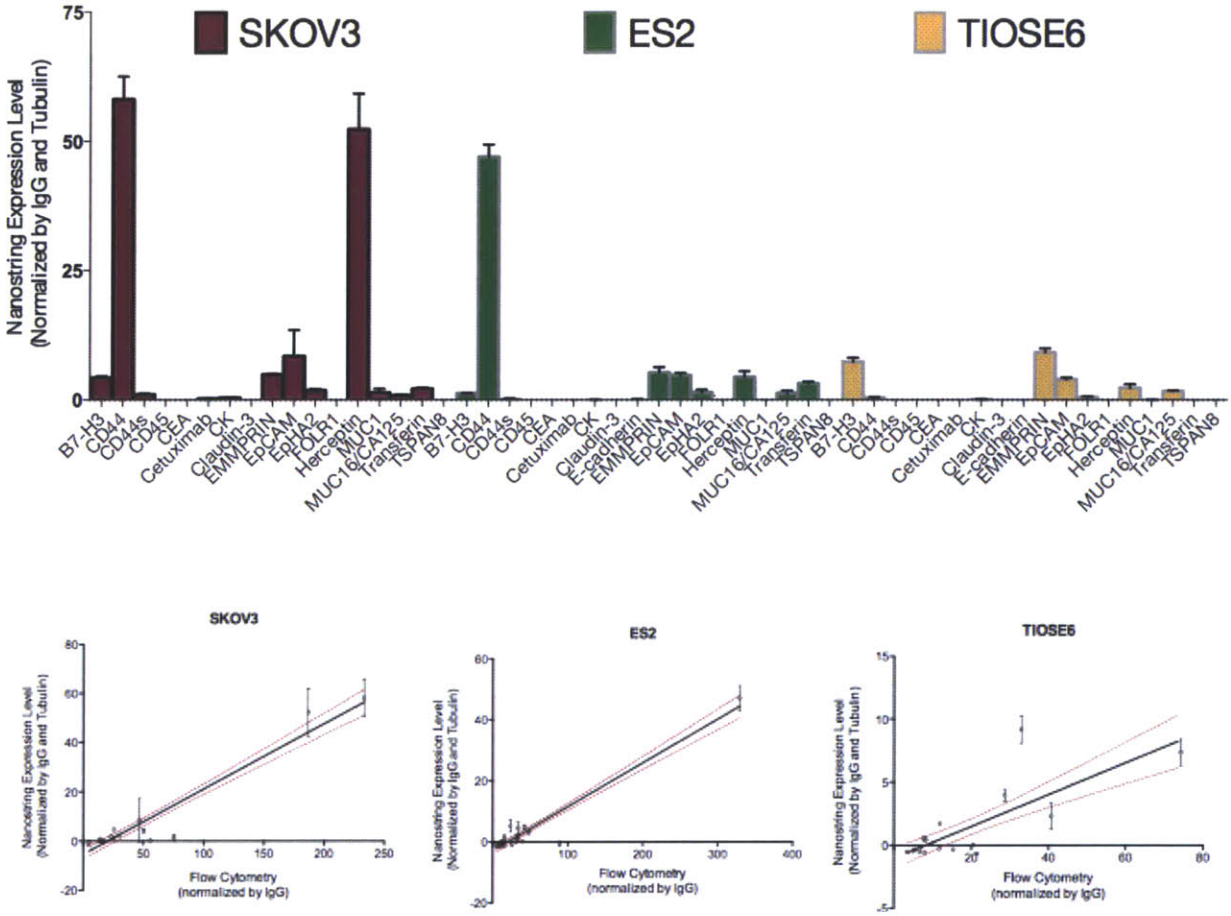

Figure 4.3. Validation of DNA barcoded Proteomic Expression Profiling. (a) Multiple cancer antigens and markers were profiled on two ovarian cancer cell lines (SKOV3 and ES2) and a benign ovarian epithelial cell line (TIOSE6). As expected, cancer antigens were high on the malignant cell lines (CD44 for SKOV3 and ES2, and Her2 for SKOV3). In contrast, TIOSE6 showed relatively low expression for all cancer antigens tested. (b) Proteomic measurements from the DNA barcoding were consistent with flow cytometry

measurements performed on the same passage of cells, and showed a linear, high correlation for SKOV3 (Pearson R = 0.96, r^2=0.89, p<.0001), ES2 (Pearson R = 0.96, r^2=0.91, p<.0001), and TiOSE6 (Pearson R = 0.78, r^2=0.60, p<.0001). Data is shown in triplicate and errors bars are shown as +/- standard error.

All measurements were performed on DNA from the equivalent of just 100 cells. Using this methodology we were able to multiplex up to 96 antibodies (88 markers, 6 controls). Markers were selected to cover a wide range of relevant cancer pathways and also included a number of cancer biomarkers. The breakdown of markers into various categories and their profile on a triple negative breast cancer cell line is shown in technical replicate (Figure 4.4).

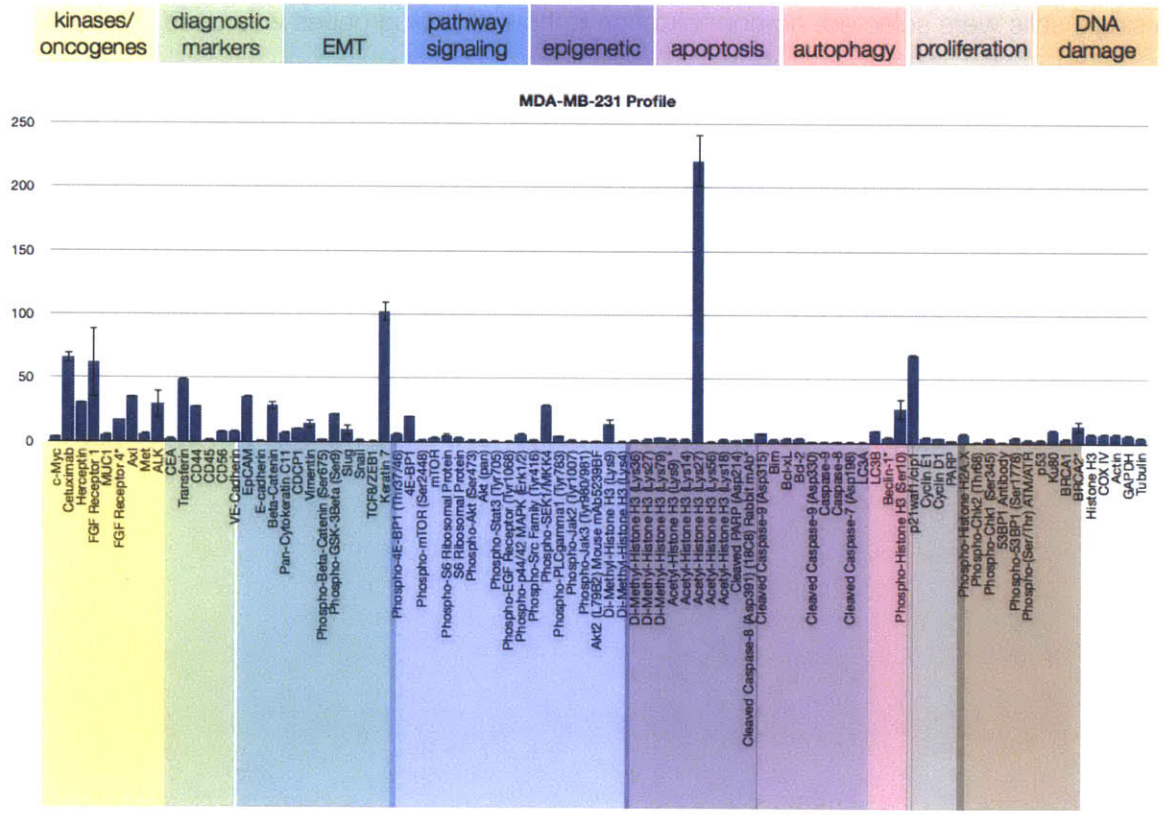

Figure 4.4. Multiplexed Profile of MDA-MB-231 in technical replicate. Representative example of 88 different DNA barcode-antibody conjugates spanning cancer-relevant pathways are profiled in triplicate

on the MDA-MB-231 triple negative breast cancer cell line. DNA signal is converted to protein binding by normalizing according to relative DNA per antibody levels. Non-specific binding from expression of six control IgGs is subtracted and expression was normalized by housekeeping genes. Housekeeping genes (Cox IV, Histone H3, Tubulin, Actin and GAPDH) are shown at the far right and have consistent expression. Data is shown in technical triplicate and errors bars are shown as +/- standard error.

4.2.2 Sensitivity and Single Cell Profiling

We tested the sensitivity of our method by measuring dilutions of DNA input to bulk measurements (DNA barcodes from 500,000 A431 cells). Dilutions down to 5 cells gave extremely significant, linear and high correlation values. We then examined single cell measurements by isolating and selecting single cells from an antibody-stained population using a micromanipulator. Single cells then underwent similar processing and analysis as described for the bulk measurements. However, since single cells were selected, no normalization to housekeeping genes was used. The profiles for single cells were compared to bulk measurements in cell culture. Significant and high correlation values were found between the single cells and bulk. High concordance could also be seen through Bland-Altman plots which showed the difference between single cell measurements to the bulk measurements (Figure 4.5).

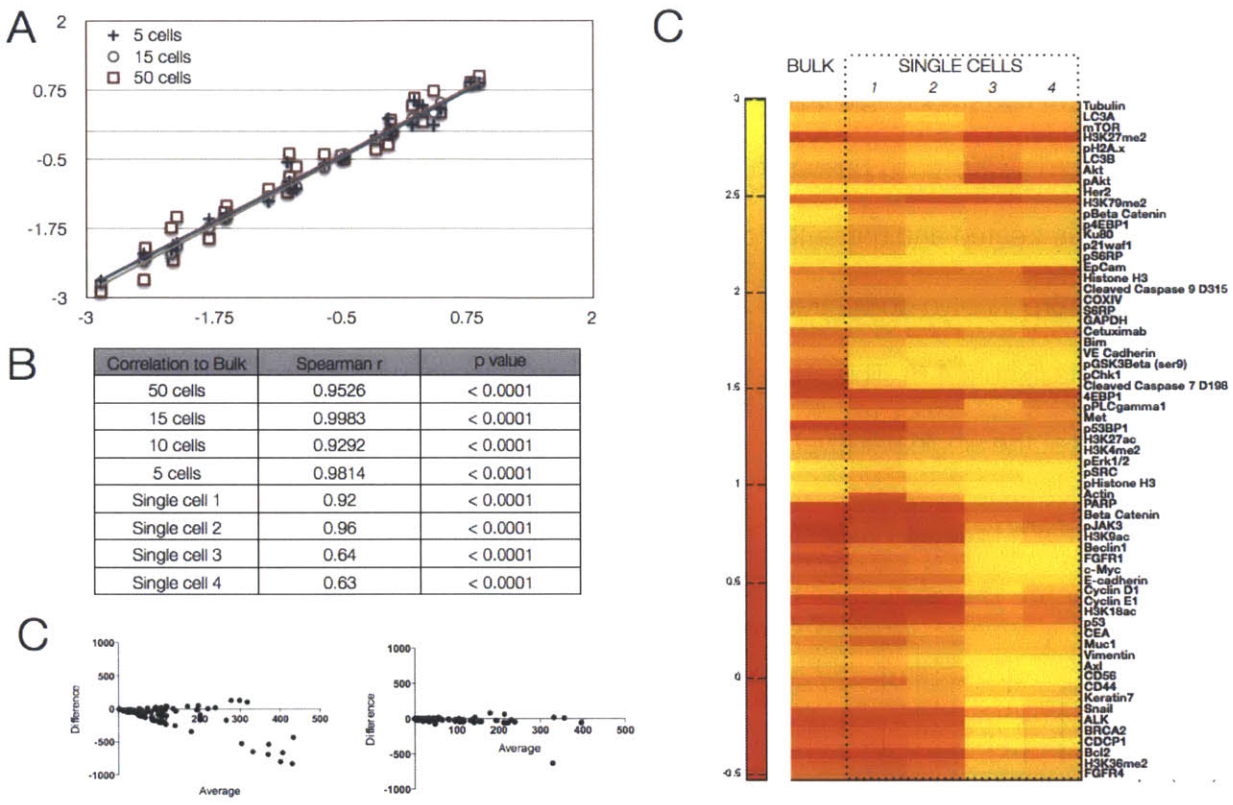

Correlation to Bulk	Spearman r	p value
50 cells	0.9526	< 0.0001
15 cells	0.9983	< 0.0001
10 cells	0.9292	< 0.0001
5 cells	0.9814	< 0.0001
Single cell 1	0.92	< 0.0001
Single cell 2	0.96	< 0.0001
Single cell 3	0.64	< 0.0001
Single cell 4	0.63	< 0.0001

Figure 4.5. Detection Sensitivity. (A) 500,000 cells from the epidermoid carcinoma cell line, A431, were lysed and processed as shown in Fig. 4.1. Dilutions corresponding to 5, 15, and 50 cells were then compared to the bulk measurement, showing good correlation at low cell numbers (Spearman R = 0.98). (B) Correlation values for analyzing small cell numbers as well as single cell analysis selected by micromanipulation. (C) Bland-Altman plots of two single cells show high concordance between markers whether measured in bulk or at the single cell level. D) Protein expression profiles (log 2 expression values) of four single cells are compared to profiles of the bulk sample. While all cells showed similar relative protein expression, single cells 1 and 2 showed nearly identical profiles to bulk measurements, whereas single cells 3 and 4 showed lower overall protein levels. Correlations were highly significant when comparing all single cells to bulk measurements ($p<.0001$). The heat map is shown with row normalization across each marker on a log scale.

The variability in single cell measurements is a combined result of technical and biological variation. Since it is impossible to achieve technical replicates on a single cell, we instead show that single

cell profiling actually produces biologically relevant results by using a positive control experimental study where we compare single cells from A431 cells treated with EGFR inhibitor (gefitinib) treated to untreated cells. Clustering based on correlation values from the proteomic profiling naturally segregated the treated and untreated populations; moreover, significant differential markers such as phospho-s6rp (known downstream target of gefitinib) were identified from these single cell measurements (Figure 4.6). This showed that biologically relevant variation could indeed be discriminated at the single cell level.

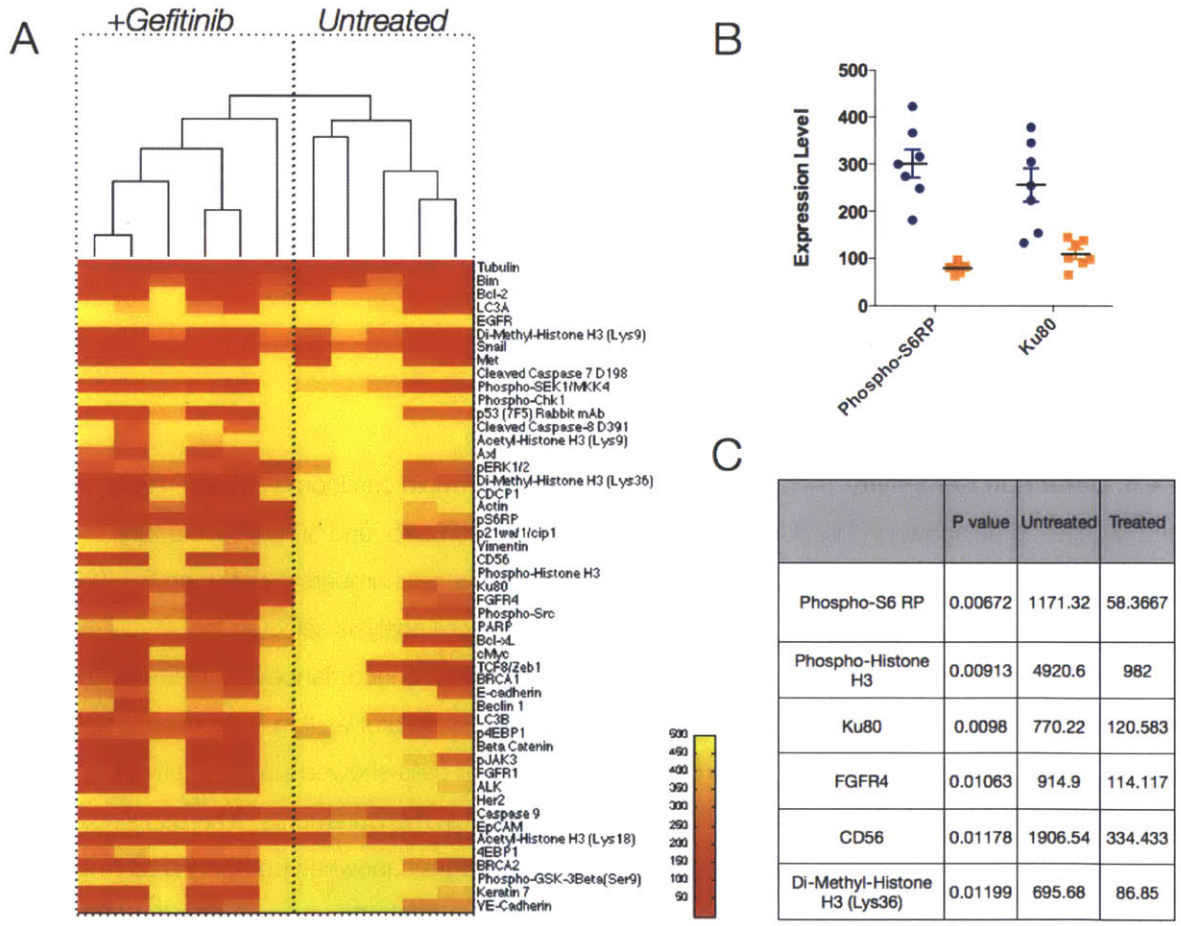

	P value	Untreated	Treated
Phospho-S6 RP	0.00672	1171.32	58.3667
Phospho-Histone H3	0.00913	4920.6	982
Ku80	0.0098	770.22	120.583
FGFR4	0.01063	914.9	114.117
CD56	0.01178	1906.54	334.433
Di-Methyl-Histone H3 (Lys36)	0.01199	695.68	86.85

Figure 4.6. Validating Single Cell Measurements. (A) We examined single cell measurements in A431 cell lines that were untreated and treated with the EGFR inhibitor gefitinib. A431 cell lines overexpress EGFR and are highly sensitive to gefitinib (IC_{50} = 100nM) as evidenced by widespread pathway inhibition (marked in red) in these cells. Treated and untreated cells segregated into two clusters based on a correlation metric (MatLab). The heat map scale is indicative of expression values across each of the markers accounting for

non-specific IgG binding. (B) Expected markers such as phospho-s6rp and Ku80 show significant changes between treated (yellow) and untreated (blue) cell lines. Many other markers also showed significant treated to untreated changes as shown in (C). These markers included surface receptors (FGFR4, CD56) and the proliferation marker phospho-Histone H3.

4.2.3 In Vitro Profiling of Cells and Treatments

The value of our methodology stems not only from its scale but also careful selection of markers. In order to study treatment response, we carefully selected markers that were implicated in notable cancer pathways, many of which are relevant to molecularly targeted drugs and chemotherapeutics.

We performed a number of in vitro screens across many types of treatments, doses and cell lines to demonstrate that the method could indeed identify both established and novel biological changes. Furthermore, we performed independent experiments to verify that we get similar marker changes using a different technique (immunofluorescence) with the same cell lines and treatment conditions.

We first performed a dose response study of taxol (Paclitaxel) on a HT1080 fibrosarcoma cell line. The results for all the markers across multiple doses are shown in Figure 4.7. Significant marker changes were determined by pairwise comparisons. One of the significant markers was tubulin, the primary target of taxol for microtubule inhibiton (Table 4.1). We also gleaned that several markers showed dose response curves (CDCP1, pCycD, CyclinE1, FGF4, BRCA2, and pERK1/2). These marker changes were consistent with an independent screen performed by immunofluorescence (Fig 4.8). In sum these experiments showed marker changes that were confirmed by results from other established methods. Additionally, we pulled out the expected dose-responses and primary drug targets for taxol. Interestingly the 350nM dose had less of a response than 7nM or 700nM.

This could be due to biological variability, or specific dose-dependent responses that have previously been found in the literature.[155,156]

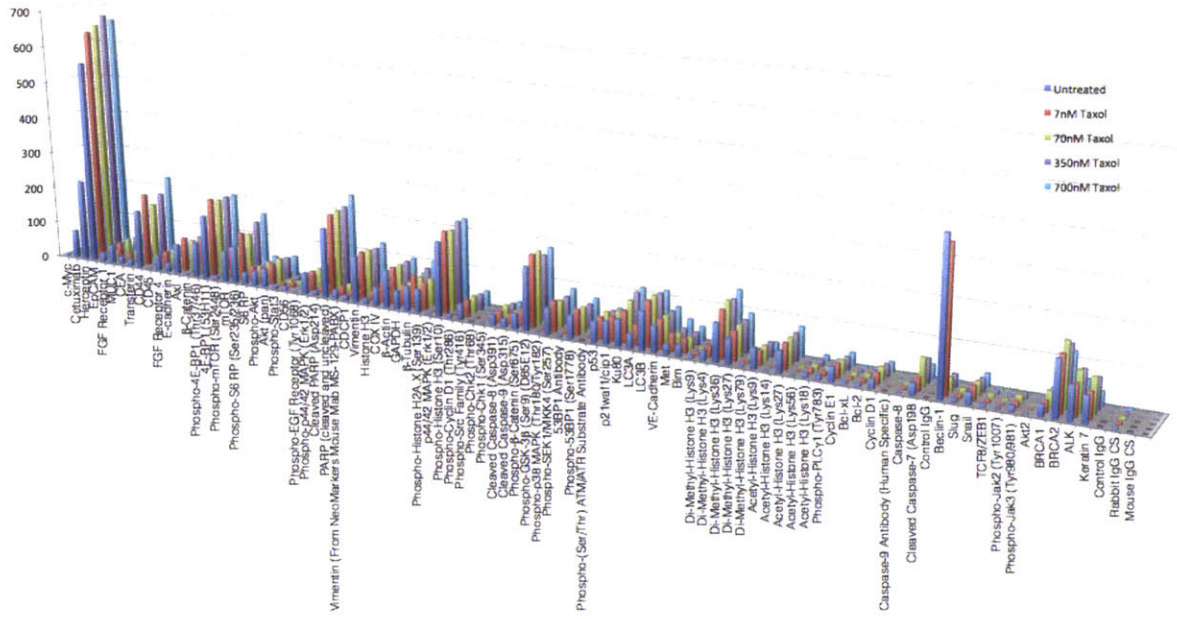

Figure 4.7. HT1080 Multiplexed Dose Response to Taxol in HT1080 Cells. (A) Multiple doses of taxol (0, 7, 70, 350 and 700nM) were given to HT1080 fibrosarcoma cell lines for 24 hours. Profiles from each dose are shown from biological duplicate. Control antibodies are shown at the end of the graph and have low expression levels.

vs 7nM	*p value*	vs 70nM	*p value*	vs 350nM	*p value*	vs 700nM	*p value*
none	none	Cyclin E1 (HE12)	0.00254017	CDCP1 Antibody	0.00107952	CDCP1 Antibody	0.00058121
		Phospho-Jak3	0.0032228	53BP1 Antibody	0.00168038	Transferin	0.00080497
		CDCP1 Antibody	0.0045608	BRCA2	0.00449409	β-Actin (13E5) Rabbit	0.00534819
		ALK (D5F3) XP®	0.00725414	Cyclin E1	0.00597256	β-Tubulin (9F3) Rabbit	0.0099721
		BRCA2	0.00932165			MUC1	0.0108515
		β-Actin (13E5) Rabbit	0.0103799			Phospho-Jak3	0.0120797
		Phospho-53BP1	0.0119901			Phospho-53BP1	0.0143511
		Phospho-p44/42	0.0174366			Histone H3 (D1H2)	0.0167682
		Phospho-Jak2	0.0186321			Phospho-p44/42	0.0194615
		c-Myc (D84C12) XP®	0.0199422			BRCA2	0.0201895
		GAPDH (14C10)	0.0201203			p21waf1/cip1	0.020681
		FGF Receptor 4	0.0214794			GAPDH (14C10)	0.022213
		CD56	0.0230159			Cyclin E1 (HE12)	0.0231627
		Di-Methyl-Histone H3	0.0240667			FGF Receptor 4	0.0236512
		Ku80 (C48E7) Rabbit	0.0272129			Phospho-Jak2	0.0257955
						COX IV (3E11) Rabbit	0.0287779
						4E-BP1 (53H11)	0.0318927
						Phospho-Akt (Ser473)	0.0348263
						Axl (C89E7) Rabbit	0.0363095
						VE-Cadherin (D87F2)	0.0406075
						Cetuximab	0.0431182
						E-cadherin	0.0442288
						Vimentin	0.0458849

Table 4.1. Significant Taxol Treatment Markers in HT1080 Cells. Significant markers are shown by performing a pairwise t-test (FDR = 0.2). As expected, no significant changes were evident with low doses of drug, while many profiling changes occurred at a high dose. Notable markers include Tubulin (primary target of taxol). Experiments were performed in biological duplicate.

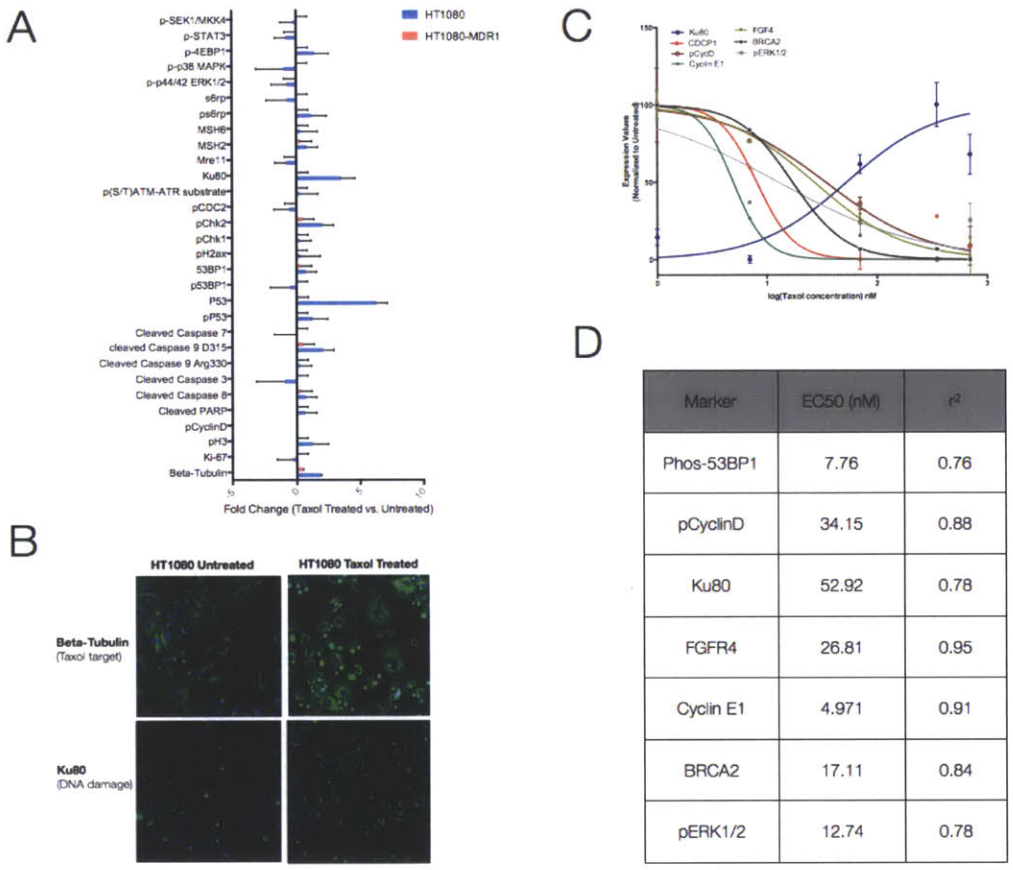

Marker	EC50 (nM)	r^2
Phos-53BP1	7.76	0.76
pCyclinD	34.15	0.88
Ku80	52.92	0.78
FGFR4	26.81	0.95
Cyclin E1	4.971	0.91
BRCA2	17.11	0.84
pERK1/2	12.74	0.78

Figure 4.8. Validation of Taxol Marker Changes. (A) Marker changes from an independent immunofluorescence screen are shown (biological triplicate +/- standard error) with sample images for key markers shown (B) After taxol treatment (right column), tubulin, the primary target of taxol, shows a different cell structure architecture (more rounded, less adherent). There is also an increase in Ku80, a DNA repair protein. (C) Similar changes were identified from DNA barcoding profiles and dose response curves could be pulled out for a variety of significant markers. (D) Each of these markers had varying EC_{50} values in response to taxol.

We then showed that this marker panel was versatile and could differentiate treatments across mechanism of action. To do this we applied 5 different treatments to a triple negative breast cancer cell line (MDA-MB-436). We selected three targeted treatments: two EGFR inhibitors (Gefitinib and Cetuximab) and a PI3K/mTOR inhibitor (PKI-587) and two DNA repair/damaging agents: PARP

inhibitor (Olaparib) and an alkylating agent (Cisplatin). Drug treatments showed expected inhibition or activation across expected markers. For example, phospho-s6rp was inhibited for the targeted treatments, and Ku80, a DNA damage marker, increased as a result of DNA damaging agents. Furthermore, these markers could be clustered based on correlation values and segregated into their mechanisms of action (Fig 4.9). Interestingly, the number of significant markers determined corresponded with the cell's sensitivity to the drug (Table 4.2). Drugs that induced greater changewere indicative of the cell's heightened sensitivity to that therapy. This suggested that profile changes and clustering in patients could be predictive of treatment response.

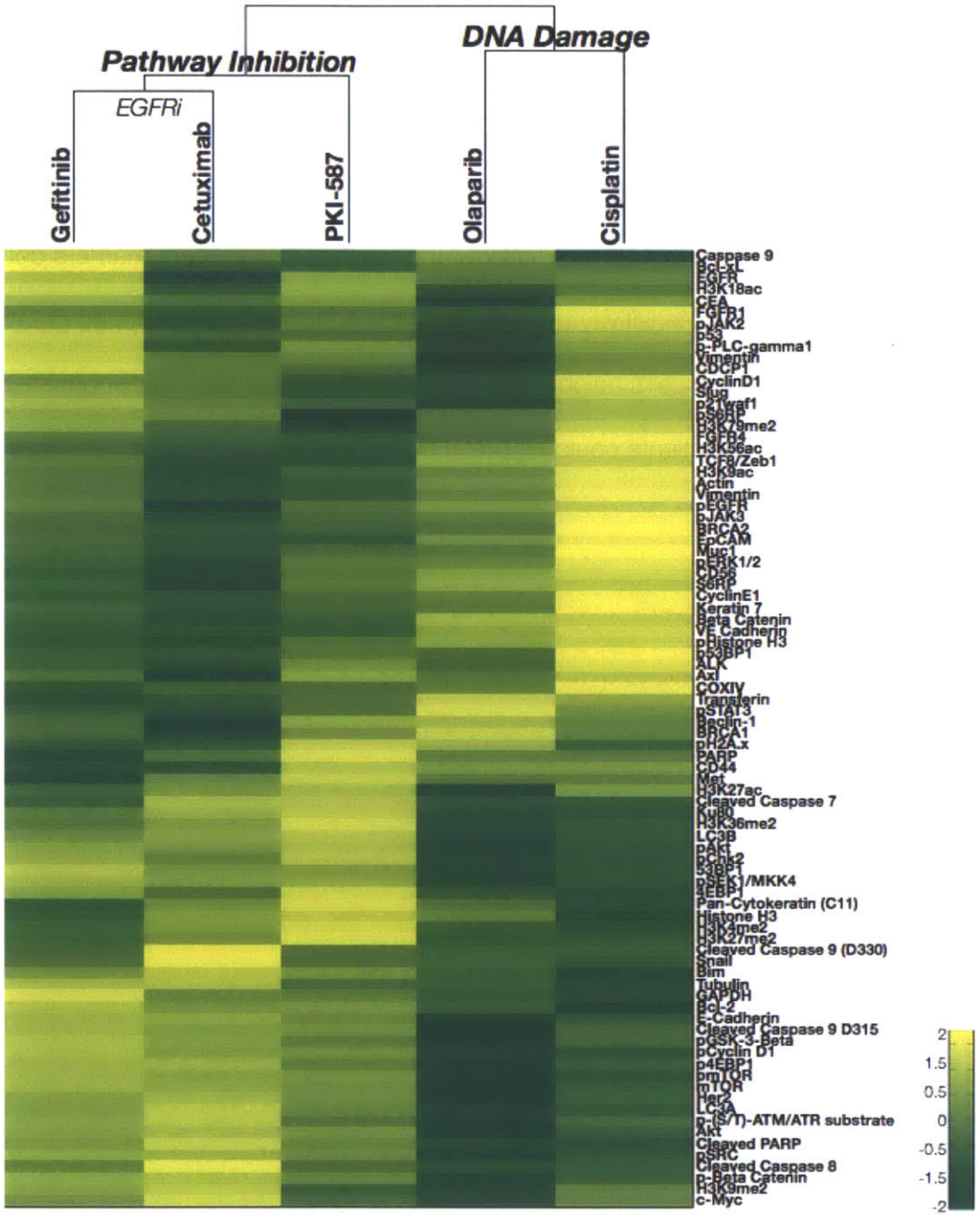

Figure 4.9. Clustering of different therapies from post-treatment profile changes. Treatment response markers for each of the groups identified inhibition of expected proteins (p-mTOR, ps6rp, pERK for targeted treatments; pH2A.X, pATM/ATR substrate for DNA damaging agents). Furthermore, correlation clustering grouped drug treatments by their mechanism of action (molecular targeted vs. DNA damaging) and their primary targets (EGFR for Gefitinib/Cetuximab vs. mTOR/PI3K for PKI-587). The heat map is normalized across row for each marker and displayed on a log scale. All measurements were performed in biological triplicate.

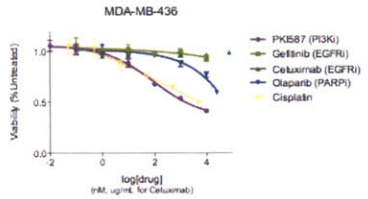

	Gefitinib
IC50 (nM)	n/a
Markers | p-value	n/a

	Cetuximab	
IC50 (ug/ml)	n/a	
Markers | p-val	Cetuximab	1.21E-03

	PKI-587	
IC50 (ug/ml)	198.3	
r²	0.83	
Markers | p-value	4E-BP1	1.45E-04
	Phospho-Histone3	4.87E-04
	PARP	6.29E-04
	Phospho-S6	6.45E-04
	Phospho-Histone2ax	9.54E-04
	Ku80	3.34E-03
	Di-Methyl- H3 (Lys36)	3.70E-03
	CD44	4.74E-03
	Di-Methyl- H3 (Lys4)	4.86E-03
	AcH3 (Lys27)	9.21E-03
	Di-Methyl H3 (Lys27)	1.17E-02

	Olaparib	
IC50 (nM)	15	
r²	0.88	
Markers | p-value	4E-BP1	1.45E-04
	Phospho-GSK-3β (Ser9)	3.30E-05
	Phospho-4E-BP1	4.92E-05
	Phospho-Akt	7.58E-05
	EGFR	1.42E-04
	mTOR	1.60E-04
	Phospho-SEK1/MKK4 (Ser257)	1.79E-04
	Cleaved Caspase-9 D315	1.87E-04
	Phospho-Src Family (Tyr416)	2.31E-04
	Phospho-S6RP	2.51E-04
	Phospho-mTOR	2.90E-04
	E-cadherin	3.78E-04
	Phos-β-Catenin	4.20E-04
	Ku80	4.28E-04
	Phospho-Chk2	6.27E-04
	Phospho-Cyclin D1	7.82E-04
	Phospho-p38 MAPK	1.86E-03
	Me2-H3-K36	2.05E-03
	Cleaved PARP	2.37E-03
	Vimentin	2.38E-03
	CEA	2.68E-03
	pSTAT3	3.15E-03
	EpCam	4.68E-03
	53BP1	5.01E-03
	ERk 1/2	5.13E-03
	VE Cadherin	5.58E-03
	pSTAT3	6.81E-03
	EpCAM	7.29E-03
	p21waf1/cip1	8.03E-03
	pH2A.X	8.07E-03
	pChk1	8.97E-03
	LC3A	9.01E-03
	p-(S/T) ATM/ATR Substrate	1.15E-02

	Cisplatin	
IC50 (nM)	1.8	
r²	0.7	
Markers | p-value	Bim	4.88E-05
	EGFR	2.81E-04
	pAKT	2.90E-04
	pmTOR	3.36E-04
	S6RP	3.54E-04
	Ku80	3.72E-04
	pCyclinD	6.04E-04
	p4EBP1	8.45E-04
	Vimentin	1.04E-03
	pH3	1.04E-03
	EpCAM	1.10E-03
	VE-cadherin	1.60E-03
	pChk2	1.90E-03
	p-SEK1/MKK4	2.20E-03
	mTOR	2.48E-03
	E-cadherin	3.02E-03
	phospho-β-Catenin	3.35E-03
	MUC1	3.51E-03
	p-(Erk1/2)	3.52E-03
	p-p38 MAPK	4.00E-03
	p-Src Family	5.96E-03
	Histone H3	6.09E-03
	Actin	8.09E-03
	Me2H3K4	9.36E-03
	Tubulin	1.33E-02
	LC3B	1.40E-02
	Cleaved Caspase 9 D315	1.61E-02
	Cleaved PARP	1.98E-02
	pChk1	2.02E-02
	p53BP1	2.56E-02
	pEGFR	2.58E-02

Table 4.2. Drug Sensitivities in MDA-MB-436 and Corresponding Significant Marker Changes. MDA-MB-436 cells are resistant to EGFR inhibitors Gefitinib and Cetuximab, and also show no significant changes in marker profiling. The significant decrease in Cetuximab during treatment serves as a control for antibody blocking or drug inhibition. In contrast, MDA-MB-436 is uniquely sensitive to PKI-587, Olaparib and Cisplatin and shows corresponding marker changes. (Pairwise-t testing, FDR = 0.2). Samples were performed in biological triplicate.

To further investigate if profile changes could be predictive of drug response, we examined profiles for Olaparib (AZD2281) and Cisplatin treatments across 4 cell lines with varying sensitivities (Fig. 4.10). Indeed we found that the sensitive breast cancer cell line MDA-MB-436 and ovarian cancer cell line A2780 showed significant marker changes across several DNA damage markers (phospho-H2A.X, phospho-Chk2, phospho-Chk2, Ku80, 53BP1) and apoptosis markers (Bim, cleaved caspases). In addition, both cell lines responded to the PARP inhibitor with changes in the

Wnt/Beta-Catenin signaling pathway. This was expected as PARP has long been known to complex with Beta-Catenin, which affects downstream Wnt signaling.[145] However, this was a pathway effect that was entirely ignored in PARP inhibitor clinical trials, and the entirety of research efforts focused on the role of PARP in DNA damage and repair.[31,121,146-149]

Resistant cell lines MDA-MB-231 and OVCAR429 did not show any significant marker changes, with one exception. OVCAR429 showed significant changes in phospho-Chk2 in response to Olaparib. This was interesting since Chk2 inhibitors have previously been shown in the literature to have a synergistic effect with PARP inhibitors, and expression of Chk2 has been predictive of Olaparib sensitivity.[150,151]

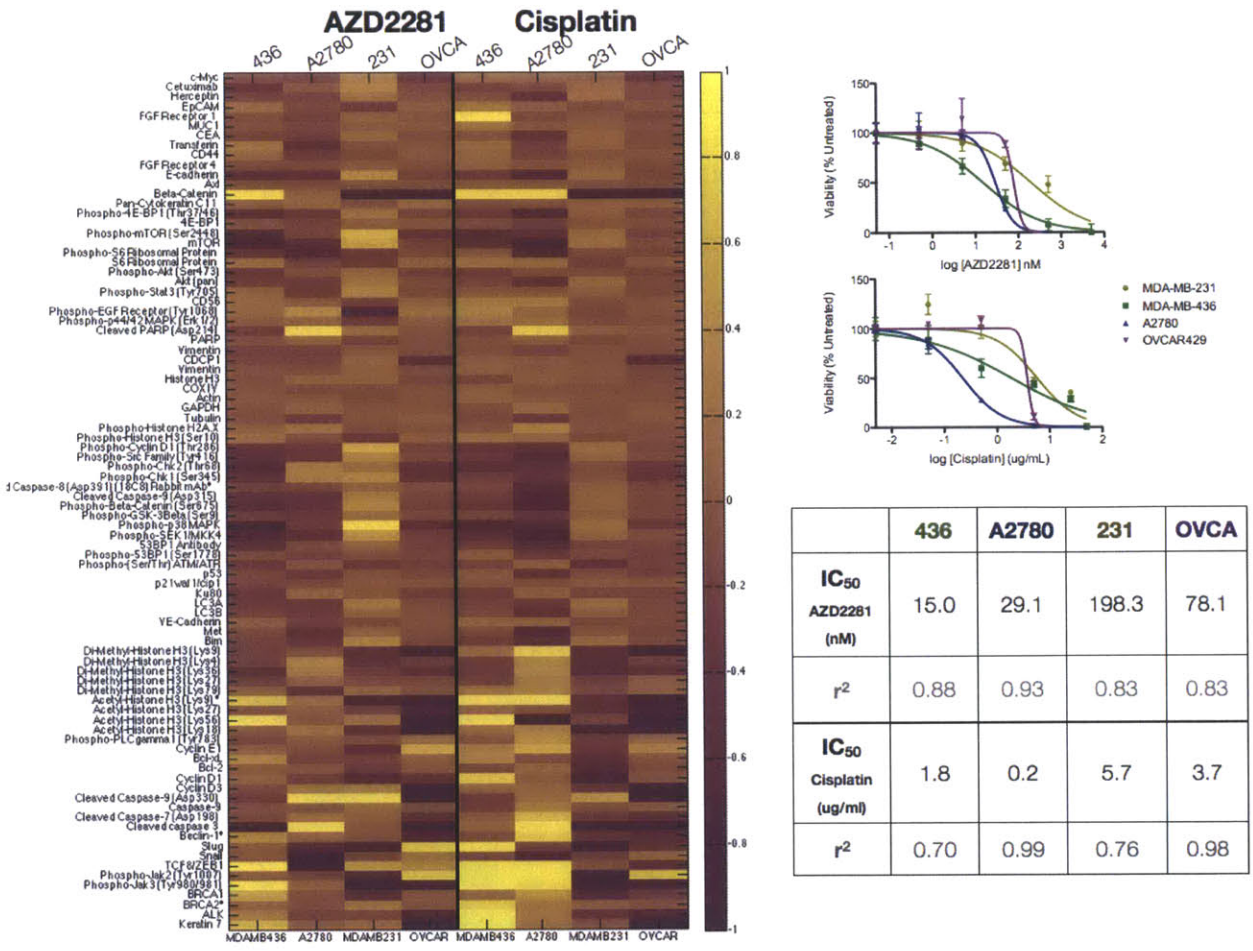

	436	A2780	231	OVCA
IC_{50} AZD2281 (nM)	15.0	29.1	198.3	78.1
r^2	0.88	0.93	0.83	0.83
IC_{50} Cisplatin (ug/ml)	1.8	0.2	5.7	3.7
r^2	0.70	0.99	0.76	0.98

Figure 4.10. Olaparib and Cisplatin In Vitro Profiling Correlates to Drug Sensitivity. We profiled 4 cell lines with varying sensitivities (viability curves shown on right) to the PARP inhibitor Olaparib (AZD2281) and the chemotherapeutic cisplatin. Heatmap data is normalized by row to show differences across cell lines and the two treatments (log scale). A number of key changes can be seen in DNA repair and epigenetic pathways. Samples were performed in biological triplicate.

4.2.4 Translation to Clinical Samples: Molecular and Therapeutic Profiling

We extended our analyses to clinical material to study intratumoral heterogeneity (at the single cell level), interpatient variability (amongst a cohort of lung cancer patients), and therapeutic response (in patients receiving a Phase I PI3K inhibitor).

We first examined single cell heterogeneity in a fine needle aspirate sample from a patient with with lung adenocarcinoma (Fig. 4.11). All investigated extracellular proteins as well as many intracellular

proteins were detectable in each of the samples. Single cells (EpCam+, DAPI+, CD45-) showed good correlation to the bulk measurement but with lower correlations and wider spread compared to cell line data. The highest correlation to bulk was 0.79 (cell culture showed R= 0.96), while the lowest value was 0.43. This supports the notion that clinical samples have greater heterogeneity than cell culture and in vitro cancer models do not fully capture tumor phenotypes. These data shows the need for better, more frequent clinical profiling techniques such as the one presented in this thesis.

A

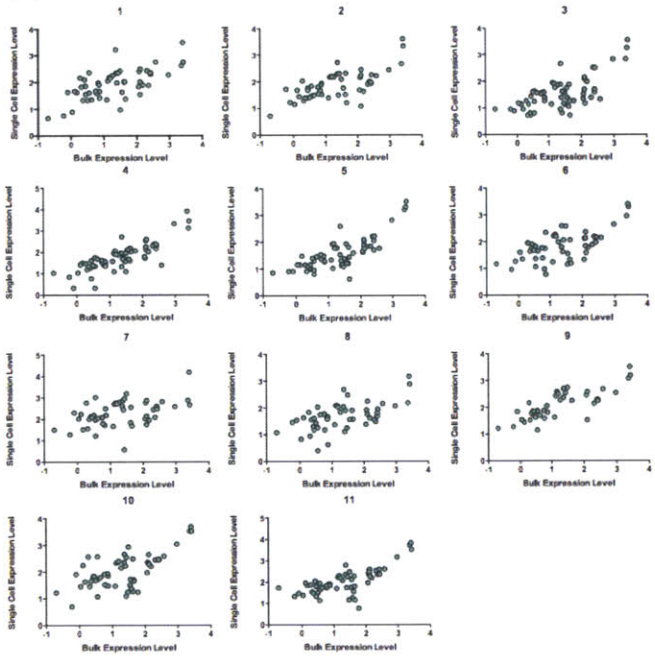

B

	1	2	3	4	5	6	7	8	9	10	11
1		0.804	0.598	0.67	0.618	0.725	0.8	0.71	0.826	0.837	0.812
2	0.804		0.743	0.697	0.714	0.794	0.77	0.772	0.809	0.799	0.775
3	0.598	0.743		0.802	0.886	0.744	0.6	0.73	0.68	0.671	0.755
4	0.67	0.697	0.802		0.883	0.646	0.556	0.664	0.718	0.654	0.755
5	0.618	0.714	0.886	0.883		0.739	0.555	0.705	0.742	0.644	0.819
6	0.725	0.794	0.744	0.646	0.739		0.749	0.766	0.818	0.789	0.765
7	0.8	0.77	0.6	0.556	0.555	0.749		0.815	0.889	0.875	0.732
8	0.71	0.772	0.73	0.664	0.705	0.766	0.815		0.888	0.768	0.8
9	0.826	0.809	0.68	0.718	0.742	0.818	0.889	0.888		0.909	0.851
10	0.837	0.799	0.671	0.654	0.644	0.789	0.875	0.768	0.899		0.86
11	0.812	0.775	0.755	0.755	0.819	0.765	0.732	0.8	0.851	0.86	
Bulk	0.626	0.62	0.562	0.796	0.727	0.539	0.433	0.542	0.77	0.54	0.656

Figure 4.11. Single-cell Profiling in Patient Sample. A fine needle aspirate was obtained from a patient with biopsy-proven lung adenocarcinoma. (A) Eleven harvested cells were analyzed individually, and protein expression levels in each cell (y axis) were correlated with expression levels from the bulk tumor sample (x axis). Though all of the cells show a linear trend, the spread and distribution of the markers varies from cell to cell. (B) Spearman R correlation coefficient values are displayed for each of the single cells to each other and to the bulk measurement ($p<.0001$). Single cells showed higher correlations to each other as compared to the bulk.

We then examined the heterogeneity amongst a cohort of patients with identical histopathological diagnoses of lung adenocarcinoma. Snapshot genotyping through MGH provided insights into the genetic basis of differences. We examined each proteomic profile to see how genetic-proteomic differences could differ or concur. Specifically we looked at four patients with EGFR mutations (two exon 19 amplifications with T790m mutations; one exon 20 mutation and one L858R sensitizing mutation with a BRAF mutation). We also looked an one patient with an EML4-ALK mutation and another with a KRAS mutation. The patients with the EGFR T790M mutations and KRAS mutation had very similar profiles (Figure 4.12). This suggests that different genotypes may result in similar proteomic phenotypes and is consistent with the observation that both EGFR T790M and KRAS mutations are known markers for resistance to EGFR inhibitor therapy.[32,152] Protein clustering also reveals interesting personalized targets. For example, Patient 4 (EGFR/BRAF mutant) had high phospho-ERK1/2 and phospho-s6rp as expected; however, this patient also showed a high level of PARP, Ku80 and pH2A.x, which are markers for DNA repair/damage. This suggests that PARP inhibitors or DNA damaging agents (cisplatin) could be effective in this patient.

An emerging clinical approach in oncology employs frequent resampling of primary cancers to more rationally assess the effect of a given drug and its dosage.[153] The ability to analyze small numbers of cells is critical, since repeat biopsies are difficult as tumors shrink post-treatment. Furthermore, risk of morbidity and high cost preclude highly invasive procedures to collect large tissue samples. We performed scant cell analyses in 4 patients before and after treatment with new PIK3CA inhibitors (Fig. 4.13). All of these patients were sampled either the day before or two days before the start of their treatment cycle and followed up with sampling at the end of the cycle. The first patient (leftmost), was a colorectal cancer patient with KRAS and TP53 mutations. The second patient (second to left) also had a colorectal cancer with a TP53 mutation and Her2 amplification. The third patient had endometrial carcinoma with mutant PIK3CA G1049R mutations and the

fourth patient (rightmost column) had a salivary gland tumor with a PIK3CA mutation. we compared the fold changes pre and post-treatment to observe global differences in each of these patients. Profiles clustered into the two patients that responded and the two that progressed. The two responsive patients received two different doses of the same drug (400mg bid vs. 150 mg bid); interestingly, the patient with the higher dose experienced larger fold changes across the marker panel.

We also examined a cohort of pre-treatment samples form patients to see if comprehensive proteomic analyses to survey signaling pathways could aid in developing companion diagnostics (Fig. 4.13b). In this cohort, the 5 patients had different cancers but all had PIK3CA genetic mutations, yet went on to have mixed responses to a PI3K inhibitor. Specifically, Patient 1 had liposarcoma (PIK3CA G346R, P53 loss, RB1 truncation), Patient 2 had endometrial cancer (PIK3CA 3140A>G, MET mutation), Patient 3 had uterine sarcoma (PIK3CA Gln546Lys), Patient 4 had endometrial carcinoma (PIK3CA G1049R), and patient 5 had salivary gland carcinoma (Pik3CA). It was interesting to note that as the markers were chosen to reflect changes treatment, the samples clustered according to response, and not according to the originating site of a tumor (e.g. endometrial cancers did not cluster together). All of these patients had stage 4 cancer and samples were collected 1-7 days before treatment.

We employed a marker ranking algorithm to determine which markers differentiated responders and non-responders. The top hit was H3K79me2. This marker clustered with a number of interesting markers: phospho-S6 RP (a known downstream target of PI3K), phospho-H2A.X, and PARP. These markers were also identified by the in vitro profiling of a PI3K inhibitor. This cluster covered diverse proteins across various pathways - epigenetic changes, DNA damage and pathway inhibition. Future targeted therapies will have to rely on biomarkers that are predictive of

treatment response, especially given the considerable costs of these types of treatments. Intra-tumor heterogeneity may itself be a biomarker of poor clinical outcome [157] and estimates of such heterogeneity may provide another approach to assess the propensity of the tumor to adapt to drug exposure.

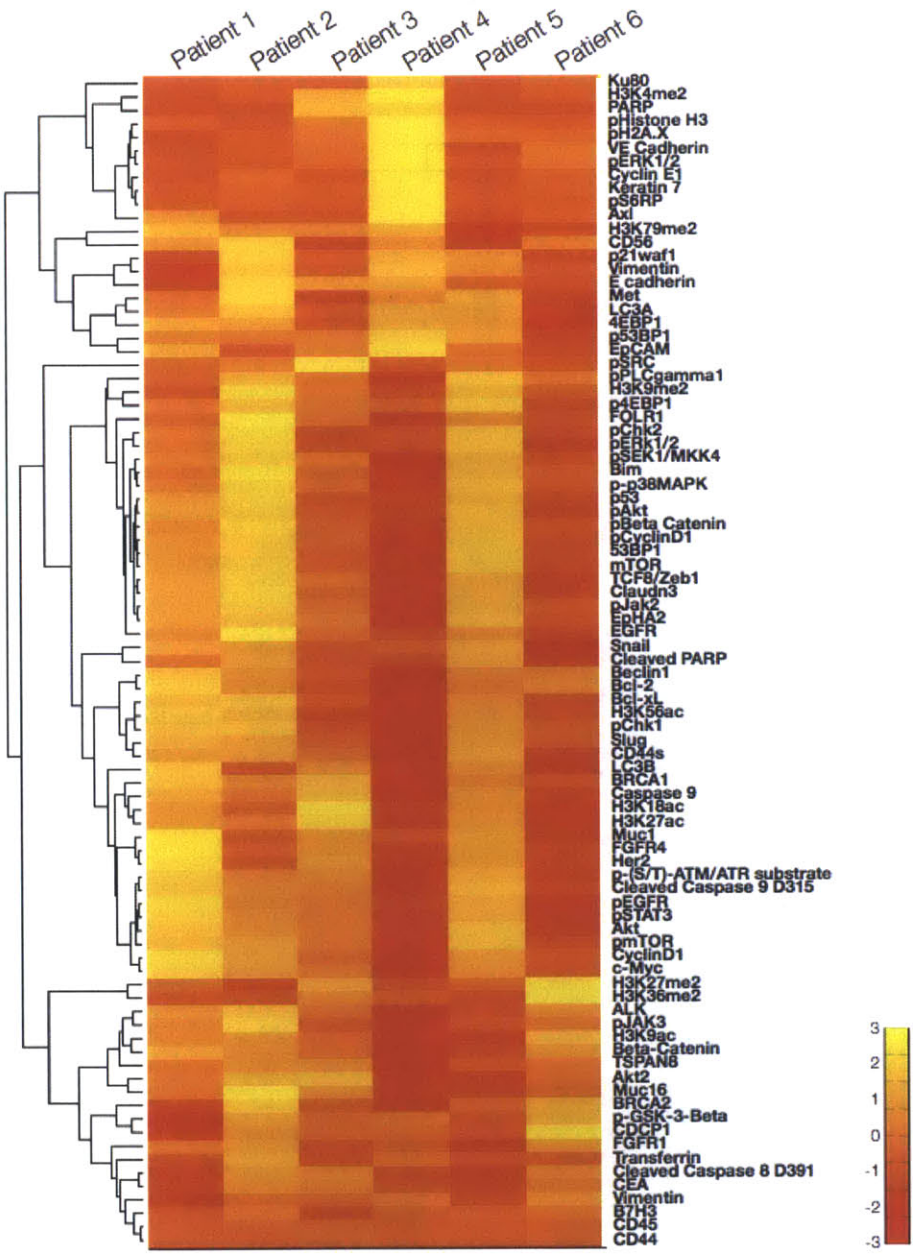

Figure 4.12. Inter-patient Heterogeneity in Lung Cancer. Fine needle aspirates were obtained from six patients with biopsy-proven lung adenocarcinoma, and bulk samples (~100 cells each) were processed as

described in Figure 4.1. Expression data is normalized by row to show differences between each patient. Clustering is based on correlation values. Patients 1, 2, and 5 showed similar protein profiles. This partially concurred with genotyping as both patients 1 and 2 had EGFR exon 19 amplification and T790m mutations. Patient 5 shows a similar profile but had a KRAS mutation. Patients 3, 4, and 6 all had distinct proteomic profiles, and all had differing mutations. Patient 3 had an exon 20 EGFR mutation, and patient 4 had an EGFR L858R mutation and an additional BRAF mutation. Patient 6 was noted to have an EML4-ALK translocation.

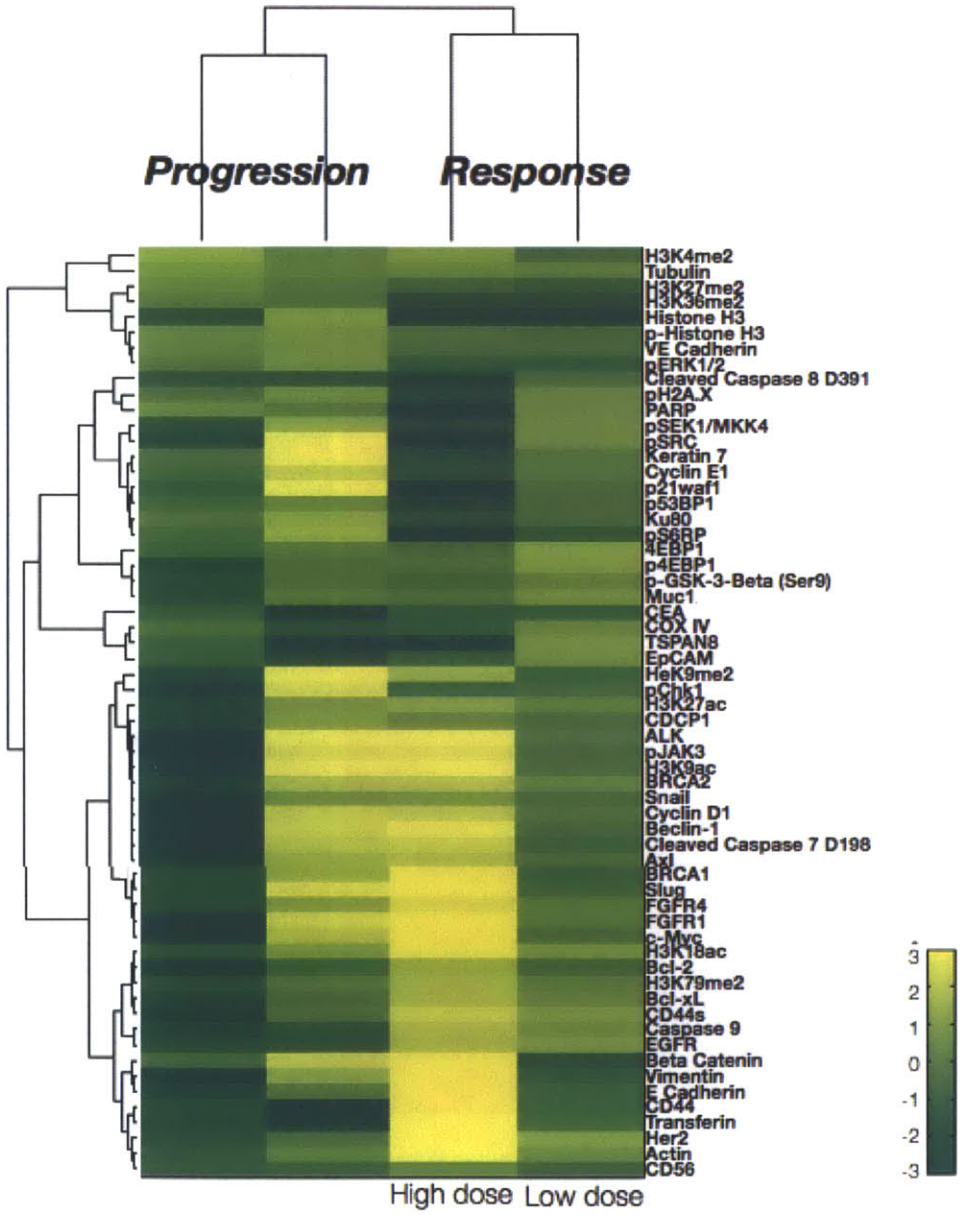

Figure 4.13. Treatment Changes post-PI3K Inhibitor. Four patients with biopsy-proven adenocarcinoma were treated with PI3K inhibitors, and primary cancers were biopsied before and after treatment. The heat map is a pre-post treatment difference map showing log2 fold changes in protein expression (normalized by row to highlight differences between patients). Patients segregate into two clusters (correlation distance metric; weighted linkage): tumors that responded and tumors that progressed. The patient in the third column received a higher dose of the PI3K inhibitor (400 mg bid as opposed to 150 mg bid) and showed greater up-regulation and down-regulation across the marker panel.

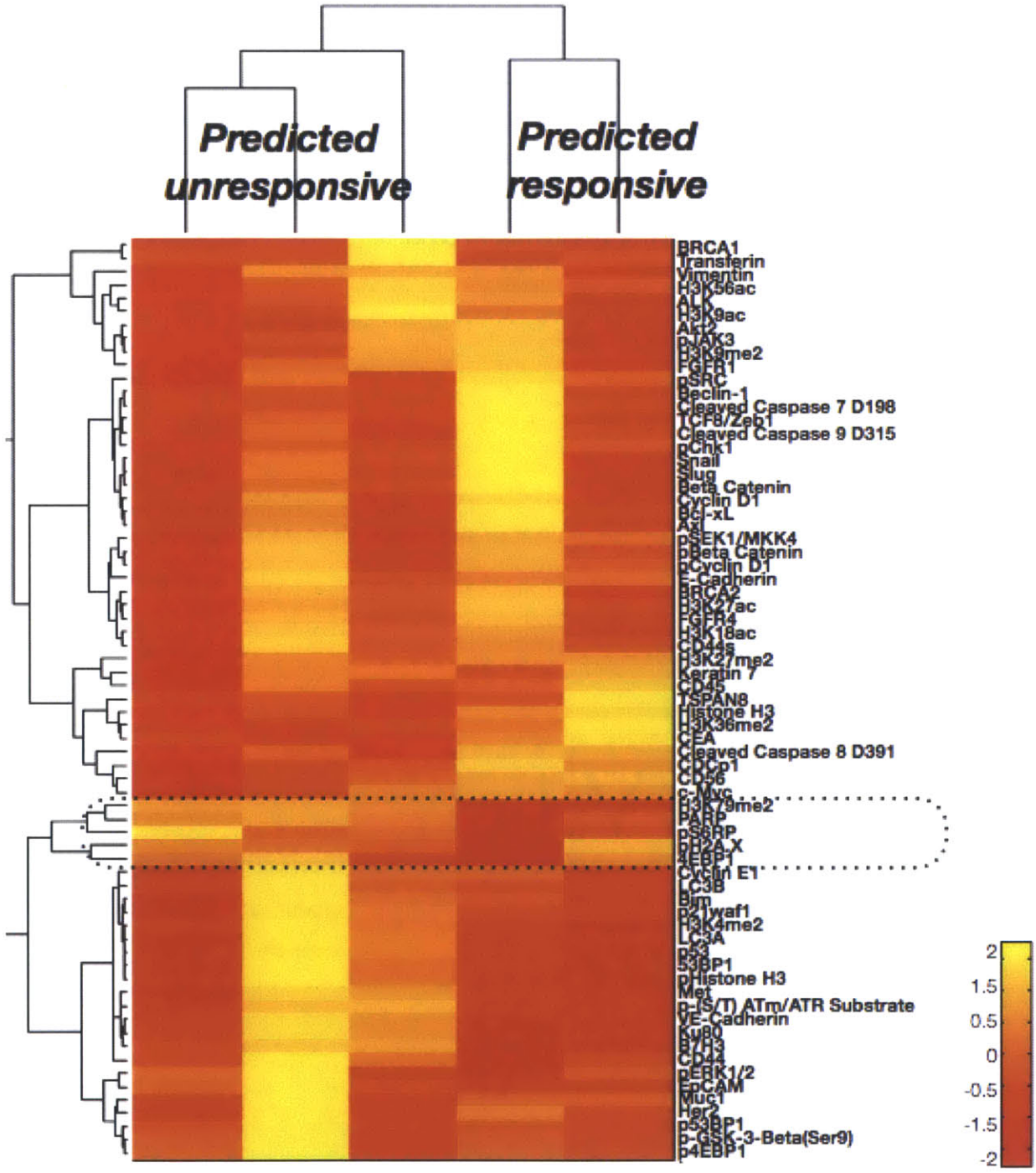

Figure 4.14. Pre-treatment profiles predict response to PI3K inhibitor. Profiles of five drug-naive lung cancer patients are shown with clustering based on correlation metrics with weighted linkage. The patients group into responders and non-responders. An algorithm to identify markers that separate drug-sensitive and drug-resistance classes identified H3K79me2 as the top hit, which clustered with many other markers

implicated in PI3Ki treatment including phospho-s6rp (dotted box). Heat map is normalized by row and shown on a log scale.

PI3K inhibitor: Significant Differential Markers
Di-Methyl-Histone H3 (Lys79)
LC3B
Cleaved Caspase-8 D391
Her2
VE-Cadherin
Beta Catenin
TSPAN8
Phospho-Cyclin D1
Bcl-xL
4EBP1

Table 4.3. Significant Differential Markers between Responders and Non-responders. The marker ranking algorithm identified ten key differential markers. Groups were defined by correlation clustering and markers were selected using the Bhattacharya distance metric.

4.2.5 Conclusion

In sum, we developed a photocleavable antibody-DNA barcoding conjugate technique for large-scale, multiplexed proteomic profiling with single cell sensitivity. This method allows for massive proteomic data collection that could advance basic research and inform clinical diagnosis and treatment decisions. In vitro profiling with a carefully selected marker panel distinguished drug treatments by differing mechanism of action, identified drug sensitivities, and even pointed to new drug combinations. Clinical sample profiling showed intratumoral heterogeneity, and variations in a seemingly 'homogenous' cohort of lung adenocarcinoma patients. Finally, we demonstrated the potential of proteomic profiling to predict and monitor patient response to cancer treatments.

4.2.6 Personal Contribution to Work

The author of this thesis led a group of researchers in designing, executing and interpreting experiments. This method was developed in equal collaboration with Vanessa Peterson.

4.3 Materials and Methods

Drug Treatments

Cell lines were given a variety of drug treatments at various doses. A431 cell lines were dosed with Gefitinib (Selleck Chemicals) in media with 1% DMSO overnight at a concentration of 10μM. The MDA-MB-436 cell line was dosed with the PARP inhibitor Olaparib (10μM in 0.1% DMSO in media), Cisplatin (10μM, 1% HBSS in media), PI3K/mTOR inhibitor PKI-587 (100nM, 0.1% DMSO/ media) and the EGFR inhibitors, Cetuximab (75 μg/ml in media), Gefitinib (10μM in 0.1% DMSO/ media). All molecular targeted agents (PKI-587, Cetuximab, Gefitinib) were incubated overnight with corresponding controls. DNA damaging agents Olaparib and Cisplatin were incubated with cells for 3 days. All fold changes are displayed compared to controls in media with no drug, but equivalent levels of DMSO, for the same period of time.

Immunofluorescence Validation

HT1080 cells were seeded in 96 well glass bottom plates (Grenier) compatible with high resolution imaging at 2,000 cells per well and grown for 24h in DMEM media before either being treated with Paclitaxel at 1μM, or kept in control media. After 24h, cells were fixed with 4% paraformaldehyde (diluted from 16% foramldehyde) for 15 minutes at room temperature, washed (PBS/1% Tween) and permeabilized with ice cold 90% methanol for 20 minutes. Cells were blocked, incubated with primary antibodies (Cell Signaling) overnight (4°C) and visualized after Hoescht and secondary antibody-FITC staining the following day. Multiple images were taken at using a 20x objective on a DeltaVision microscope. All markers were measured in biological triplicate. Fluorescence intensity for each cell was determined using CellProfiler, which used Hoescht and the whole cell stain to

delineate cell boundaries, and size constraints to discount debris. Additional in-house MatLab code was then used to calculate the marker signals for each condition and calculate the changes between treated and untreated.

Flow Cytometry Validation

Standard flow cytometry staining methods were used. 200,000 cells were used per vial. All primary antibodies were stained for one hour at room temperature at 1μg/ml or the recommended dilution. All secondary antibodies were incubated for 30 minutes at 2μg/ml. Measurements were performed on a LSRII flow cytometer. Fixable viability dyes were used in some cases.

Antibody Staining and DNA Collection for Proteomic Profiling

Cell staining for proteomic identification with Nanostring was based on standard flow cytometry staining methods. The pooled antibody cocktail was incubated for one hour at room temperature with intermittent vortexing. Staining with a large number of antibodies was comparable to single antibody staining; cell permeabilization also did not affect antibody binding. After incubation, the cells were washed (Perm/Wash buffer) on ice. Labeled cells could then be counted and selected for DNA release via cell lysis, proteolysis and photocleavage (UV long wavelength, 30 minutes). Supernatant from the lysate was collected and serial dilutions were performed in DNAse free water to collect DNA equivalent to 50-100 cells to avoid saturation of the Nanostring cartridge. This amount resulted in cartridge binding densities within the linear range of Nanostring quantitation. Binding densities lower than 0.2 were still linear and gave consistent proteomic profiles comparable to those in the highly quantitative, linear range.

Nanostring Materials and Processing

All capture and fluorescent probes were designed by Nanostring to be compatible with their Prep/ Analyzer stations. Commercial protocols for hybridization and detection from the DNA lysis sample were followed.

Single Cell Isolation and processing.

After antibody staining, single cells were picked using a micromanipulator. Cells were stained with Hoescht and added to an open 10cm dish and imaged using TE2000 microscope. Once cells were identified, the micromanipulator could be used to carefully select a single cell and place it directly into the PCR tube used in nanostring processing. Nanostring probes were then directly added to this tube according to commercial protocols.

Analysis

Calculating Proteomic Expression Profiles

Proteomic expression profiles were extracted from Nanostring raw data for DNA counts as follows: First, raw DNA counts were normalized by the mean of the internal nanostring positive controls. These counts were then converted to antibody expression values using the relative DNA/Ab counts we calculated. Average background signal from control IgG antibodies was then subtracted. Housekeeping genes were used for normalization. We normalized signals by Beta-tubulin as this provided the most consistent result. For the taxol treatments we normalized by Histone H3, GAPDH and Actin, since tubulin is a primary target of taxol. Data was transformed into log2 scale as denoted in captions.

Clustering

Heat maps and clustergrams were plotted using MatLab with a matrix input of marker expression values calculated as listed above. All clustergrams shown were performed using a weighted linkage and were clustered using correlation values as a distance metric. Some clustergrams were normalized by row as specified in captions to highlight differences of each marker between different patients. If a marker was not detectable in one of the patients it was removed from the matrix or heatmap and not displayed.

Statistical analysis: Correlations and Significant Marker Testing

Correlation between single cell analysis and bulk measurement was calculated in GraphPad Prism. Spearman R values were calculated without assuming a normal, consistent distribution. Two-sided p values were calculated.

Significant Markers were identified by comparing two groups (e.g. treated vs. untreated) in Prism and performing pairwise t-tests with an FDR of 0.2 for multiple test correction error. Significant markers and their p-values are displayed in supplementary tables.

To identify differentiating markers between responders and non-responders, we used a multi-class sequential forward selection ranking algorithm. We classified the patients into responders and non-responders based on known data. Class separability is measured by the Bhattacharya distance.

| Chapter 5 | Perspectives and Future Directions

This thesis describes several tools to address critical hurdles in monitoring tumors in cancer patients. The state of drug development and cancer treatment has remained largely unchanged for the last 30 years despite rising cost of care. We were motivated to change established pharmaceutical and therapeutic paradigms where limited data is collected during pre-clinical and clinical trails. We hypothesized that data-driven clinical trials that complemented current genomic analyses would increase the number of successful drug candidates and improve patient outcomes. Using micro and nanotechnologies, we sought to create tools and methods that could overcome a number of barriers to clinical translation. We developed a microfluidic device for circulating tumor cell isolation and characterization, a nanoparticle assay to study drug binding, and a DNA barcoding technology for massive proteomic profiling. All three projects laid the groundwork for the adaptation of biomedical research techniques into clinical practice. By building on this foundation, we envision a future with data-driven clinical trials and improved cancer treatment regimens.

In the first project, we designed and engineered a microfluidic CTC isolation device that integrated two distinct cell separation technologies, namely a self-assembled magnetic filter and a size-based sorter. This allowed for the efficient isolation of CTCs in an unbiased manner with improved throughput and cell-capture accuracy. On-chip profiling can also enable cellular studies at single cell resolution. With such advanced features, the HMSS chip could play an important role in translational cancer research. Since peripheral blood is easier to acquire from patients repeatedly, this device enables us to study CTCs in patients over time. We plan on using the HMSS system with clinical samples to look at a variety of markers that are relevant to pathway inhibition in molecularly targeted treatments to chart how the molecular phenotypes of CTCs change throughout treatment. Ultimately, we envision that the technological advancements in HMSS device would aid in understanding the underlying biology of CTCs as well as in establishing their clinical

utility. Furthermore, this device can be used in conjunction with the methods described in this thesis to understand intratumoral heterogeneity on a single cell level and the pharmacodynamic properties of circulating tumor cells.

In the second project, we addressed current limitations in clinical trails to accurately measure drug binding and dosing. Currently these measurements are made with radioactive probes and only performed in one or two patients due to ethical issues. However, our magnetic nanoparticle assay allowed for measurement of drug binding and quantification with ex vivo samples isolated from blood. The ability to provide such data in biologically relevant samples could be of considerable clinical interest to make rational treatment decisions, optimize doses in a given patient and understand population heterogeneities of drug responses. The method could also serve to quantitate the effective drug target resident time in readily accessible samples such as peripheral blood. In sum, we designed and developed a paradigm using small molecule nanoparticle conjugates that have the potential to address several clinical limitations and to impact patient treatment. We are advancing and testing this method with other small molecule drugs such as the ALK inhibitor Crizotinib and plan on applying measurements to study drug dosing in vivo. Future experiments could also examine drug distribution in metastases vs primary tumor in a mouse model. Finally, we plan on using our assay to study drug binding differences across cell lines with differing drug sensitivities. Such an assay could allow for researchers and clinicians to disentangle treatment failure as a result of drug targeting or cell efflux as opposed to efficacy.

The final project was motivated by the scarcity of proteomic information measured in clinical trials for cancer treatments. Though vast genomic information has been collected, this information has resulted in only a few successes; moreover, it has been a great challenge to discriminate between true driver oncogenes as opposed to passenger mutations. We developed a photocleavable DNA barcoding immunodetection method for sensing tens to hundreds of key proteins in human cells.

Combining several well-established techniques, this is currently the only methodology with the potential to simultaneously assay over 100 markers at the single cell level, requiring far less sample material than multiplexed FACS, immunohistochemistry or mass cytometry. Using this method, we demonstrate how insights into cancer biology insights including intratumoral heterogeniety, patient diversity, and changes in tumor biology following selection pressures from therapy could have important clinical implications. Furthermore, the assay allows for downstream processing, making it compatible for concurrent genetic measurements. Proteomic profiling during pre-clinical and clinical trials can lead to more effective therapies and cheaper drug development. In the future, we expect that the method can be applied to perform protein mapping across patients, characterize the tumor-stroma interactions, profile rare circulating tumors cells, and perhaps even explain clonal evolution in tumors via topological visualization of several proteins.

Currently we are performing further in depth studies of cancer treatment response by 1) exploring possible synergistic combinations as identified by our screen (e.g. PARPi and PI3Ki; PI3Ki and EGFRi) 2) understanding how Wnt signaling connects to PARP sensitivity 3) demonstrating feasibility of personalized treatments through integrative profiling of patient-derived cell lines. Specifically, for aim 3, we are performing concurrent RNA/DNA/proteomic profiling on ovarian cancer samples and comparing profiling changes to drug sensitivities from patient-derived cell lines, and clinical response. In addition, we plan to profile circulating tumor cells and compare their proteomic profiles to that of the primary tumor.

This tool can enable a number of other projects that can yield great insights into cancer evolution, and the tumor microenvironment. In particular, we can see how this method can be used to perform large-scale profiling on numerous single cells. It will be interesting to see if proteomic heterogeneity is actually greater or less than the variations captured by single cell genotyping. With

concurrent RNA/DNA/proteomic measurements, this tool could also show how the branched evolution of cancer clones agrees or differs based on genetic or proteomic measurements. This methodology could also be used as powerful tool to fully understand stromal cells that support the tumor. There is mounting evidence that endothelial cells promote tumor vascularization to sustain tumor growth, while host immune cells can act as immune shields to disguise the tumor from the body's natural defense. These cell populations can be selected by single cell sorting methods (FACS, micromanipulation, laser capture microdissection) based on well established and well defined markers. Follow up profiling with our method could reveal the cell's phenotype and tumor-supportive or tumor-protective activities in stromal cells. These experiments would not only advance our biological understanding, but also evince new drug targets and biomarkers for cancer therapeutics.

The "war" on cancer was declared in the 1970s. While there has been no single cure, we have advanced our knowledge on cancer and are better equipped to manage this heterogeneous, evolving disease. The research community exploited advances in genomics to afford select patients groups entirely new targeted therapeutics and prolong their lives by years. New hallmarks of cancer and pathways have been identified (e.g. epigenetic histone and bromodomain targets).[158,159] Immunotherapies designed to target not the tumor but the surrounding inflammatory milieu have shown dramatic responses in patients.[160] These novel methods show how insights into cancer have rapidly progressed from biological study into the clinic. We anticipate that the knowledge derived from translational biomedical tools will redefine our 'war' with cancer and turn this deadly disease into a treatable, manageable one.

I Bibliography I

1. Siegel, R., Naishadham, D. & Jemal, A. Cancer statistics, 2012. *CA: a cancer journal for clinicians* 62, 10-29 (2012).
2. Schilsky, R. L. Personalized medicine in oncology: the future is now. *Nature Reviews Drug Discovery* **9**, 363-366 (2010).
3. Hood, L., Heath, J. R., Phelps, M. E. & Lin, B. Systems biology and new technologies enable predictive and preventative medicine. *Science Signaling* **306**, 640 (2004).
4. Aspinall, M. G. & Hamermesh, R. G. Realizing the promise of personalized medicine. *Harvard business review* **85**, 108 (2007).
5. Dannenberg, J. H. & Berns, A. Drugging drug resistance. *Cell* **141**, 18-20 (2010).
6. Hutchinson, L. Personalized cancer medicine: era of promise and progress. *Nat Rev Clin Oncol* **8**, 121 (2011).
7. Yap, T. A., Gerlinger, M., Futreal, P. A., Pusztai, L. & Swanton, C. Intratumor heterogeneity: seeing the wood for the trees. *Sci Transl Med* **4**, 127ps10 (2012).
8. Gerlinger, M. et al. Intratumor heterogeneity and branched evolution revealed by multiregion sequencing. *New England Journal of Medicine* **366**, 883-892 (2012).
9. Anderson, K. et al. Genetic variegation of clonal architecture and propagating cells in leukaemia. *Nature* **469**, 356-361 (2010).
10. Heng, H. H. et al. Genetic and epigenetic heterogeneity in cancer: a genome-centric perspective. *J Cell Physiol* **220**, 538-547 (2009).
11. Navin, N. et al. Tumour evolution inferred by single-cell sequencing. *Nature* **472**, 90-94 (2011).
12. Kreso, A. et al. Variable clonal repopulation dynamics influence chemotherapy response in colorectal cancer. *Science* **339**, 543-548 (2013).
13. Luo, J., Solimini, N. L. & Elledge, S. J. Principles of cancer therapy: oncogene and non-oncogene addiction. *Cell* **136**, 823-837 (2009).
14. Chan, N. et al. Contextual synthetic lethality of cancer cell kill based on the tumor microenvironment. *Cancer Res* **70**, 8045-8054 (2010).
15. Chmielecki, J. et al. Optimization of dosing for EGFR-mutant non-small cell lung cancer with evolutionary cancer modeling. *Sci Transl Med* **3**, 90ra59 (2011).
16. Hanahan, D. & Weinberg, R. A. Hallmarks of cancer: the next generation. *Cell* **144**, 646-674 (2011).
17. Widschwendter, M. et al. Epigenetic stem cell signature in cancer. *Nat Genet* **39**, 157-158 (2007).
18. Vivanco, I. & Sawyers, C. L. The phosphatidylinositol 3-kinase–AKT pathway in human cancer. *Nature Reviews Cancer* **2**, 489-501 (2002).
19. Nowell, P. C. The clonal evolution of tumor cell populations. *Science* **194**, 23-28 (1976).

20. Eisbruch, A. Clinical heterogeneity and tumor control probability. *Acta Oncologica* **49**, 1385-1387 (2010).
21. Kelland, L. The resurgence of platinum-based cancer chemotherapy. *Nature Reviews Cancer* **7**, 573-584 (2007).
22. Chabner, B. A. & Longo, D. L. *Cancer chemotherapy and biotherapy: principles and practice* (LWW, 2011).
23. Wood, A. J. J., Rowinsky, E. K. & Donehower, R. C. Paclitaxel (taxol). *New England Journal of Medicine* **332**, 1004-1014 (1995).
24. Weinstein, I. B. & Joe, A. Oncogene addiction. *Cancer Research* **68**, 3077-3080 (2008).
25. Druker, B. J. et al. Activity of a specific inhibitor of the BCR-ABL tyrosine kinase in the blast crisis of chronic myeloid leukemia and acute lymphoblastic leukemia with the Philadelphia chromosome. *New England Journal of Medicine* **344**, 1038-1042 (2001).
26. Paez, J. G. et al. EGFR mutations in lung cancer: correlation with clinical response to gefitinib therapy. *Science Signaling* **304**, 1497 (2004).
27. Soda, M. et al. Identification of the transforming EML4–ALK fusion gene in non-small-cell lung cancer. *Nature* **448**, 561-566 (2007).
28. Li, R. & Morris, S. W. Development of anaplastic lymphoma kinase (ALK) small-molecule inhibitors for cancer therapy. *Med Res Rev* **28**, 372-412 (2008).
29. Baselga, J. et al. Phase II study of weekly intravenous trastuzumab (Herceptin) in patients with HER2/neu-overexpressing metastatic breast cancer. **Seminars in oncology 26(4 Suppl 12)**, 78 (1999).
30. McCabe, N. et al. Deficiency in the repair of DNA damage by homologous recombination and sensitivity to poly(ADP-ribose) polymerase inhibition. *Cancer Res* **66**, 8109-8115 (2006).
31. Hastak, K., Alli, E. & Ford, J. M. Synergistic chemosensitivity of triple-negative breast cancer cell lines to poly(ADP-Ribose) polymerase inhibition, gemcitabine, and cisplatin. *Cancer Res* **70**, 7970-7980 (2010).
32. Pao, W. et al. Acquired resistance of lung adenocarcinomas to gefitinib or erlotinib is associated with a second mutation in the EGFR kinase domain. *PLoS medicine* **2**, e73 (2005).
33. He, K., Xu, T. & Goldkorn, A. Cancer cells cyclically lose and regain drug-resistant highly tumorigenic features characteristic of a cancer stem-like phenotype. *Mol Cancer Ther* **10**, 938-948 (2011).
34. Porter, D. L., Levine, B. L., Kalos, M., Bagg, A. & June, C. H. Chimeric antigen receptor-modified T cells in chronic lymphoid leukemia. *N Engl J Med* **365**, 725-733 (2011).
35. Atkins, D. et al. Immunohistochemical Detection of EGFR in Paraffin-embedded Tumor Tissues Variation in Staining Intensity Due to Choice of Fixative and Storage Time of Tissue Sections. *Journal of Histochemistry & Cytochemistry* **52**, 893-901 (2004).

36. Limon, J., Dal Cin, P. & Sandberg, A. A. Application of long-term collagenase disaggregation for the cytogenetic analysis of human solid tumors. *Cancer genetics and cytogenetics* **23**, 305-313 (1986).
37. Haun, J. B. et al. Micro-NMR for rapid molecular analysis of human tumor samples. *Sci Transl Med* **3**, 71ra16 (2011).
38. Young, N. A., Al-Saleem, T. I., Ehya, H. & Smith, M. R. Utilization of fine-needle aspiration cytology and flow cytometry in the diagnosis and subclassification of primary and recurrent lymphoma. *Cancer Cytopathology* **84**, 252-261 (1998).
39. Pantel, K. & Alix-Panabières, C. The clinical significance of circulating tumor cells. *Nature Clinical Practice Oncology* **4**, 62-63 (2007).
40. Stott, S. L. et al. Isolation of circulating tumor cells using a microvortex-generating herringbone-chip. *Proceedings of the National Academy of Sciences* **107**, 18392-18397 (2010).
41. Stott, S. L. et al. Isolation and characterization of circulating tumor cells from patients with localized and metastatic prostate cancer. *Science translational medicine* **2**, 25ra23 (2010).
42. Bujalkova, M. et al. Multiplex SNaPshot genotyping for detecting loss of heterozygosity in the mismatch-repair genes MLH1 and MSH2 in microsatellite-unstable tumors. *Clinical chemistry* **54**, 1844-1854 (2008).
43. Cronin, M. et al. Analytical validation of the Oncotype DX genomic diagnostic test for recurrence prognosis and therapeutic response prediction in node-negative, estrogen receptor–positive breast cancer. *Clinical chemistry* **53**, 1084-1091 (2007).
44. Kumar, V., Abbas, A. K., Fausto, N. & Aster, J. C. Robbins & Cotran pathologic basis of disease. *books.google.com* (2009).
45. Vogelstein, B. et al. Cancer genome landscapes. *Science* **339**, 1546-1558 (2013).
46. Di Loreto, C. et al. Immunocytochemical expression of tissue specific transcription factor-1 in lung carcinoma. *Journal of clinical pathology* **50**, 30-32 (1997).
47. Whiteaker, J. R. et al. A targeted proteomics-based pipeline for verification of biomarkers in plasma. *Nat Biotechnol* **29**, 625-634 (2011).
48. Bandura, D. R. et al. Mass cytometry: technique for real time single cell multitarget immunoassay based on inductively coupled plasma time-of-flight mass spectrometry. *Analytical Chemistry* **81**, 6813-6822 (2009).
49. Bendall, S. C. et al. Single-cell mass cytometry of differential immune and drug responses across a human hematopoietic continuum. *Science* **332**, 687-696 (2011).
50. Ornatsky, O. et al. Highly multiparametric analysis by mass cytometry. *Journal of immunological methods* **361**, 1-20 (2010).
51. Benoist, C. & Hacohen, N. Immunology. Flow cytometry, amped up. *Science* **332**, 677-678 (2011).

52. Krutzik, P. O. & Nolan, G. P. Intracellular phospho-protein staining techniques for flow cytometry: monitoring single cell signaling events. *Cytometry A* **55**, 61-70 (2003).
53. Salieb-Beugelaar, G. B., Simone, G., Arora, A., Philippi, A. & Manz, A. Latest developments in microfluidic cell biology and analysis systems. *Analytical chemistry* **82**, 4848 (2010).
54. Haun, J. B., Yoon, T. J., Lee, H. & Weissleder, R. Molecular detection of biomarkers and cells using magnetic nanoparticles and diagnostic magnetic resonance. *Methods Mol Biol* **726**, 33-49 (2011).
55. Weissleder, R. Molecular imaging in cancer. *Science Signaling* **312**, 1168 (2006).
56. Farokhzad, O. C. & Langer, R. Impact of nanotechnology on drug delivery. *ACS nano* **3**, 16-20 (2009).
57. Tassa, C. et al. Binding affinity and kinetic analysis of targeted small molecule-modified nanoparticles. *Bioconjug Chem* **21**, 14-19 (2010).
58. Ferrari, M. Cancer nanotechnology: opportunities and challenges. *Nature Reviews Cancer* **5**, 161-171 (2005).
59. Gottlieb, M. S., Schroff, R., Schanker, H. M. & Weisman, J. D. Pneumocystis carinii pneumonia and mucosal candidiasis in previously healthy homosexual men - evidence of a new acquired cellular immunodeficiency. *The New England Journal of Medicine* **305**, 1425-1431 (1981).
60. Fan, R. et al. Integrated barcode chips for rapid, multiplexed analysis of proteins in microliter quantities of blood. *Nat Biotechnol* **26**, 1373-1378 (2008).
61. Nagrath, S. et al. Isolation of rare circulating tumour cells in cancer patients by microchip technology. *Nature* **450**, 1235-1239 (2007).
62. Mattanovich, D. & Borth, N. Applications of cell sorting in biotechnology. *Microb Cell Fact* **5**, 12 (2006).
63. Lagasse, E. et al. Purified hematopoietic stem cells can differentiate into hepatocytes in vivo. *Nature medicine* **6**, 1229-1234 (2000).
64. Issadore, D. et al. Ultrasensitive Clinical Enumeration of Rare Cells ex Vivo Using a Micro-Hall Detector. *Sci Transl Med* **4**, 141ra92 (2012).
65. Lang, J. M., Casavant, B. P. & Beebe, D. J. Circulating tumor cells: getting more from less. *Sci Transl Med* **4**, 141ps13 (2012).
66. Adams, J. D., Kim, U. & Soh, H. T. Multitarget magnetic activated cell sorter. *Proc Natl Acad Sci USA* **105**, 18165-18170 (2008).
67. Han, K. & Bruno Frazier, A. Continuous magnetophoretic separation of blood cells in microdevice format. *Journal of Applied Physics* **96**, 5797 (2004).
68. Inglis, D. W., Riehn, R., Austin, R. H. & Sturm, J. C. Continuous microfluidic immunomagnetic cell separation. *American Physics Letters* **85**, 37013 (2004).
69. Issadore, D. et al. Self-assembled magnetic filter for highly efficient immunomagnetic separation. *Lab Chip* **11**, 147-151 (2011).

70. Wheeler, A. R. et al. Microfluidic device for single-cell analysis. *Anal Chem* **75**, 3581-3586 (2003).
71. Toriello, N. M. et al. Integrated microfluidic bioprocessor for single-cell gene expression analysis. *Proc Natl Acad Sci USA* **105**, 20173-20178 (2008).
72. Chung, J. et al. Microfluidic Cell Sorter (μFCS) for On-chip Capture and Analysis of Single Cells. *Adv Healthc Mater* **1**, 432-436 (2012).
73. Lee, H., Sun, E., Ham, D. & Weissleder, R. Chip-NMR biosensor for detection and molecular analysis of cells. *Nat Med* **14**, 869-874 (2008).
74. Tassa, C., Shaw, S. Y. & Weissleder, R. Dextran-coated iron oxide nanoparticles: a versatile platform for targeted molecular imaging, molecular diagnostics, and therapy. *Acc Chem Res* **44**, 842-852 (2011).
75. Geiss, G. K. et al. Direct multiplexed measurement of gene expression with color-coded probe pairs. *Nature biotechnology* **26**, 317-325 (2008).
76. Lin, C. et al. Submicrometre geometrically encoded fluorescent barcodes self-assembled from DNA. *Nature Chemistry* **4**, 832-839 (2012).
77. Niemeyer, C. M., Adler, M. & Wacker, R. Detecting antigens by quantitative immuno-PCR. *Nature protocols* **2**, 1918-1930 (2007).
78. Fredriksson, S. et al. Multiplexed protein detection by proximity ligation for cancer biomarker validation. *Nature methods* **4**, 327-329 (2007).
79. Kazane, S. A. et al. Site-specific DNA-antibody conjugates for specific and sensitive immuno-PCR. *Proceedings of the National Academy of Sciences* **109**, 3731-3736 (2012).
80. Shi, Q. et al. Single-cell proteomic chip for profiling intracellular signaling pathways in single tumor cells. *Proceedings of the National Academy of Sciences* **109**, 419-424 (2012).
81. Chaffer, C. L. & Weinberg, R. A. A perspective on cancer cell metastasis. *Science* **331**, 1559-1564 (2011).
82. Cristofanilli, M. et al. Circulating tumor cells, disease progression, and survival in metastatic breast cancer. *N Engl J Med* **351**, 781-791 (2004).
83. Maheswaran, S. et al. Detection of mutations in EGFR in circulating lung-cancer cells. *N Engl J Med* **359**, 366-377 (2008).
84. Pierga, J. Y. et al. Circulating tumor cell detection predicts early metastatic relapse after neoadjuvant chemotherapy in large operable and locally advanced breast cancer in a phase II randomized trial. *Clin Cancer Res* **14**, 7004-7010 (2008).
85. Yu, M. et al. RNA sequencing of pancreatic circulating tumour cells implicates WNT signalling in metastasis. *Nature* **487**, 510-513 (2012).
86. Stott, S. L. et al. Isolation and characterization of circulating tumor cells from patients with localized and metastatic prostate cancer. *Sci Transl Med* **2**, 25ra23 (2010).

87. Miyamoto, D. T. et al. Androgen Receptor Signaling in Circulating Tumor Cells as a Marker of Hormonally Responsive Prostate Cancer. *Cancer Discov* **2**, 995-1003 (2012).
88. Yu, M., Stott, S., Toner, M., Maheswaran, S. & Haber, D. A. Circulating tumor cells: approaches to isolation and characterization. *J Cell Biol* **192**, 373-382 (2011).
89. Paterlini-Brechot, P. & Benali, N. L. Circulating tumor cells (CTC) detection: Clinical impact and future directions. *Cancer Letters* **253**, 180-204 (2007).
90. Zheng, S. et al. Membrane microfilter device for selective capture, electrolysis and genomic analysis of human circulating tumor cells. *J Chromatogr A* **1162**, 154-161 (2007).
91. Pantel, K., Brakenhoff, R. H. & Brandt, B. Detection, clinical relevance and specific biological properties of disseminating tumour cells. *Nature reviews Cancer* **8**, 329-340 (2008).
92. Lin, H. K. et al. Portable Filter-Based Microdevice for Detection and Characterization of Circulating Tumor Cells. *Clinical Cancer Research* **16**, 5011-5018 (2010).
93. Hur, S. C., Mach, A. J. & Carlo, D. D. High-throughput size-based rare cell enrichment using microscale vortices. *Biomicrofluidics* **5**, 022206 (2011).
94. Gradilone, A. et al. Circulating tumour cells lacking cytokeratin in breast cancer: the importance of being mesenchymal. *J Cell Mol Med* **15**, 1066-1070 (2011).
95. Lustberg, M., Jatana, K. R., Zborowski, M. & Chalmers, J. J. Emerging technologies for CTC detection based on depletion of normal cells. *Recent Results Cancer Res* **195**, 97-110 (2012).
96. Tan, W.-H. & Takeuchi, S. A trap-and-release integrated microfluidic system for dynamic microarray applications. *Proc Natl Acad Sci USA* **104**, 1146-1151 (2007).
97. Stott, S. L. et al. Isolation of circulating tumor cells using a microvortex-generating herringbone-chip. *Proc Natl Acad Sci U S A* **107**, 18392-18397 (2010).
98. Forbes, T. P. & Kralj, J. G. Engineering and analysis of surface interactions in a microfluidic herringbone micromixer. *Lab on a Chip* **12**, 2634 (2012).
99. Zhou, J., Khodakov, D. A., Ellis, A. V. & Voelcker, N. H. Surface modification for PDMS-based microfluidic devices. *Electrophoresis* **33**, 89-104 (2011).
100. Vuoriluoto, K. et al. Vimentin regulates EMT induction by Slug and oncogenic H-Ras and migration by governing Axl expression in breast cancer. *Oncogene* **30**, 1436-1448 (2011).
101. Blick, T. et al. Epithelial mesenchymal transition traits in human breast cancer cell lines. *Clin Exp Metastasis* **25**, 629-642 (2008).
102. Ulirsch, J. et al. Vimentin DNA methylation predicts survival in breast cancer. *Breast Cancer Res Treat* **137**, 383-396 (2013).
103. Wang, L. H. et al. Monitoring Drug-Induced H2AX as a Pharmacodynamic Biomarker in Individual Circulating Tumor Cells. *Clin Cancer Res* **16**, 1073-1084 (2010).
104. Kallergi, G. et al. Phosphorylated EGFR and PI3K/Akt signaling kinases are expressed in circulating tumor cells of breast cancer patients. *Breast Cancer Res* **10**, R80 (2008).

105. Giljohann, D. A. & Mirkin, C. A. Drivers of biodiagnostic development. *Nature* **462**, 461-464 (2009).
106. Cheng, M. M. et al. Nanotechnologies for biomolecular detection and medical diagnostics. *Curr Opin Chem Biol* **10**, 11-19 (2006).
107. Tassa, C., Duffner, J. L. & Lewisâ ¦, T. A. Binding affinity and kinetic analysis of targeted small molecule-modified nanoparticles. *Bioconjugate â ¦* (2009).
108. Hong, S., Leroueil, P., Majoros, I., Orr, B., Baker, J & Holl, M. The binding avidity of a nanoparticle-based multivalent targeted drug delivery platform. *Chemistry and Biology* **14**, 107-115 (2007).
109. Fan, R. et al. Integrated barcode chips for rapid, multiplexed analysis of proteins in microliter quantities of blood. *Nat Biotechnol* **26**, 1373-1378 (2008).
110. Haun, J. B., Devaraj, N. K., Hilderbrand, S. A., Lee, H. & Weissleder, R. Bioorthogonal chemistry amplifies nanoparticle binding and enhances the sensitivity of cell detection. *Nat Nanotechnol* **5**, 660-665 (2010).
111. Shaw, S. Y. et al. Perturbational profiling of nanomaterial biologic activity. *Proc Natl Acad Sci U S A* **105**, 7387-7392 (2008).
112. Lee, H., Yoon, T. J. & Weissleder, R. Ultrasensitive detection of bacteria using core-shell nanoparticles and an NMR-filter system. *Angew Chem Int Ed Engl* **48**, 5657-5660 (2009).
113. Perez, J. M., Josephson, L., O'Loughlin, T., Hogemann, D. & Weissleder, R. Magnetic relaxation switches capable of sensing molecular interactions. *Nat Biotechnol* **20**, 816-820 (2002).
114. Sun, E. Y., Weissleder, R. & Josephson, L. Continuous analyte sensing with magnetic nanoswitches. *Small* **2**, 1144-1147 (2006).
115. Swinney, DC & Anthony, J. How were new medicines discovered? *Nature Reviews Drug Discovery* (2011).
116. Issadore, D. et al. Miniature magnetic resonance system for point-of-care diagnostics. *Lab Chip* **11**, 2282-2287 (2011).
117. Johnson, N. et al. Compromised CDK1 activity sensitizes BRCA-proficient cancers to PARP inhibition. *Nat Med* **17**, 875-882 (2011).
118. Dedes, K. J. et al. PTEN deficiency in endometrioid endometrial adenocarcinomas predicts sensitivity to PARP inhibitors. *Sci Transl Med* **2**, 53ra75 (2010).
119. O'Shaughnessy, J. et al. Iniparib plus chemotherapy in metastatic triple-negative breast cancer. *N Engl J Med* **364**, 205-214 (2011).
120. Tutt, A., Robson, M., Garber, J. E. & Domchekâ ¦, S. M. Oral poly (ADP-ribose) polymerase inhibitor olaparib in patients with BRCA1 or BRCA2 mutations and advanced breast cancer: a proof-of-concept trial. *The Lancet* (2010).
121. He, J. X., Yang, C. H. & Miao, Z. H. Poly(ADP-ribose) polymerase inhibitors as promising cancer therapeutics. *Acta Pharmacol Sin* **31**, 1172-1180 (2010).

122. Menear, K. A., Adcock, C. & Boulterâ ¦, R. 4-[3-(4-Cyclopropanecarbonylpiperazine-1-carbonyl)-4-fluorobenzyl]-2 H-phthalazin-1-one: A Novel Bioavailable Inhibitor of Poly (ADP-ribose) Polymerase-1. *Journal of medicinal â ¦* (2008).
123. Keliher, E. J., Reiner, T., Turetsky, A., Hilderbrand, S. A. & Weissleder, R. High-yielding, two-step 18F labeling strategy for 18F-PARP1 inhibitors. *ChemMedChem* **6**, 424-427 (2011).
124. Reiner, T., Earley, S., Turetsky, A. & Weissleder, R. Bioorthogonal small-molecule ligands for PARP1 imaging in living cells. *Chembiochem* **11**, 2374-2377 (2010).
125. Ferraris, D. V. Evolution of poly (ADP-ribose) polymerase-1 (PARP-1) inhibitors. From concept to clinic. *Journal of medicinal chemistry* (2010).
126. Alber, F. et al. The molecular architecture of the nuclear pore complex. *Nature* **450**, 695-701 (2007).
127. Haun, J. B., Devaraj, N. K., Marinelli, B. S., Lee, H. & Weissleder, R. Probing intracellular biomarkers and mediators of cell activation using nanosensors and bioorthogonal chemistry. *ACS Nano* **5**, 3204-3213 (2011).
128. Haince, J. F. et al. PARP1-dependent kinetics of recruitment of MRE11 and NBS1 proteins to multiple DNA damage sites. *J Biol Chem* **283**, 1197-1208 (2008).
129. Meder, V. S., Boeglin, M., de Murcia, G. & Schreiber, V. PARP-1 and PARP-2 interact with nucleophosmin/B23 and accumulate in transcriptionally active nucleoli. *J Cell Sci* **118**, 211-222 (2005).
130. Miyashiro, J. et al. Synthesis and SAR of novel tricyclic quinoxalinone inhibitors of poly(ADP-ribose)polymerase-1 (PARP-1). *Bioorg Med Chem Lett* **19**, 4050-4054 (2009).
131. Karlberg, T., Hammarstrom, M., Schutz, P., Svensson, L. & Schuler, H. Crystal structure of the catalytic domain of human PARP2 in complex with PARP inhibitor ABT-888. *Biochemistry* **49**, 1056-1058 (2010).
132. Mendeleyev, J., Kirsten, E., Hakam, A., Buki, K. G. & Kun, E. Potential chemotherapeutic activity of 4-iodo-3-nitrobenzamide : Metabolic reduction to the 3-nitroso derivative and induction of cell death in tumor cells in culture. *Biochemical Pharmacology* **50**, 705-714 (1995).
133. Haun, J. B. et al. Micro-NMR for rapid molecular analysis of human tumor samples. *Sci Transl Med* **3**, 71ra16 (2011).
134. Brustmann, H. Poly (adenosine diphosphate-ribose) polymerase expression in serous ovarian carcinoma: correlation with p53, MIB-1, and outcome. *International Journal of Gynecologic Pathology* (2007).
135. von Minckwitz, G. et al. Cytoplasmic Poly (Adenosine Diphosphate–Ribose) Polymerase Expression Is Predictive and Prognostic in Patients With Breast Cancer Treated With Neoadjuvant Chemotherapy. *Journal of Clinical Oncology* **29**, 2150 (2011).

136. Haun, J. B., Devaraj, N. K., Marinelli, B. S., Lee, H. & Weissleder, R. Probing intracellular biomarkers and mediators of cell activation using nanosensors and bioorthogonal chemistry. *ACS Nano* **5**, 3204-3213 (2011).
137. Devaraj, N. K., Hilderbrand, S., Upadhyay, R., Mazitschek, R. & Weissleder, R. Bioorthogonal Turn-On Probes for Imaging Small Molecules inside Living Cells. *Angewandte Chemie* **122**, 2931-2934 (2010).
138. Reiner, T. et al. Near-Infrared Fluorescent Probe for Imaging of Pancreatic β Cells. *Bioconjugate chemistry* (2010).
139. Reiner, T., Keliher, E. J., Earley, S., Marinelli, B. & Weissleder, R. Synthesis and in vivo imaging of a 18F-labeled PARP1 inhibitor using a chemically orthogonal scavenger-assisted high-performance method. *Angew Chem Int Ed Engl* **50**, 1922-1925 (2011).
140. Budin, G., Yang, K. S. & Reinerâ ¦, T. Bioorthogonal Probes for Poloâ like Kinase 1 Imaging and Quantification. *Angewandte Chemie â ¦* (2011).
141. Tassa, C., Shaw, S. Y. & Weissleder, R. Dextran-Coated Iron Oxide Nanoparticles: A Versatile Platform for Targeted Molecular Imaging, Molecular Diagnostics, and Therapy. *Acc Chem Res* (2011).
142. Reynolds, F., O'Loughlin, T., Weissleder, R. & Josephson, L. Method of determining nanoparticle core weight. *Analytical chemistry* **77**, 814-817 (2005).
143. Hsi, E. D. A practical approach for evaluating new antibodies in the clinical immunohistochemistry laboratory. *Archives of pathology & laboratory medicine* **125**, 289-294 (2001).
144. Guo, J., Wang, S., Dai, N., Teo, Y. N. & Kool, E. T. Multispectral labeling of antibodies with polyfluorophores on a DNA backbone and application in cellular imaging. *Proceedings of the National Academy of Sciences* **108**, 3493-3498 (2011).
145. Shitashige, M., Hirohashi, S., Yamada, T. Wnt signaling inside the nucleus. *Cancer* Science 99, 631-637, (2008).
146. Farmer, H. et al. Targeting the DNA repair defect in BRCA mutant cells as a therapeutic strategy. *Nature* **434**, 917-921 (2005).
147. Jagtap, P. & Szabo, C. Poly(ADP-ribose) polymerase and the therapeutic effects of its inhibitors. *Nat Rev Drug Discov* **4**, 421-440 (2005).
148. Javle, M. & Curtin, N. J. The role of PARP in DNA repair and its therapeutic exploitation. *Br J Cancer* **105**, 1114-1122 (2011).
149. Thomas, H. D. et al. Preclinical selection of a novel poly(ADP-ribose) polymerase inhibitor for clinical trial. *Mol Cancer Ther* **6**, 945-956 (2007).
150. Anderson, V. E. et al. CCT241533 is a potent and selective inhibitor of CHK2 that potentiates the cytotoxicity of PARP inhibitors. *Cancer research* **71**, 463-472 (2011).

151. Smith, J., Tho, L. M., Xu, N. & Gillespie, D. A. The ATM-Chk2 and ATR-Chk1 pathways in DNA damage signaling and cancer. *Advances in cancer research* **108**, 73 (2010).
152. Pao, W. et al. KRAS mutations and primary resistance of lung adenocarcinomas to gefitinib or erlotinib. *PLoS medicine* **2**, e17 (2005).
153. Thakur, M. D. et al. Modelling vemurafenib resistance in melanoma reveals a strategy to forestall drug resistance. *Nature* **494**, 251-255 (2013).
154. Yaffe, M. The Scientific Dunk and the Lamppost: Massive Sequencing Efforts in Cancer Discovery and Treatment. *Science Signaling.* **6**, pe13 (2013).
155. Blagosklonny, M., Schulte, T., Nguyen, P., Mimnaugh, E., Trepel, J., Neckers, L. Taol induction ofp21WAF1 and p53 requires c-raf-1. *Cancer Research*. **55**, 4623, 1995.
156. Orth, J., Kohler, R., Foijer, F., Sorger, P., Weissleder, R., Mitchison, T. Analysis of mitosis and antimitotic drug responses in tumors by in vivo microscopy and single cell pharmacodynamics. *Cancer Research* **71**, 4608 (2011).
157. McGranahan, N., Burrell, R., Endesfelder, D., Novelli, M. and Swanton, C. Cancer Chromosomal instability: therapeutic and diagnostic challenges. *EMBO Reports* **13**, 528-538 (2012).
158. Sharma, S., Kelly, T., Jones, P. Epigenetics in cancer. *Carcinogenesis* **31**, 27-36 (2010).
159. Filippakopoulos, P.,et al. Selective Inhibition of BET bromodomains. *Nature* **468**, 1067-1073 (2010).
160. Brahmer, J., et al. Safety and Activity of Anti-PD-L1 Antibody in Patients with Advanced Cancer. *New England Journal of Medicine* **366**, 2455-2465 (2012).